Novel optical developments for axial super-resolution microscopy at the mesoscale

Shannan Foylan

Submitted in fulfilment of the requirements for the degree of Doctor of Philosophy

Department of Physics

University of Strathclyde, Glasgow

February 22, 2024

Declaration of Authenticity & Author's Rights

This thesis is the result of the author's original research. It has been composed by the author and has not been previously submitted for examination which has led to the award of a degree.

Collaborations with other researchers have been integral to the work of this thesis and any contributions from others have been clearly indicated in the text and are clearly listed below for each Chapter.

Chapter 2: An automated analysis pipeline was developed to accurately measure the fluorescence signal from prepared lens specimens included a segment of Open Access (available on Github) Python code written by and copyrighted by Nicholas Hall (shown in Appendix A). A stock of DH5α *E. coli* were provided by Prof. Paul Hoskisson (University of Strathclyde).

Chapter 4: Analysis of the fluorescent standing wave pattern generated with a lens specimen model was achieved using a MATLAB script written and developed by Ross Scrimgeour (appropriate citations in Chapter). A background correction pipeline for work in this Chapter was written by Lisa Kölln (University of Strathclyde). Culture and specimen preparation

of HA-GLUT4-GFP 3T3-L1 cells for imaging was performed by Angéline Geiser (University of Strathclyde). Figure 4.2 was made in Biorender using the Centre for Biophotonics account (Kay Polland, Agreement number: BY25LAR7HL).

Signed: 

Date: 12/07/2023

For Lee, Allan & Joe

Abstract

A balancing act inherent to all optical microscopy is the amount of a specimen that can be viewed in a single image and the level of spatial detail that can be resolved within it. From the theoretical basis of resolution set up by Abbe, Rayleigh and Sparrow in the 1800 and 1900s, it is understood that to obtain high (sub-cellular) resolution, a high numerical aperture (NA) lens is required. Generally speaking, with conventional optics, a high NA lens also has a high magnification, diminishing the amount of a specimen observed at once to a few hundred square microns. Furthermore, conventional optics are restricted by the physical nature of light; it is not possible to resolve detail below approximately half of the wavelength of the light used to illuminate the specimen. This phenomenon, known as the diffraction limit, is a driving factor in the advancement of super-resolution microscopy in recent years. While optical or chemical phenomena are utilised to breach the diffraction limit of imaging objective lenses in super-resolution microscopy, due to further requirements, high NA lenses are still necessary, meaning that only a handful of cells are imaged simultaneously with the exceptional resolution achieved by these systems.

In 2016, McConnell et al. presented a novel bespoke objective lens with the unusual lens prescription of a low magnification and comparatively high NA (4x/0.47). The system, called the Mesolens, was designed with such a prescription to image large cell volumes (6 mm x 6 mm x 3 mm) while retaining sub-cellular resolution in 3D. The Mesolens has allowed for imaging of entire bodies and organs, resolving every fluorescently labelled organelle of interest within the specimen. Several optical developments have been reported to speed up the acquisition rate across the large imaging volume and to bring the 3D resolution of the system towards isotropy.

However, until the work discussed in this thesis, the axial resolution of the Mesolens remained at the diffraction limit reported in the initial paper of 7 µm. In this work, I have developed two new illumination modalities that manipulate the excitation light before it reaches the specimen plane of the Mesolens, and both provide nanometre-scale axial resolution. This lays the groundwork for further exciting potential projects.

The first technique demonstrated in this work extends the well utilised microscopic technique of Total Internal Reflection Fluorescence (TIRF) from the approximately 100 μm^2 FOV available to commercially available high magnification, high NA TIRF objectives to the full field of view (FOV) of the Mesolens in widefield (4.4 mm x 3.0 mm). The modality, which we call MesoTIRF, allows for more than a five-fold improvement in contrast, with excellent signal-background ratio and near isotropic resolution. For practicality and to allow for full characterisation, this system was designed as a prototype initially around an upright microscope system (Chapter 2) before adapting for the Mesolens (Chapter 3) and thorough characterisation and demonstration of the imaging capability of this new illuminator is provided here.

The second technique extends another microscopy method to the mesoscale, in this instance standing wave (SW) illumination. This method generates an interference pattern to excite fluorescence from labelled cellular structures and produces high-resolution images of three-dimensional specimen in a two-dimensional image. SW microscopy is generally performed with high magnification, high NA objective lenses: this results in high resolution images but only within a small FOV so the cell numbers are again limited. In Chapter 4, I will present a technique for performing SW imaging at the mesoscale. In the 4.4 mm x 3.0 mm FOV of the Mesolens, we performed topological mapping of more than 16,000 live cells simultaneously, alongside characterisation of the illumination mode and further applications in fixed mammalian cell imaging.

Contents

List of Figures

List of Tables

Acknowledgements

There are a lot of people who have provided me invaluable support, advice, supervision and friendship over the past few years and would've got me through the trials of a normal PhD, let alone one with Covid-19 in the middle. This may be a chapter in and of itself.

First and foremost, Gail McConnell. I promise this will be as quick as possible Gail, so you aren't sick while reading this. Gail, in a sentence, is exactly the kind of scientist and person you would want to be your PhD supervisor. She has been a constant source of support, has patiently taught me through many years of daft questions (the one which still sears my brain when I think about it is "why can't I see the beam?" while wearing laser safety specs...), adapted my project through challenging paths and has put me forward for so many cool opportunities. Without the backing of Gail, I wouldn't be even a halfway decent scientist and certainly wouldn't be as confident as I now am talking about my work and science in general. There are definitely people I would have preferred to have been supervised by less!

I'd like to thank Brad Amos, for a whole list of reasons, notwithstanding the incredible opportunity he gave me to work with him as an RA on resuscitating an old vacuum evaporator and running damage control on a flood besieged prototype Mesolens immediately following my PhD. Brad is one of the most knowledgeable people I've had the privilege to meet let alone work with and days spent working with him in optics and wet labs or hearing his stories from his time spent teaching the world about the confocal microscope are among my favourite of the past few years.

I'd also like to thank Mike Shaw, my industrial supervisor at NPL. While Covid-19 got in the way of my spending any extended period of time in Teddington, Mike has

been a constant source of feedback and advice for interesting ideas to follow in the lab, manuscript preparation and analysis techniques.

Eliana, Mollie and Jordan, from the day we met in Gail's office on the 1st of October 2018, all three of you supported me and became my lifelong friends, I can't imagine doing a PhD without you three. Can't wait until we're in a retirement home together reminiscing about Plymouth, all those silly acronyms in microscopy and still fighting amongst ourselves for Eliana's love.

Lisa, Katrina, you kindly accepted my silly first year questions as the more experienced PhD students and soon became my friends as well as workmates. You're both two of the coolest people I know (yes, I will tell continue to tell everyone I meet that Katrina worked for NASA).

Liam, excuse me, Dr Liam Mark Rooney FRMS. There is nothing I can write here that is appropriate for print but you patiently taught me a lot of biology and begrudgingly accepted my friendship, blehhh.

Meg and Bea, I'm sorry you had to share an office with stressy final year Shannan but our chats about Meg's clumsiness and Bea's desire to sue someone always made me laugh and I'm glad to call you both friends. Becca, our chats about how annoying TIRF can be were always therapeutic and thank you for the gift of the glow worms!

Jana, Gill, Peter, thank you for teaching this physicist who hadn't held a pipette before 2018 how to do cell culture. I guess it is partly your fault that I've now turned to the dark side and keep moving further towards biology going forward in my career! Ross, Jan, Nick, you are all computational gurus, thank you (and apologies) for patiently answering my many basic coding/analysis questions.

Mollie B, Kay and Mollie's three hypothetical wains, I'm glad to be sticking around Strathclyde for a bit longer to keep hearing your amazing chat and to see you develop your very cool projects.

There are many amazing researchers on levels 5 and 6 of SIPBS but specifically Ryan, Holly, Tanith, Angéline, Laura, Maggie, David, Geraldine and Katherine, from helping me out with biology without making me feel like a silly physicist to just gabbing or complaining with me, you have helped me so much over the past few years, thank

you!

Andrew, you're an alright friend I suppose, I'm happy that we did our PhDs at the same time and had the odd supportive lunch. It goes against our dynamic for me to be too nice in print that could be traced back to me but you are a very good egg.

Anna, love of my life, you know what you did. Thank you for always being the reasonable one (I know right?), talking me down and making jokes. I can't imagine doing very much without you as the other half of Shananana but a PhD definitely wouldn't be on that list.

Alison, you've probably been the person who has believed in me professionally for the longest. You're a wonderful friend, thank you for everything.

Thank you to my family for always supporting me and only occasionally (every week) implying that I only did the PhD to get to go to all the conferences I've been lucky to go to in very cool places. You encouraged me to be a wee geek from a young age and hopefully this wee geek can now go by Dr Foylan.

To the three men this thesis is dedicated to, I love and miss you all and wish I could show you this achievement. I'd like to think you'd be proud and make many doctor jokes!

Finally, Toast, you were an active hindrance to the thesis writing process if anything, but you are still the best cat out.

Research output

Published works

S. Foylan, W. B. Amos, J. Dempster, L. Kölln, C. G. Hansen, M. Shaw, and G. McConnell , "MesoTIRF: A prism-based Total Internal Reflection Fluorescence illuminator for high resolution, high contrast imaging of large cell populations", Applied Physics Letters 122, 113701, 2023 https://doi.org/10.1063/5.0133032

S. Foylan, J. K. Schniete, L. S. Kölln, J. Dempster, C. G. Hansen, M. Shaw, T. J. Bushell, and G. McConnell, "Mesoscale standing wave imaging", Journal of Microscopy, 1–9, 2023 https://doi.org/10.1111/jmi.13

Oral presentations

- (29th January 2023) **SPIE Photonics West**, San Francisco, USA: "MesoTIRF: a novel axial super-resolution illuminator for membrane imaging over a 4.4 x 3.0 mm field of view" & "Towards widefield multiphoton mesoscopy with the Mesolens"
- (18th November 2022) **University of Glasgow Chemical Photonics Invited Seminar**, Glasgow, UK: "Optical developments for axial super-resolution imaging on the mesoscale"
- (7th September 2022) PicoQuant Single Molecule Workshop, Berlin, Germany: "MesoTIRF: Axial super-resolution imaging on the mesoscale"

- (5th July 2022) **RMS Frontiers in Bioimaging**, Birmingham, UK: "MesoTIRF: Axial super-resolution imaging on the mesoscale"
- (17th November 2020) **RMS Frontiers in Bioimaging**, Virtual: "Measuring the thickness of an evanescent field for TIRF mesoscopy"
- (15th August 2020) **National Physical Laboratory Postgraduate Institute Conference**, Virtual: "Characterising an evanescent field for large field of view illumination in mesoscopic imaging"
- (21st August 2019) **University of Strathclyde Physics Department Postgraduate First Year Conference**, Loch Lomond, UK

Poster presentations

- (29th June - 1st July 2022) **British Biophysical Society Biennial Meeting**, Galway, Ireland
- (7th - 10th June 2022) **European Light Microscopy Initiative Meeting**, Turku, Finland
- (20th August 2020) **University of Strathclyde Physics Department Postgraduate Second Year Poster Session**, Virtual
- (22nd June 2020) **Photonics Online Meeting**, Virtual - Twitter
- (19th August 2019) **Glasgow Imaging Network**, Glasgow, UK
- (5th June 2019) **SPIE Photonex**, Glasgow, UK
- (29th May 2019) **SUPA Annual Gathering**, Glasgow, UK

List of abbreviations

2D: two dimensional

2P: two photon

3D: three dimensional

APTMS: (3-Aminopropyl)triethoxysilane

CLSM: confocal laser scanning microscopy

CW: continuous wave

DAPI: 4',6-diamidino-2-phenylindole

DMSO: dimethyl sulfoxide

DNA: deoxyribonucleic acid

DNA-PAINT: DNA-Point Accumulation In Nanoscale Topography

FOV: field of view

GFP: green fluorescent protein

IR: infrared

IRM: Interference Reflection Microscopy

LB: Luria Bertani

LED: light emitting diode

LUT: look up table

NA: numerical aperture

OD: optical density

PI: propidium iodide

PSF: point spread function

RGB: red-green-blue

ROI: region of interest

SBR: signal-background ratio

SIM: Structured Illumination Microscopy

SMLM: Single Molecule Localisation Microscopy

SNR: signal-noise ratio

SRRF: Super-Resolution Radial Fluctuations

STORM: Stochastic Optical Reconstruction Microscopy

SW: standing wave

TIR: Total Internal Reflection

TIRF: Total Internal Reflection Fluorescence

UV: ultraviolet

"Wait, what?"

Dara Ó Briain

Chapter 1

Introduction

The field of microscopy is several centuries old, and began with Hans Janssen [1], a Dutch manufacturer of reading glasses, who created the first compound microscope with his son in 1595. However, the first scientific application of microscopes is more commonly associated with the renowned physicist Robert Hooke and the microbiologist Antonie van Leeuwenhoek. The former produced his seminal publication *Micrographia* in 1665 [2] in which he displayed compound microscope images of insects, fleas, seeds, plants and introduced the scientific world to the concept of cells as the building blocks of biological systems. The latter developed a single lens microscope with the initial purpose of examining thread counts in drapery fabrics and then used his handiwork to begin studying bacteria and protozoa [3].

The progression of microscopy from these early roots to an expansive field of scientific research is due to the technical advancement of many complementary fields of study. As the physics of optical systems was better understood, the instrumentation for microscopes became more robust until the limitation in resolvable detail was set by the nature of light itself (see Chapter 1.1.3). Manufacturers produced multi-element objective lenses to correct for aberrations, which allows for specimens to be magnified through several orders of magnitude while retaining image quality. Correction collars which axially shift the position of lenses within the objective lens barrel are commonplace on high magnification, high numerical aperture commercial objective lenses to account for aberrations caused by variations in coverglass thickness. Additionally,

lenses are designed to refractive index match relevant immersion media. The refractive index of glass is around 1.5 and, as such, high resolution objective lenses are designed to match this index with the specimen of interest immersed in high quality immersion oil of this refractive index. However, a more natural biological environment is aqueous, where the refractive index is lower, at around 1.33. Water-dipping objectives matched to this index are common, but the resolution produced is generally slightly lower than oil immersion. After the discovery of fluorescence (see Chapter 1.3), photochemistry became crucial to the development of novel fluorescent molecules for organelle specific labelling of biological specimens. One of the workhorses of many cellular biology imaging laboratories, the Confocal Laser Scanning Microscope (CLSM), required the development of robust laser technologies and adequate computational power. As such, they were only introduced to biology labs in the late 1980s, [4], [5] . For a similar reason, the high optical powers required for two-photon excitation of fluorescence required a ultrashort time pulsed mid-deep IR laser source, so while the theory was well described in the 1950s by Maria Göppert-Meyer [6], the experimental realisation was not observed until 1990, following the discovery and widespread use of the femtosecond pulsed laser [7], [8].

Ultimately, the progression of microscopy has been dictated by the biology of interest. Super-resolution optical microscopy has come into being in recent decades as scientists became interested in the structure and processes of biological specimens at the molecular level. Electron Microscopy (EM) and Atomic Force Microscopy (AFM) offer spatial resolution significantly better than super-resolution light microscopy, but require vigorous and often destructive preparation techniques, such as fixation, dehydration, cyrotoming and embedding in non-biological media such as resin. As such, examining biological structure and dynamics *in vivo* is not possible with EM and while correlative approaches have allowed for fluorescence imaging and EM to be performed in tandem [9], these processes are generally not trivial and so organelle specific imaging with EM is often performed with histochemistry. Furthermore, EM and AFM do not offer the exquisite molecular specificity synonymous with fluorescence labelling, so specificity is lost for higher resolution in these instances.

This introductory Chapter will cover the theoretical basis of image formation in an optical microscope, the metrics used to describe image quality, and will lay the groundwork for the various optical microscopy techniques which will be discussed in this thesis. The optical developments produced in the later Chapters of this work are extensions of existing and well-utilised techniques and, as such, the background and previous work with these methods will be presented here in depth.

1.1 Imaging theory for microscopy

1.1.1 Image formation

Image formation, in its simplest form, requires an object illuminated with light and a single focusing lens element. The imaged object in question absorbs light in a process governed by the Beer-Lambert law [10] and will attenuate the intensity of illumination light in this region accordingly. The periphery and non-absorbing features of the object will scatter the light with a characteristic pattern depending on the physical configuration of the object. An inverted image of an object placed at infinity will be formed at the focal length of the collecting lens. Considered under ray optics evaluations, this is a simple process. Simple, geometric relations connect an object placed at or within the focal length of a lens to the image of the object formed at the lens' back focal plane, as in Figure 1.1(a). However, there are several physical characteristics of light which muddle this simplistic view of image formation by a lens. Chiefly, light acts as a wave and is therefore subject to diffraction and interference phenomena. As such, a lens element can be thought of as a stack of prisms of varying thicknesses and input face angles, which will diffract incident light to varying degrees, as illustrated in Figure 1.2 for (a) convex and (b) concave lenses.

In the simplest and most common instance of light diffracting through a circular aperture, an illuminated point source will form a disk in the image plane rather than a point due to different wavefronts within the illumination beam diffracting through the lens to different degrees. The model for light propagating through a circular aperture is the simplest case for examining diffraction and interference effects caused by the

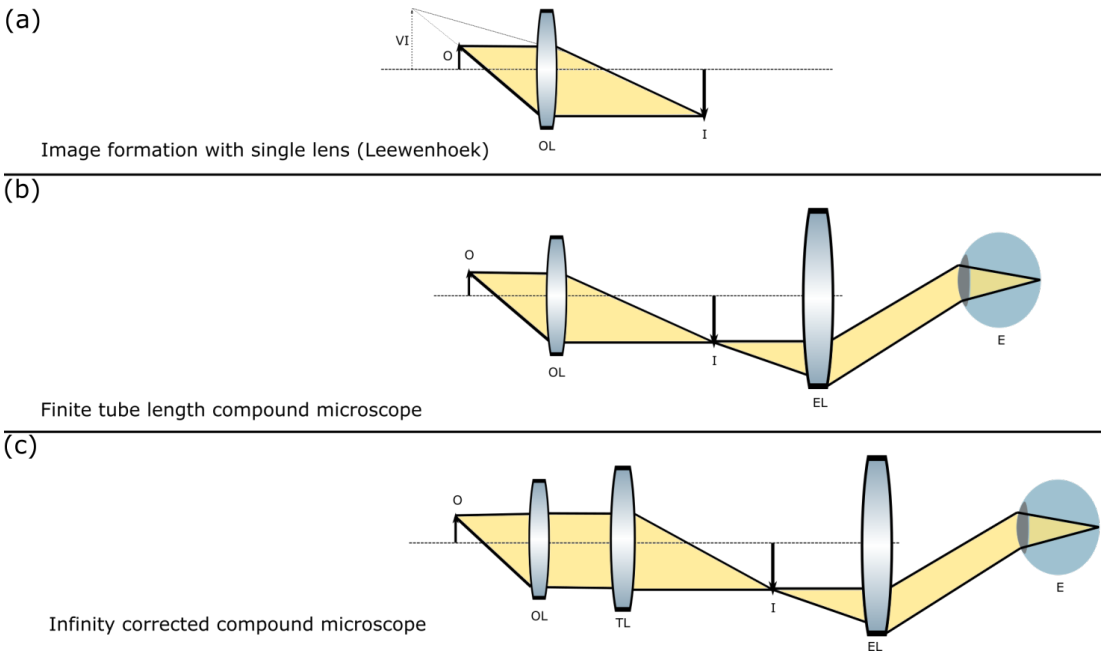

Figure 1.1: Ray diagrams for (a) single lens element, (b) finite tube length and (c) infinity corrected microscope systems, adapted from [11]. VI: virtual image, O: object, OL: objective lens, TL: tube lens, I: (intermediate) image, EL: eyepiece lens, E: eye (or camera, parallel to eye's axis).

element, and the theory presented from this point assumes this configuration.

The simple one lens imaging system, as shown in Figure 1.1(a) was employed by Leeuwenhoek, where the eye was placed at the focal plane of the single lens. Following on from Hooke, modern microscopes consist of a compound of several lens elements such that the specimen plane and image plane are further apart, allowing for additional optics to be placed in the train to allow for further magnification, masks, polarisers etc. Most modern commercial objective lenses either have finite tube lengths of 160 mm (Figure 1.1(b)) or are 'infinity corrected' such that any additional optical element placed between the objective and tube lens of the system does not introduce unwanted aberration into collected images (Figure 1.1(c)).

1.1.2 Characteristics of a lens and resulting microscope system

The basis of any optical imaging system lies in the manipulation of light by utilising the refractive index of different materials. Refractive index is a material property

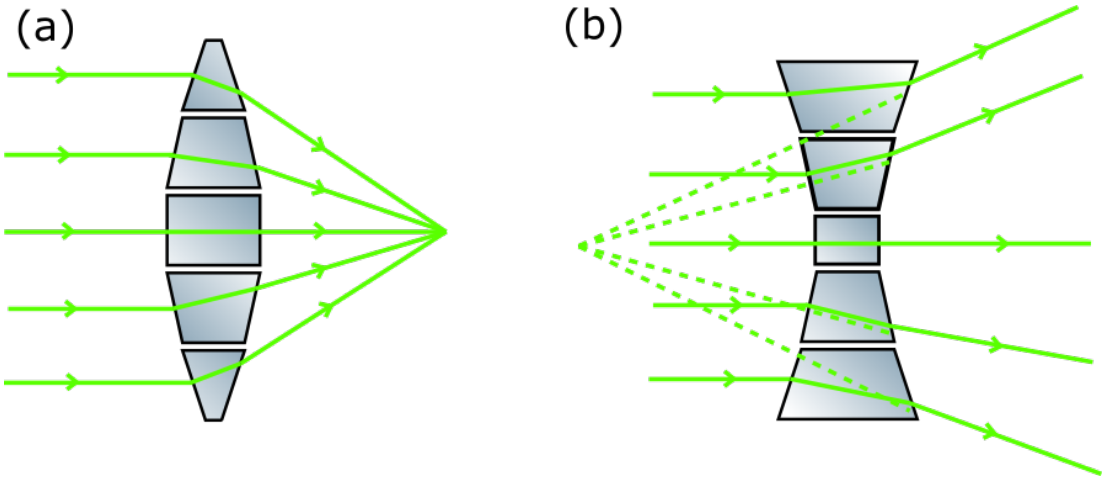

Figure 1.2: (a) Convex lens illustrated as a stack of prisms forming a positive focus, converging collimated wavefronts (b) concave lens illustrated as a stack of prism forming a negative focus, diverging collimated wavefronts.

which describes the rate at which light will slow down when propagating through the material. This is described by equation (1.1), where c is the speed of light in a vacuum (in metres/second) and v is the speed of light in the given material [12] (also in SI units of metres/second),

$$n = \frac{c}{v} \ . \tag{1.1}$$

Geometric optics can be used to describe how light will behave passing from one material into another. This process is governed by a simple relation known as Snell's law, [12], given as

$$n_1 \sin\theta_1 = n_2 \sin\theta_2 \ . \tag{1.2}$$

This relation describes the case where a wave propagating in a material with refractive index n_1 is incident on a material boundary with a second media of refractive index n_2 at an angle of incidence θ_1. The angle at which the wave refracts into the second media is given by θ_2. The instance when these two angles are equal describes reflection back into the media of refractive index n_1.

The principal function of a lens in a microscope system is to magnify an image of

a microscopic specimen to be studied by a human eye or a digital camera. Therefore, a fundamental parameter of a lens or a lens system is the magnification, which can simply be expressed as the ratio between the image size and the object size. This value can also be related to the focal length of the lens f. This is the point where an image of an object placed at infinity will form relative to the lens. More generally, we consider the distance of the object from the lens to be described by u and the image by v. The lens formula (1.3), [13], is a fundamental formula in optics and can be applied to any single lens system, assuming propagation is occurring in air ($n \simeq 1$), or more precisely in a vacuum. The lens formula is given as

$$\frac{1}{f} = \frac{1}{u} + \frac{1}{v} \ . \tag{1.3}$$

The magnification of an image formed at v by a lens of focal length f can then be given by (1.4), [13], where y_{image} is the height of the image from the optical axis and y_{object} the height of the object. By convention, $f > 0$ lenses are convex, $f < 0$ are concave, an image with a distance $v > 0$ is termed real, $v < 0$ is imaginary and all objects must have a physical height ($u > 0$). Magnification is expressed as

$$M = \frac{y_{\text{image}}}{y_{\text{object}}} = -\frac{v}{u} \ . \tag{1.4}$$

A useful extension to the lens formula is for the instance of a thin lens, that is the case where the lens is thin enough to cause negligible translation on the incident light, [14]. This formula allows one to relate the radii of curvature (R_1, R_2) of each of the lens faces to the focal length of the thin lens of refractive index n_{l} using the relation

$$\frac{1}{f} = (n_{\text{l}} - 1)\left(\frac{1}{R_1} - \frac{1}{R_2}\right) \ . \tag{1.5}$$

The light gathering power of a lens is given by the numerical aperture (NA) which is defined by the half-angle of angles accepted by the lens element (or collection of lens elements in an objective barrel), θ. The NA of an element is a fundamental dimensionless quantity in imaging; it defines the light gathering power, the spatial resolution (discussed in detail in Chapter 1.1.3) and the optical throughput of the

system. The NA is given by

$$\mathrm{NA} = n \sin(\theta) \ . \tag{1.6}$$

where n is the refractive index of the medium between the lens and the object, and θ is the half angle of collection of the objective lens. Trigonometrically, the manufacturer's quoted NA for an objective lens can be related to the size of the imaging field by the specified working distance which is the distance from the front element of the lens barrel to the specimen plane when the object is in focus. This would be equivalent to the focal length for a single lens in an optical path. The field of view (FOV) of a microscope system may be expressed in a few ways depending on whether one is interested in the illumination field (how much of the specimen is physically illuminated), the FOV relative to the microscope eyepiece or relative to the camera sensor recording the image, [11]. For the instance where the FOV relative to the eyepiece is required, the field size may be approximated by the f-number of the eyepiece (that is, focal length divided by the diameter of the lens aperture) divided by the objective lens magnification.

Due to the wave nature of light, aberrations in images can be seen due to diffraction, dispersion and misalignment of elements the optical path. Lens manufacturers account for spherical and chromatic aberration by combining several lenses into doublets or optical trains to correct for the dispersion caused by one optical element, [11], [15]. By coating elements with anti-reflection coatings, manufacturers improve the transmission efficiency of an element, which leads to a resulting improved image contrast. Furthermore, high NA and high magnification commercial objective lenses use high refractive index immersion media (such as Type F or Type DF oil, [16]) to index match the mountant of the imaged specimen to the optics within the objective lens. This permits the full NA of the element or elements to be used.

Finally, a useful characteristic property of an optical system is the optical throughput. This is often termed the optical (or Lagrange) invariant or étendue. This value is the product of the pupil area and the collection angle of this pupil, [17] and relates the incident wave to the transmitted wave through the optical element. The optical

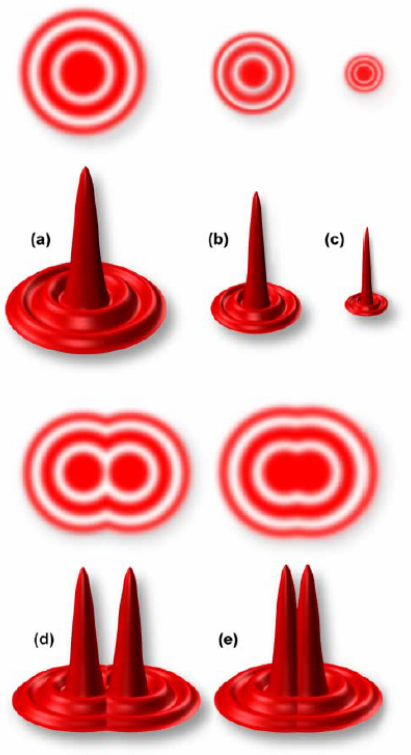

Figure 1.3: 2D and 3D representations of a point source imaged with a circular aperture, forming Airy disks in the image plane. (a) - (c) image formed with increasing numerical aperture lenses. (d) Rayleigh criterion for two spatially resolved objects, (e) Sparrow criterion for two spatially resolved objects. Image reproduced from [11].

throughput of a system can be increased through optimisation but cannot be decreased.

1.1.3 Spatial resolution

The wave nature of light imposes a spatial resolution limit, which can be well understood under Airy diffraction theory. This is shown schematically in Figure 1.3 where an Airy disk illustrates the effects of both diffraction and interference through a lens element. When a system is focused on a point source, the interference minima between the bright maxima fringes are of zero intensity. The resolution limit of the system can then be characterised by considering the geometry of these fringes. In the 1800s, Ernst Abbe [18] provided a framework for the lateral resolution of a system using this interference model and considered the radius of an Airy disk to be the limit. Therefore, the Abbe lateral resolution limit is given by

$$r_{\text{Abbe}} = \frac{\lambda}{2NA} \ . \tag{1.7}$$

Here, λ is the wavelength of illuminating light and NA is the numerical aperture of the imaging objective lens.

A few decades later, this framework was extended by Lord Rayleigh [18] to consider two Airy patterns formed by two spatially close point sources. The Rayleigh limit defines the minimum distance of separation necessary between two objects to be distinguishable given the wavelength of illumination and the numerical aperture of the imaging objective. The Rayleigh lateral resolution limit is given by

$$r_{\text{Rayleigh}} = \frac{0.61\lambda}{NA} \ . \tag{1.8}$$

A somewhat less widely utilised measure of spatial resolution was produced by Sparrow, [19]. In this instance, the resolution limit is given by the point where two separate objects are just distinguishable but the intensity between the two zeroth order diffraction patterns given by the objects respective Airy disks is constant, i.e. there is no dark minima between them, as illustrated by Figure 1.3. The Sparrow lateral resolution limit is given by

$$r_{\text{Sparrow}} = \frac{0.47\lambda}{NA} \ . \tag{1.9}$$

Similarly, one can define axial resolution by considering the diffraction pattern formed along the optical axis, generally termed the z axis of the microscope, and is the minimum distance two objects must be separated axially in order to be distinguishable from each other. This limit is given by equation (1.10) and, given the square dependence on the NA, axial resolution is significantly poorer than lateral resolution for the same imaging objective. It also follows that axial resolution is forfeited for the lower magnification afforded by conventional low NA objective lenses.

$$z_{\text{Rayleigh}} = \frac{2n\lambda}{NA^2} \ . \tag{1.10}$$

The axial resolution of an objective lens defines the depth of field, which is the

distance along the optical axis in z within which an object is in sharp focus at one axial position of the imaging objective in object space. In an ideal imaging scenario for brightfield microscopy, depth of field is equivalent to axial resolution [18]. A closely related value to depth of field is depth of focus, which refers to the distance along the optical axis in image space where an image is in sharp focus. As with lateral spatial resolution, depth of field decreases for higher NA objective lenses.

The point spread function (PSF) of an imaging system describes how an imaged point source is observed in the image plane of the system, it is comparable with an Airy disc if all apertures in the optical train are circular, [12]. A 3D representation of both lateral and axial resolution of a system can be demonstrated by its PSF, which demonstrates the convolution that diffraction limited optics impose upon an imaged point source. Mathematically, imaging with a physical lens can be expressed as a convolution between the object and the PSF of the system. An illustration of lateral and axial PSFs of a sub-diffraction limited sized point source is shown in Figure 1.4.

In a physical imaging scenario, the ideal resolution of the imaging optics must be matched to the sensor used to record the varying intensity across the image. Scientific grade cameras for microscopy have a fixed pixel size, count and acquisition method which affects the resultant resolution of an image. The two main types of widefield cameras for microscopy are Complementary Metal-Oxide Semiconductors (CMOSs), [20] and Charged Coupled Devices (CCDs), [21]. The former converts photons to electrons on its sensor chip pixel-wise, much like an array of bucket detectors across the sensor face. The latter reads out the sensor array line-wise, with each column of pixels being read out by a single analog-digital-converter. The physical size of the pixel on the sensor (usually on the order of microns) must be measured relative to the size of a pixel at the image plane in order to accurately measure the size of objects in the obtained image. More pixels of an appropriate size on the sensor face leads to a higher camera resolution, but this comes at a cost of lower frame rate, which is particularly detrimental for imaging of fast dynamic processes.

In order to utilise the full resolution of a sensor, one must sample the spatial frequencies of the imaged object close to the Nyquist rate [22]. This criterion requires

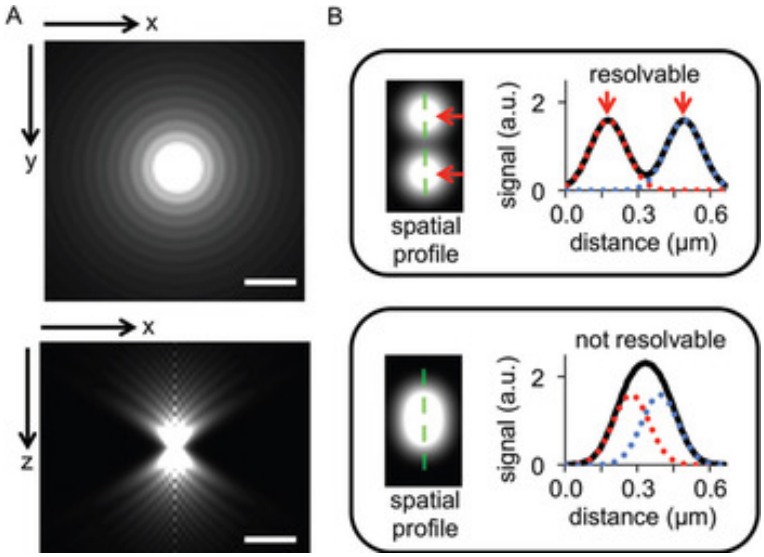

Figure 1.4: A: lateral and axial PSFs of an imaged point source, B: resolvable vs unresolvable feature demonstrated by intensity line profiles, reproduced from [23].

that the pixel size must be set to twice that of the resolution limit set by the imaging optics, so is generally on the order of the wavelength of illuminating light [22]. Mismatch of pixel size to magnification will result in either undersampling of the object, which may be desired but ultimately compromises resolution, or in oversampling which is still limited to Nyquist resolution but introduces redundancy and is time-consuming.

1.1.4 Image quality metrics and improvement techniques

Contrast in microscopy arises from a feature in the imaged specimen which alters the intensity of the illumination light, [24]. A host of the physical properties of light can be manipulated to achieve contrast enhancement in optical microscopy. For example, in Differential Interference Contrast (DIC) microscopy, interference between light wavefronts gives rise to sharper contrast from the optical path difference of the illumination beam which is split by a linear polariser and a quarter wave plate such that two parallel propagating beams pass through the specimen at different points which may vary in height and refractive index [11]. Interference effects have also given rise to resolution enhancing techniques such as Structured Illumination Microscopy (SIM) where alternating spatially different illumination patterns bring higher frequency information into

the detection bandpass of the microscope in order to improve lateral spatial resolution by a factor of 2, [25]. Furthermore, waves interfering such that their superposition appears stationary are beneficial to optical microscopy in that the nature of standing waves allows for 3D information to be extracted from 2D image data, [26]. Standing Wave (SW) microscopy will be discussed in depth in Section 1.6 of this Chapter and in Chapter 4 where the author has presented work extending SW imaging into the mesoscale.

The phase of the illuminating light can be used to improve the contrast of brightfield micrographs. Phase contrast lends itself well to imaging of thin, transparent specimen which do not absorb light as small changes in phase can be associated to small changes in the amplitude (or brightness) of the wave. Light undergoes a small phase change (fractions of a wavelength) when interacting with matter. By reverse engineering the effect, including phase optics into the illumination and detection path of a brightfield microscope, the small phase changes can be converted into a brighter signal, giving rise to higher contrast images, [27].

Closely interlinked with the concept of contrast is the background that can be observed in a micrograph. In brightfield illumination, for example, a 'perfect' image will contain a bright object on a dark (zero intensity count) background. Such a situation is incredibly unlikely in a physical imaging experiment as most specimen will not be fully absorbing, errant light from another source may enter the illumination path, cameras have inherent electronic noise and even with pristine alignment, slight inhomogeniety of illumination will be introduced by the optics of the system itself.

1.2 The widefield microscope

A useful distinction in optical microscopy classifies techniques into the means by which images are collected. The older method of capturing detail from a specimen of interest using the eyepiece of the microscope or with a digital camera is termed widefield microscopy as each pixel of the image is acquired simultaneously from a uniformly illuminated specimen plane.

Widefield illumination and detection is a relatively fast means of imaging, limited

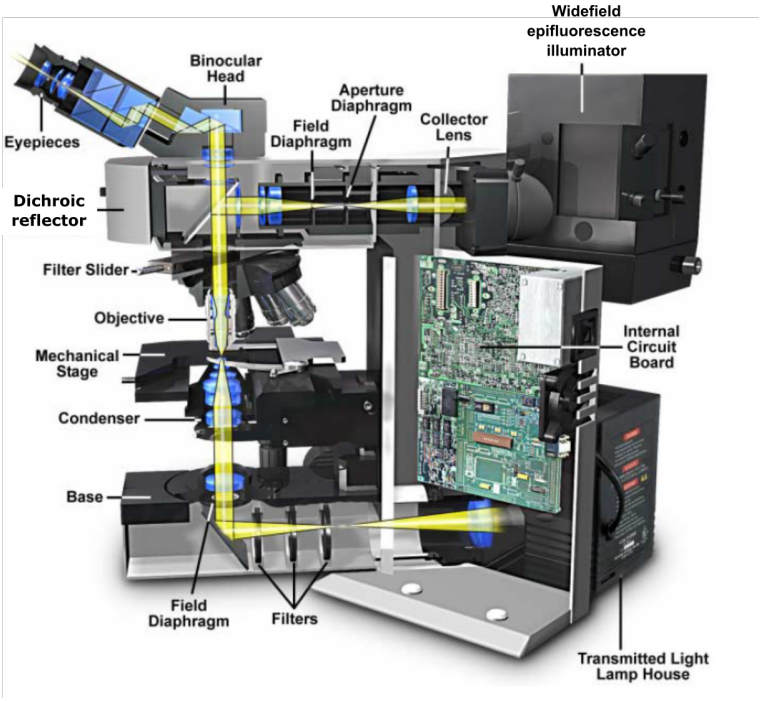

Figure 1.5: A schematic of the components of an upright widefield microscope showing epi- and transmission illumination ray paths. Modified from [11].

only by the camera technology utilised and the size of the imaging field investigated. The most simple means of obtaining contrast in optical microscopy, brightfield illumination, is a widefield technique which has been developed by introducing contrast enhancement methods described previously (Chapter 1.1.4) to include interference, diffraction and fluorescence features.

Brightfield transmission microscopy is the most standard means of imaging on an optical microscope, and is generally available as an imaging modality on commercial systems utilised for much more complex imaging. It requires an optical train of correctly aligned high quality lenses, Figure 1.6, and a white light illuminator, either a inert gas lamp, a halogen bulb or a white light LED source. Köhler illumination is a technique of illuminating the observed specimen utilised widely by most microscope users when imaging with brightfield transmission microscopy [11].

Firstly proposed by August Köhler while working at Carl Zeiss in the late 19th century, the technique requires that an image of the source of illumination is enlarged and focused on the plane of the condenser aperture. This aperture iris can be adjusted

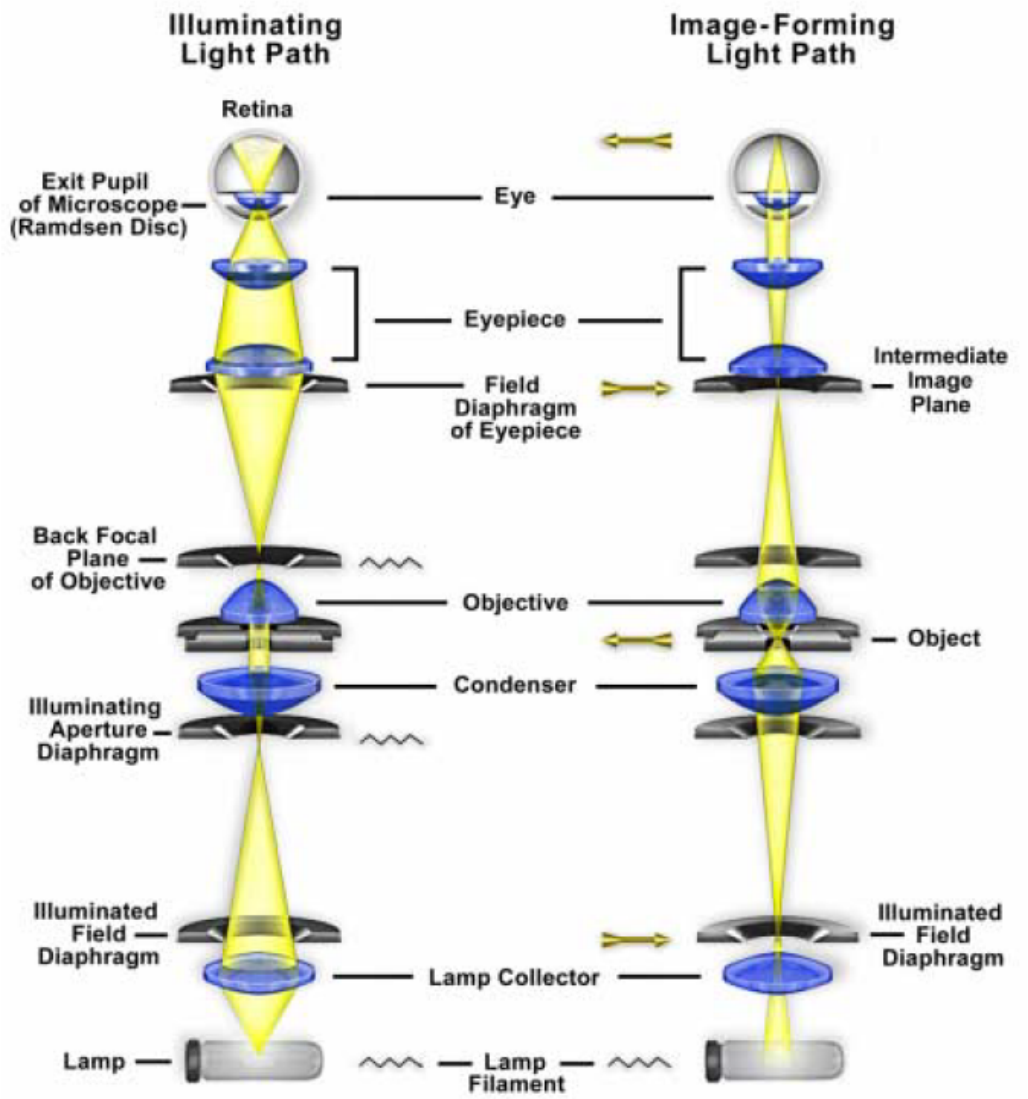

Figure 1.6: Separated conjugate image and illumination planes in optical microscopy, adapted from [11], illustrating the concept of Köhler illumination, image formation and acquisition.

to allow the desired range of light ray azimuths. The concept of Köhler illumination can be described by imaging two conjugate planes, illuminating and image forming. This ensures that the illumination at the specimen plane is not affected by defects in the condenser and therefore does not appear in the final image of the specimen, as in Figure 1.6.

All imaging data included in this thesis has been acquired from widefield illumination and acquisition in Total Internal Reflection Fluorescence (TIRF) microscopy, MesoTIRF and Standing Wave (SW) mesoscopy. These methods offer a means of acquiring axial super-resolved images in 2D, the latter method encoding 3D information into the image obtained several times faster than a scanning method across the same imaging volume.

1.3 Fluorescence microscopy

Fluorescence was first described by George Stokes in the mid-nineteenth century when he noted that the fluorescent wavelength of a specimen was always greater than the excitation wavelength, subsequently coining this phenomena as the Stokes shift, [10]. The Stokes shift is described well by a Jablonski diagram, an example of which is shown in Figure 1.7.

The excitation light induces an absorption of an electron (of energy $h\mu_A$) from the electric ground level (S_0) to some higher electronic or vibrational energy level. Fluorescence can only occur from the first excited level (S_1) and transitions from higher levels are facilitated by thermal internal conversions. The diagram shows that the fluorescent electron (and associated photon) has a lower frequency than the absorbed electron, $\nu_A > \nu_F$, so it follows that in the same media, the wavelength of the fluorescent electron (and photon) is longer than that of the absorbed photon , $\lambda_A < \lambda_F$. As electrons relax back to the ground level from the first excited level, a photon is released described by the parameters related to the higher wavelength electron. This longer wavelength emission photon is useful in imaging as it can be spectrally separated from the excitation photon, and in practice, using appropriate filters, crosstalk between these channels can be minimised or removed.

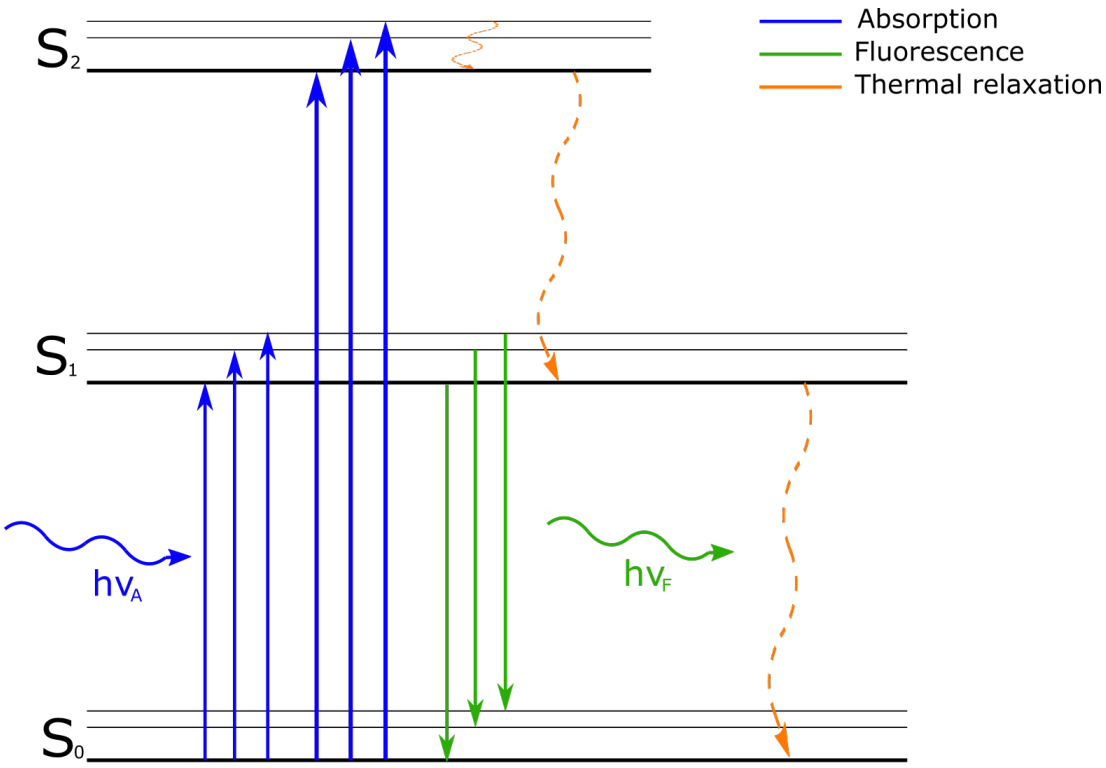

Figure 1.7: Jablonski diagram - illustration of electronic transitions resulting in absorption of a photon instigating the excitation of an electron from the electronic ground state S_0 to a higher n-th level S_n, spontaneously thermal relaxations to lower electronic levels and relaxation releasing a fluorescent photon. Schematic based on those provided in [10] .

The first fluorescence microscope was developed in 1911 by Oskar Heimstädt, [28]. Certain biological specimens emit fluorescence intrinsically and most can be fluorescently stained *in vivo* [29]. The optical detection of fluorescent or fluorescently labelled cells, proteins and organisms can illustrate temporal and morphological changes to the specimen. The main reason that fluorescence microscopy has been so widely adopted in biological imaging is the degree of specificity offered. A wide variety of fluorophores (fluorescent probes) are available from the naturally occurring, aromatic amino acids (tryptophan, tyrosine and phenylalanine), chlorophyll and green fluorescent protein (GFP), to the synthetic compounds such as fluorescein, rhodamine and many others, [10]. Through conjugation to molecules and antibodies which will bind to specific organelles and proteins of interest, fluorophores can exclusively label sub-cellular regions of interest, while the irrelevant bulk of the specimen will be dark, allowing for molecular specificity. This specificity is not offered by brightfield and darkfield illumination methods, and also generally cannot be achieved by AFM or EM. Furthermore, fluorescence microscopy can be achieved with intact specimen in physiological conditions, even in living, dynamic specimens. Again, this cannot be achieved using EM.

Photobleaching can occur in fluorescently labelled samples, where the excited state fluorophores photochemically decompose and can be seen experimentally as a reduction in fluorescence signal, [30]. Photobleaching can be partially accounted for by understanding of the photochemistry of the fluorophore being used, using neutral density filters to decrease the intensity of illumination incident on the sample and by limiting the exposure of the sample to light. However, photobleaching is a phenomenon that cannot be completely mitigated in optical microscopy, [30], but can be appropriately reduced in practice by careful consideration of illumination intensity and appropriate choice of fluorescent labels and image acquisition parameters.

1.4 The confocal microscope

Confocal laser scanning microscopy (CLSM) was developed to overcome the large background noise faced by conventional microscopy by limiting the area of illumination to

a small diffraction limited spot and then eliminating out-of-focus light by introducing a pin hole before the detector. Images of samples are then obtained by scanning the light source or moving the specimen relative to the light beam. The first confocal microscope is accredited to Marvin Minsky, [18] who applied for a patent in 1957. This first conception of a confocal microscope moved the stage and sample relative to a stationary beam. An alternative method for confocal sectioning is to use a spinning disk. This approach was developed by Paul Nipkow, and used a spinning disk to transfer 2D data to 1D data for applications in communications using Morse code, [31]. This principle was applied to confocal laser scanning microscopy by Egger and Petráň in the late 1960s, [18], by positioning a spinning disk with spiralling punched holes in front of the detector which acted as a series of pinholes. This disk acts as both a means of confocal illumination and as point detection, so eliminating out-of-focus fluorescence over the whole sample.

Three dimensional (3D) image acquisition in CLSM is a collection of optical sections, that is multiple 2D images at varying focal planes. The main addition to a conventional optical microscope is the illumination and detection apertures and the scanning system. While confocal microscopy began with stage scanning systems [32], White, Amos and Durbin [5] pioneered the now much more common laser scanning method in CLSM. This overcomes the need to move the specimen under investigation, [4].

In 1987, confocal microscopy was shown to have significant application to cellular biology by the Cambridge group, [5], who compared CLSM to widefield epifluorescence and by a group in Heidelberg, [33], who used CLSM to image the transport of a specific lipids within cells. The intensity of the illumination and the sensitivity of the detector have been shown to decrease with distance from the plane of focus, [5].

van Meer et al, [33], utilised both CLSM and conventional fluorescence microscopy to study intracellular transport of the novel sphingolipids by marking with a fluorescent ceramide analog. While conventional fluorescence microscopy was used, it proved to have insufficient resolution to distinguish between the areas of interest in the cell, the Golgi apparatus and the membrane, so the bulk of the work presented was using a CLSM.

Carlsson et al, [4], combined CLSM with 3D digital image processing to demonstrate fast optical sectioning in a spinal cord neuron, a plant ovule and in rat lung tissue. A detailed description of their experimental and computational acquisition technique lay the groundwork for the decades of useful biological research that utilised confocal microscopy in three dimensions.

While CSLM has had a significant impact in biomedical imaging, [5], [33], [34], [35], the need to scan the laser (or illumination source) over and through the depth of the entire sample is time consuming and requires extensive computational effort to stitch data sets together. It could also lead to discrepancy in measurement if biological processes have changed the specimen from one data set to the next. Confocal systems are also not able to perform high resolution optical sectioning with low numerical aperture objective lenses, [5].

While the microscopy methods discussed in the main body of this thesis are widefield techniques, confocal imaging and CLSM are crucial imaging modalities for biology and useful to discuss in the context of any microscopy research. Particularly for Chapter 4 where standing wave microscopy and mesoscopy are discussed, this imaging could have been achieved with confocal acquisition, therefore it is useful to provide a background in this niche of the field here.

The next two sections of this Chapter rely on the manipulation of an interference or diffraction property of the optics used to illuminate the specimen of interest to either improve the resolution of the system or to perform label-free imaging of the specimen.

1.5 Total Internal Reflection Fluorescence Microscopy

Total Internal Reflection (TIR) occurs when light is incident on a refractive index boundary between a media of index n_i and n_t (where $n_t < n_i$) above a critical angle θ_c, [12],

$$\theta_{\mathrm{c}} = \sin^{-1}(n);\, n = \frac{n_{\mathrm{t}}}{n_{\mathrm{i}}}\ . \tag{1.11}$$

Perhaps counter-intuitively, while the freely propagating beam undergoes TIR, a

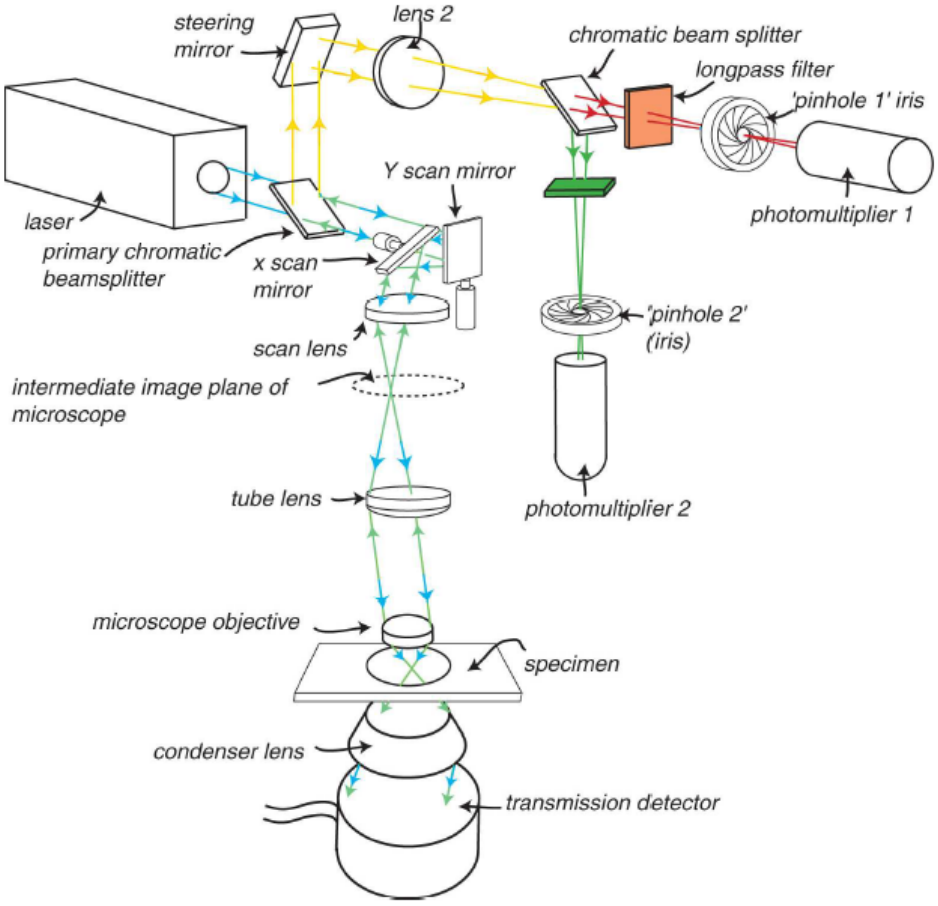

Figure 1.8: Schematic of a confocal microscope. Key components are a laser which is raster scanned across the specimen using galvo-mounted scan mirrors, confocal pinholes which limit the detection volume to a diffraction limited spot and photomultiplier tubes for recording pixel wise fluorescence. Figure reproduced from [34].

small 'disappearing' field does propagate into the second lower index media. This evanescent field decays exponentially in intensity I (in SI units of W/m^2) with distance z from the index boundary and has a propagation depth d given by

$$I(z) = I(0)e^{(-\frac{z}{d})} \ . \tag{1.12}$$

$$d = \frac{\lambda_0}{4\pi\sqrt{n_{\mathrm{i}}^2 \sin^2(\theta_{\mathrm{i}}) - n_{\mathrm{t}}^2}} \ . \tag{1.13}$$

where λ_0 is the wavelength of incident light, θ_{i} is the incidence angle and $n_{\mathrm{i,t}}$ are the refractive indices on either side of the TIR interface. Therefore, in theory, a higher super-critical angle of incidence will generate a thinner evanescent field [36]. Across a constant illuminated area, evanescent power is expected to exponentially decay with incidence angle with the maximum of d (in nm), as in equation (1.13), corresponding to the penetration depth of the evanescent field.

A more descriptive relation for the intensity of the evanescent wave can be found by defining boundary conditions and solving Maxwell's equation for the evanescent electric field vector, [37]. Using the refractive index interface as the boundary, it can be seen that evanescent field intensity varies between s-polarised and p-polarised incident light, in a relation given by

$$I_0^s = I_{\mathrm{i}}^{\mathrm{s}} \frac{4\cos^2\theta_{\mathrm{i}}}{[1-n^2]} \quad \text{and} \quad I_0^{\mathrm{p}} = I_{\mathrm{i}}^{\mathrm{p}} \frac{4\cos^2\theta_{\mathrm{i}}(2\sin^2\theta_{\mathrm{i}} - n^2)}{n^4\cos^2\theta_{\mathrm{i}} + \sin^2\theta_{\mathrm{i}} - n^2} \ . \tag{1.14}$$

$I_{\mathrm{i}}^{\mathrm{s,p}}$ are the intensities of the s-polarised and p-polarised portions of the incident beam respectively and n refers to the ratio of refractive indices given in (1.11). From this fuller description, it is clear that p-polarised incident light will result in a higher intensity evanescent field for lower super-critical incidence angles.

In the instance where an evanescent field propagates into a sample which is fluorescently labelled, from equation (1.13) only fluorophores within an axial depth of around

100 nm will be excited. Fluorescent specimens allow an evanescent field to be used to achieve axial super-resolution in imaging, with a single optical section on the order of the depth of the evanescent field, generally around 100 nm from the refractive index boundary.

1.5.1 Derivation of evanescent field parameters from first principles

An electromagnetic plane wave propagating perpendicular to a refractive index boundary (denoted as propagating in z here) can be described simply by (1.15), where k is the plane wave vector.

$$E_{\mathrm{z}} \propto exp(\mathrm{ikz}) \ . \tag{1.15}$$

In this case, the shortest possible wave front spacing, given by the natural wave spacing (λ_0), is scaled by the refractive index of the medium the wave is propagating in material of index (n_m), such that the shortest wave front spacing is expressed by $\lambda_{\mathrm{m}} = \frac{\lambda_0}{n_{\mathrm{m}}}$. This spacing is related to the wave vector $\vec{k}_{\mathrm{m}}$ which is described geometrically in Figure 1.9 and described mathematically as

$$\vec{k_{\mathrm{m}}} = k_{\mathrm{mx}}\hat{\mathrm{x}} + k_{\mathrm{my}}\hat{\mathrm{y}} + k_{\mathrm{mz}}\hat{\mathrm{z}} \ . \tag{1.16}$$

The vector in (1.16) can be manipulated to yield the wave number which is more useful in the analysis of electric fields. This wave number is expressed as

$$|\vec{k_{\mathrm{m}}}| = k_{\mathrm{m}} = \sqrt{k_{\mathrm{mx}}^2 + k_{\mathrm{my}}^2 + k_{\mathrm{mz}}^2} = \frac{2\pi}{\lambda_{\mathrm{m}}} = \frac{n_{\mathrm{m}}\omega}{c} \ . \tag{1.17}$$

where the speed of light in a vacuum (c) is a constant and the angular frequency of the wave (ω) will be a constant provided the wavelength of light remains constant throughout the system. Therefore the wave number, and by association the wave front spacing, will remain real and fixed quantities for freely propagating light in a medium with dispersion qualities described by the refractive index of the propagation media (n_{m}).

If light is incident on a refractive index boundary above the critical angle for total

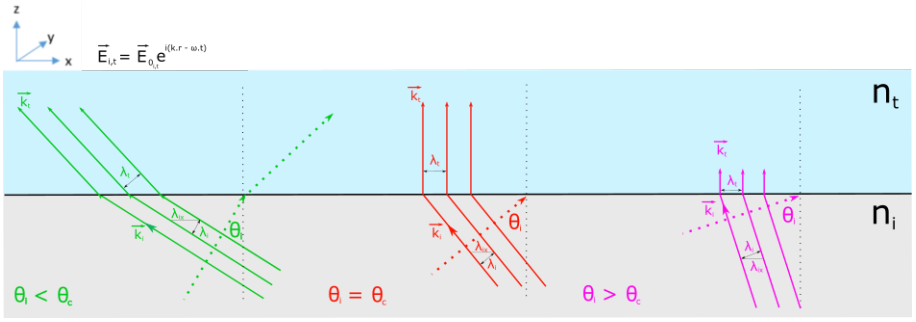

Figure 1.9: Wave front geometry shown as solid lines perpendicular to dashed arrow headed normal of plane waves incident on, reflecting and refracting from a planar dielectric interface between two different refractive index media. In green for clarity, sub-critical illumination refracting into lower index media. In red for clarity, critical illumination propagating into lower index media at normal incidence. In yellow for clarity, super-critical illumination propagating into short lived evanescent field in lower index media.

internal reflection, the wave front spacing λ_{m} can be squashed to no longer obey the wave number conservation of propagating plane waves, (1.17). Following the geometry in Figure 1.9, it is clear that there is no component of the wave vector in the perpendicular y-plane, $k_{\mathrm{iy}} = k_{\mathrm{ty}} = 0$.

It is also clear that the x-component of the wave front spacing is always longer than the natural spacing of the wave fronts, i.e. $\lambda_{\mathrm{ix}} > \lambda_{\mathrm{i}} = \frac{2\pi}{k_{\mathrm{i}}}$, where k_{i} is the wave number associated with the incident wave. In order to describe a physical optical scenario, the spacing λ_{tx} has to be continuous across the refractive index boundary,

$$\lambda_{\mathrm{tx}} = \frac{2\pi}{k_{\mathrm{tx}}} = \lambda_{\mathrm{ix}} = \frac{\lambda_{\mathrm{i}}}{\sin\theta_{\mathrm{i}}} \ . \tag{1.18}$$

It follows that the wave vector of the beam which propagates into the lower refractive index media is given by

$$k_{\mathrm{tx}} = \frac{2\pi n_{\mathrm{i}} \sin\theta_{\mathrm{i}}}{\lambda_0} \ . \tag{1.19}$$

For angles less than the critical angle, the x-component of the wave front spacing λ_{tx} is greater than the natural spacing $\lambda_{\mathrm{t}} = \frac{2\pi}{k_{\mathrm{t}}}$ and so the wave refracts into the media n_{t} with an angle described by Snell's law, (1.2).

For angles greater than the critical angle, the x component of the spacing is less than the natural spacing ($\lambda_{\mathrm{tx}} < \lambda_{\mathrm{t}}$) and so the wave vector describing the x component is greater than that describing the vector itself ($k_{\mathrm{tx}} > k_{\mathrm{t}}$). This forces the relation (1.17) into the form,

$$(k_{\mathrm{x}}^2 + k_{\mathrm{tz}}^2) > k_{\mathrm{t}}^2 \ . \tag{1.20}$$

Taking the fact that $k_{\mathrm{tx}} > k_{\mathrm{t}}$ and (1.20) into account defines that the axial component of the waves is described by $k_{\mathrm{tz}}^2 < 0$, which are purely imaginary. Under these conditions, the waves which transmit into the second media n_{t} are exponentially decaying and are termed evanescent.

Evanescent waves have four characteristic properties which make them a useful type of illumination in applications such as microscopy, fabrication of waveguides, spectroscopy and atom optics. These are shallow penetration depth, exponentially decaying intensity, and sensitivity to both polarisation and phase.

As discussed above, the z component of an evanescent wave vector is purely imaginary, allowing the electric field vector to be described as

$$E_{\mathrm{z}} \propto exp(-|k_{\mathrm{tz}}|z) \ . \tag{1.21}$$

The negative exponential arises from the squaring of the imaginary wave vector with the imaginary i present in a plane wave description ($E = e^{\mathrm{ikz}}$). Intensity is defined as the square of the magnitude of the electric field vector, $I_{\mathrm{z}} \propto |E_{\mathrm{z}}|^2 \propto exp(-2|k_{\mathrm{tz}}|z)$. The characteristic decay depth of the evanescent field can be extracted from the relation

$$I_{\mathrm{z}} \propto exp(-z/d) \ . \tag{1.22}$$

$$d = \frac{1}{2|k_{\mathrm{tz}}|} \ . \tag{1.23}$$

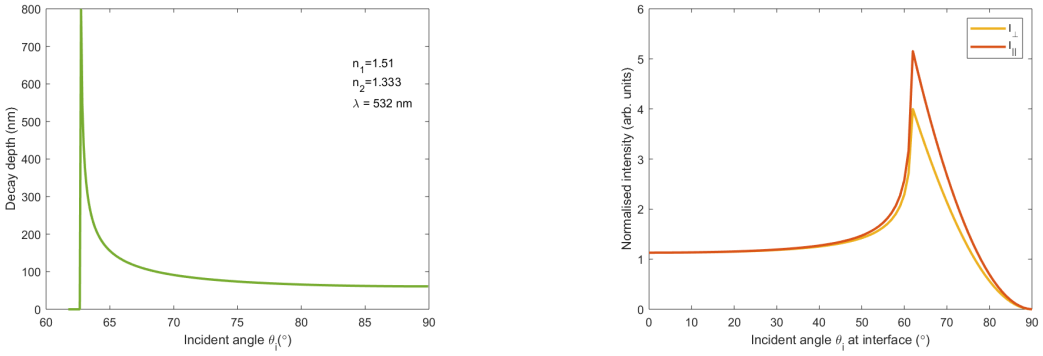

(a) (b)

Figure 1.10: (a) Decay depth against incidence angle for a 532-nm laser undergoing TIR at a glass to water interface (b) Intensity (perpendicular (yellow) and parallel (red) polarised) against incidence angle for a sub- and super-critical green laser beam.

As the wave vector relation $k_{\mathrm{t}}^2 = k_{\mathrm{tx}}^2 - k_{\mathrm{tz}}^2$ holds, the decay depth can be rewritten as

$$d = \frac{1}{2\sqrt{k_{\mathrm{tx}}^2 - k_{\mathrm{t}}^2}} \,. \tag{1.24}$$

This relation can be expanded to include more experimentally relevant variables using the known equations (1.19), (1.11) and $k_{\mathrm{t}} = \frac{2\pi n_{\mathrm{t}}}{\lambda_0}$, leading to the relation shown in equation 1.13.

For an incidence angle just above the critical angle, the depth of the evanescent field d is on the order of the wavelength of the incident light, λ_0. Going into the supercritical regime can push this depth down to fractions of the wavelength of the incident light, approaching 100 nm. Figure 1.10a illustrates the drop in decay depth as the incidence angle of illumination is pushed further and further supercritical, for the instance of a green laser illumination source ($\lambda = 532\,nm$) totally internally reflecting on a glass ($n_{\mathrm{i}} = 1.51$) to water ($n_{\mathrm{t}} = 1.33$) interface. The relation between intensity of the polarised components of an electric field vector going through the super-critical angle for TIR is shown in Figure 1.10b.

1.5.2 Fluorescence excitation with a beam undergoing TIR

The rapidly decaying evanescent field produced by a beam undergoing TIR and described by the parameters discussed above is advantageous to several applications, including telecommunications, surface plasmon resonance and quantum information processing to name a few [38]. In optical microscopy, this phenomenon has allowed for the development of an unlabelled (Total Internal Reflection Microscopy, TIRM) and the much more popular labelled Total Internal Reflection Fluorescence (TIRF) microscopy.

TIRF microscopy is now an established imaging technique commonplace in many cellular biology laboratories. The method was introduced to the field of biology by Axelrod [39] in the 1980s who used a glass prism to impose TIR on the fluorescence excitation beam. With this setup, the authors were able to demonstrate the contrast improvement and background rejection now synonymous with TIRF imaging in membrane labelled epithelial cells.

TIRF microscopy has been used extensively in cell biology to image cell contacts [39], to study adhesion of vesicles to the cell membrane [40], [41], [42], to study ion channels, [43], endocytosis, [44] and to examine the self-assembly of proteins into peptide chains [45].

Generating TIR at the specimen plane can be achieved using an expensive TIRF objective [46], with a glass prism [47], or more recently, with a waveguide, [48] (see schematic included as Figure 1.11). To support super-critical illumination, TIRF objectives have a numerical aperture (NA) between 1.45-1.5, however these objective lenses invariably have a high magnification of at least 60x. As such, the FOV is restricted to around 100 µm x 100 µm, which supports imaging of only a few cells in a single image. Stitching and tiling methods can be used to image larger specimen areas, but these methods routinely introduce artefacts into the resultant image (e.g. inhomogeneous illumination leading to dark bands between adjacent areas, or imperfect registration between adjacent FOVs), can be time-consuming and computationally demanding.

Waveguide-based TIRF obviates the need for a very high NA objective lens. Moderately large FOV TIRF images of up to 0.5 mm x 0.5 mm in size have been demonstrated with waveguide-based TIRF using custom-designed chips [49], [50] and results

show tens of cells imaged in a single image. More recently, chip-based TIRF microscopy, among other complementary imaging modalities, has been shown where the system is effectively independent of imaging objective, [51].

Prism-based TIRF can use off-the-shelf components and therefore is substantially lower cost and easier to implement than than both of these other methods, and it can, in principle, be achieved with any objective lens. This potentially allows for larger fields of view (FOV) than those possible with high magnification, high numerical aperture (NA) TIRF objectives. However, even with prism-based TIRF, the detection objective lens remains a fundamental limitation when considering FOV. Low magnification objective lenses that support wide FOV imaging typically have a low NA, which in turn leads to low resolution images. Ideally for wide FOV TIRF, an objective lens with a combination of low magnification and high NA is required for sub-cellular resolution imaging in three dimensions. However, despite the considerable advantages of prism-based TIRF, restrictions are imposed on specimen mounting. The cell culture surface must be directly in contact with the prism surface to allow for the propagation of the rapidly decaying evanescent field through the fluorescently labelled sample. With upright microscopes, the sample must be mounted between two coverslips rather than on a conventional slide.

While TIRF illumination is now widely used, the evanescent wave generally only penetrates less than 120 nm into the cell, such that only the basal membrane can be imaged. To overcome this limitation, the group of Tokunaga allowed sub-critical light to propagate into the sample to image at greater depths. This method termed Highly Inclined Laminated Optical (HILO) sheet microscopy allows for improved resolution while retaining the advantage of volumetric imaging [52].

Another technique of implementing TIRF at depth has been shown by Boulanger et al. [53]. In this work, the incidence angle of illumination is iterated throughout imaging, allowing the evanescent depth to reach around 800 nm while retaining the resolution afforded by the thinner constitutive evanescent fields. Azimuthal averaging was also employed to account for modulation artefacts inherent in evanescent illumination. Recently, TIRF has also been utilised for single molecule localisation microscopy

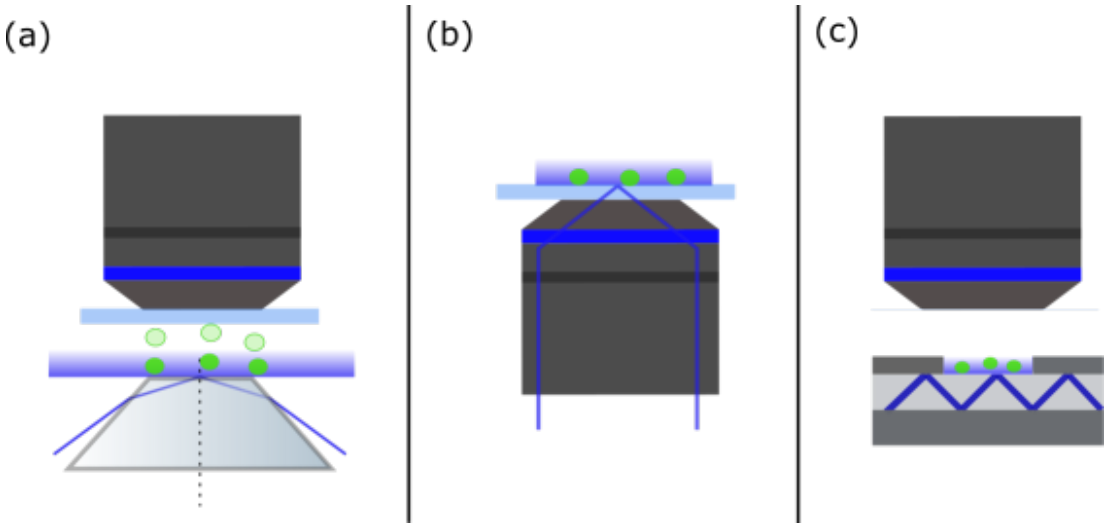

Figure 1.11: Three means of achieving TIRF illumination in microscopy: (a) prism [39], (b) TIRF objective [46] and (c) waveguide [51].

.

methods. For example, the technique of Point Accumulation In Nanoscale Topography (PAINT) combines localisation of fluorophores with TIRF illumination to resolve single molecules [54], [55].

1.6 Standing Wave Microscopy

A standing wave (SW) is a superposition of two counter-propagating waves which appear to be stationary, or standing, as the nodes (points of zero intensity, caused by deconstructive interference) and anti-nodes (points of maximum intensity, caused by constructive interference) are at fixed positions in space.

The first experimental detection of an optical standing wave was achieved by Otto Wiener in 1890 [12]. The beautiful, conceptually simple experiment involved coating a glass plate with a thin (roughly 20 nm) layer of photographic film and placing this atop a planar mirror surface at a small angle. He then illuminated this setup at normal incidence, allowing the incident and reflected waves from the monochromatic (or as monochromatic as possible in 1890) light source to pass through the photographic substrate. Following development of the film, Wiener observed that the film had blackened in the antinodal regions of the standing wave, allowing for the visualisation of fringes

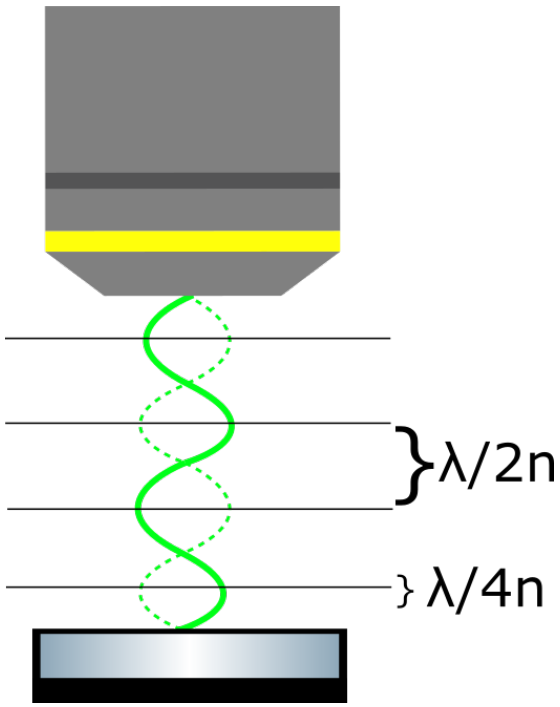

Figure 1.12: Illustration of a standing wave produced by light delivered through the widefield epifluorescence path of a microscope self-interfering via a mirror surface. Antinodal fringes shown as black solid lines separated by equation (1.28) with a thickness given by equation (1.29).

separated by fractions of the illuminating wavelength. A few years later, this experiment was repeated and expanded by Paul Drude and Walther Nernst [56] to capture this phenomenon using fluorescence contrast. Both of these experiments concluded that the generation of a standing wave was a result of the electric field vectors of the incident waves interfering with each other and that the magnetic field vector was not involved, [12].

Standing waves produced by the interference of two interacting planar waves have been utilised in fluorescence microscopy to achieve a simple form of structured illumination. The theoretical framework for the intensity profile of an excitation beam formed by the interference between two coinciding waves and its use in microscopy was initially provided by Lanni, [57]. For interfering beams of wavelength λ propagating through a specimen of refractive index n at an angle θ to the optical axis of the microscope separated by a phase shift of ϕ, the electric field intensity of the resultant interference pattern is given by equation (1.25).

$$I_{\text{ex}}(z) = 1 + \cos(Kz + \phi) \ , \tag{1.25}$$

$$K = \frac{4\pi n}{\lambda} \cos\theta \ . \tag{1.26}$$

For the case where this interference pattern of light is propagating through a fluorescently labelled specimen, fluorescence will only be excited in the anti-nodes of the standing wave (the areas of constructive interference) and dark minima bands will be observed in the nodes of the interference. The spacing between the anti-nodes, Δ_s can be expressed as a function of the physical parameters of the model,

$$\Delta s = \frac{\lambda}{2n\cos\theta} \ . \tag{1.27}$$

In the case of illumination along the optical axis of the microscope, the cosine dependence on the normal angle allows for minimising equation to the form,

$$\Delta s_{\text{min}} = \frac{\lambda}{2n} \ . \tag{1.28}$$

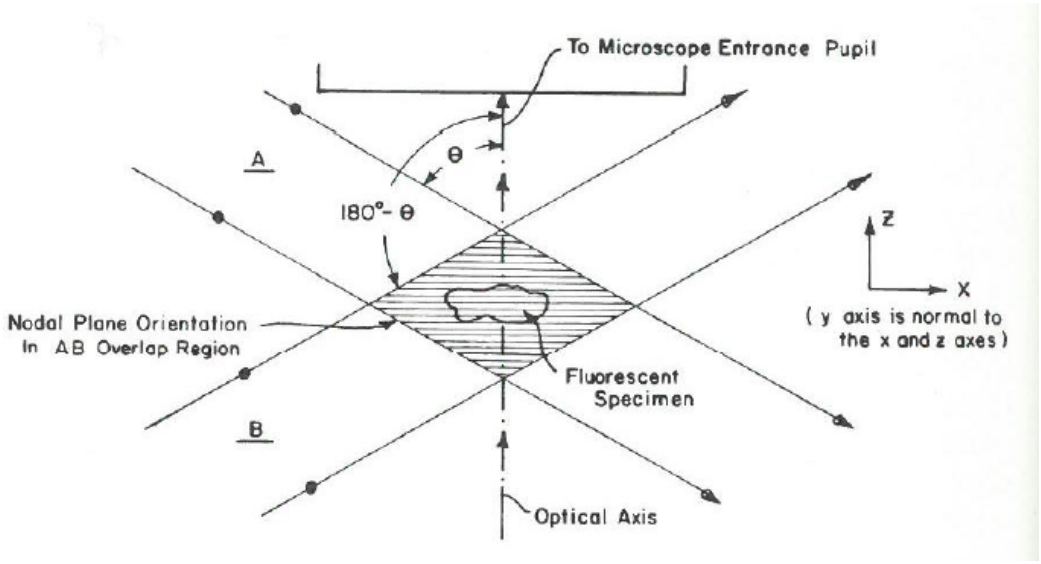

Figure 1.13: Interference between two counter-propagating waves at different angles to the optical axis of the imaging microscope objective, resulting in a region of standing waves (illustrated by bands showing the orientation of the standing wave antinodes). Reproduced from [57].

The thickness of the fluorescent fringes in standing wave illumination can be expressed as the full width at half maximum (FWHM) of the antinodal planes. Therefore, the fringe thickness, and axial resolution, can be expressed as

$$FWHM = \frac{\Delta s_{\min}}{2} = \frac{\lambda}{4n} \ . \tag{1.29}$$

There is a caveat to this theoretical model. The standing wave interference pattern which results from the excitation light will not be visible to the observer with appropriate emission filters in place. However, the standing waves which are excited will be products of the illumination light which will yield standing wave fringes in axial positions relative to the fluorescence emission light. Both the excitation and spatially modified fluorescent emission standing waves are characterised by equations (1.28) and (1.29), however, any measurements quoted in this thesis are considered from the detected emission pattern.

The initial experiments of Lanni [57] were performed with the illumination incident on the specimen at an oblique angle, as in Figure 1.13, meaning that the antinodal spac-

ing and thickness was not minimised. However, despite using relatively thick antinodal planes for excitation of fluorescence, the authors were able to image fringes in F-actin filaments in 3T3 cells labelled with rhodamine phalloidin.

The use of standing waves for the excitation of fluorescence in microscopy was extended from the basis set out by Lanni by Bailey et al., [26], where the authors demonstrated the imaging modality of SW microscopy with fluorophores labelling proteins involved with the structure and motility of cells, actin and myosin. This setup was significantly simpler than previous demonstrations, with only one light source used to produce a standing wave illumination pattern. By mounting the specimen of interest on a first surface reflector, a widefield epifluorescence microscope could be used to achieve standing wave illumination with a single excitation beam, which will reflect on the mirror surface, undergo a phase shift and then interfere with the incident beam, thus creating the standing wave illumination pattern.

Much more recently, researchers have combined mirror mounted SW microscopy with CLSM in order to achieve the background rejection, contrast improvement and optical sectioning synonymous with confocal imaging, [58], [59]. Amor et al. introduced a characterisation technique which will be utilised extensively in this thesis. Their work used a plano-convex lens specimen prepared with a monolayer of a fluorescent dye to model the antinodes of the generated standing waves. The principle here is the same as that employed by Wiener and Drude to use fluorescence to record the position and thickness of the antinodal fringes. However, with the added geometrical component of being able to relate the recorded fringes to their height from the specimen plane using the known geometry of the lens. Amor et al. also began the now much developed study of examining the morphology of red blood cells using SW microscopy, which this thesis extends (Chapter 4). This work was previously extended by Tinning et al., [60], where authors presented a method for high speed, widefield detection of red blood cells with computational reconstruction of the axial profile of the bi-concave structure of the cells.

In principle, the axial resolution improvement in SW microscopy gives rise to areas of information lost in the nodal planes of the excitation pattern. Using a single wavelength of illumination originating from the same axial positioned source results in

approximately 50% of the depth information of the specimen being lost, as shown by equation (1.28). However, if one could shift the position of these fringes, it would be possible to fill in the areas of information lost through the nature of illumination while retaining the high axial resolution and information on axial profile. As such, Schniete et al, [61], developed a technique termed TartanSW microscopy, where three illumination wavelengths of light, chosen to be within the excitation spectrum of the labelling fluorophore, were sequentially applied through the epifluorescence path of an upright microscope. Each of the wavelengths revealed detail from different heights within the specimen, allowing for the axial information gathered from the specimen to increase from 50% to 98% in TartanSW microscopy versus conventional SW microscopy. This work demonstrated the impressive ability of their technique to obtain three different standing wave patterns across a host of fixed, fluorescently labelled mammalian specimen, indicating the intricate axial profile of actin filaments and membrane of a handful of cells. The authors discuss the limitation of their system - one of which also applies to work contained in this thesis - which is that while axial information can be obtained from the specimen in this manner, the heterogeneity of cells and the configuration of their organelles renders reconstruction of the 3D morphology of the cell from this 2D standing wave data difficult. Consequently, 3D renders of SW microscopy datasets have not yet been performed.

A technique for shifting the positions of the antinodal fringes in space rather than varying the wavelength of illumination has been shown by Li et al [62] for the purpose of improving the axial resolution of a Structured Illumination Microscope (SIM), which demonstrates a characteristic two-fold improvement in lateral resolution. Li et al. used a piezoscanner attached to a mirror surface held in a custom mount above the imaged specimen in this work to shift the position of the antinodal fringes through the volume of the specimen.

1.7 Optical mesoscopy

Meso- is a prefix which means "middle" [63] and the field of optical mesoscopy came into being to address the fundamental limitation faced by both microscopy and macroscopy where a balance between field of view (FOV) that can be obtained and spatial resolution must be achieved. Mesoscopy retains high resolution across millimetre length scales by utilising bespoke optics or computational control of hardware. Several instances of mesoscopes have been demonstrated, and main current technologies will be reviewed here in brief.

The group of Sofroniew, [64], presented work to overcome the limitation of conventional microscopy to imaging neural activity. This custom two photon random access mesoscope (2p_RAM) enables high resolution imaging across a large field of view (5 mm $\times$ 1 mm) which corresponds to multiple regions in the mouse brains used to demonstrate the method. The 2p_RAM has cellular, near diffraction limited resolution (lateral: 0.66 µm and axial: 4.09 µm). This mesoscope was designed to have high 2 photon excitation efficiency over the wavelength range 900-1070 nm, which allows for excitation of green fluorescent protein and its spectral variants, which could have further applications in biomedical imaging beyond neural imaging. The crucial addition this mesoscope presents is the fast 3D scanning facilitated by the random access data sampling. 2p_RAM mesoscopes are now commercially available as units from Thorlabs.

The group of Stirman et al, [65], also found issue with conventional two photon microscopy as the standard imaging technique for neural imaging. Their solution involved splitting the beam path of a pulsed emission Ti:Sapphire laser and designing optics and scanning systems capable of extending the field of view to over 9.5 mm^2. Measures of resolution were reported as 1.2 ± 0.1 µm laterally and 12.1 ± 0.3 µm axially at the centre of the image, and 11.8 ± 0.4 µm at the edges, due to the curvature of field affecting the lens. The group performed extensive resolution and optical performance tests on their newly designed system which utilised commercial off-the-shelf components such that reproducing the system would not be too costly.

Ptychography is a scanning microscopy technique which utilises diffraction and

phase contrast in order to reconstruct images. It was first demonstrated by Faulkner and Rodenburg, [66], and allows for quantifying phase data that is not feasible in phase microscopy modes that can be added onto a conventional brightfield microscope (differential interference microscopy and Zernike phase contrast microscopy, [67]). Fourier Ptychographic Microscopy (FPM) employs ptychography by stitching together multiple low resolution images in Fourier space to obtain a higher resolution image. It is possible to use a low NA objective lens (e.g. 0.5, [67]) for FPM which in conventional brightfield microscopy would forfeit spatial resolution in favour of a larger FOV.

While FPM does allow for mesoscopic imaging with improved resolution, it is not well suited to applications where a small depth of focus (axial resolution in terms of image space) is required, as in optical sectioning methods. This technique is also computationally demanding and as such is not as widely utilised in biology as other methods.

While the mesoscopes discussed previously work very well with neural imaging they are very specialised. The 2p-RAM lens, [64], is only suited to IR wavelengths (900-1070 nm) and only in two-photon single spot laser scanning mode. The Trepan2p is also designed to work exclusively as a two-photon laser scanning microscope with an extended field of view, [65].

Selective plane illumination microscopy (SPIM) allows for mesoscopic imaging of samples of millimetre dimensions in optical sections via a set up with two objective lens; one for illumination and one for detection. Only a single focal plane (relative to the detection lens) is illuminated at any one time, so photobleaching across the sample is greatly reduced. SPIM was proposed as a widefield microscopy technique to overcome the issues of imaging faced by the high resolution, pixel-wise acquistion predecessors of CLSM and multi-photon microscopy, [68]. The group who first demonstrated SPIM in 2004 [68] showed a penetration depth of 500 µm into a fixed embryo, far exceeding the depth possible with a confocal microscope with a high resolution of 6 µm. The development of SPIM provided an alternative method of imaging biological processes in large living specimen at a much improved image acquisition speed. Optical sectioning is achieved in SPIM by the characteristic illumination process of only illuminating the

focal plane of the detector lens and then obtaining multiple images of the sample from different directions in order to build up a high resolution 3D image post acquisition. While light sheet microscopy techniques are very promising for mesoscopic imaging of large samples, their performance is based on the physical dimensions of the light sheet generated which are determined by the diffraction properties of light, [69].

A notable instance of mesoscale imaging for cellular biology is that of the mesoSPIM initiative [70]. MesoSPIM is a light sheet system which allows for imaging of bodies and organs up to 1 cubic centimetre with isotropic 6.5 µm resolution. MesoSPIM is entirely open source, allowing researchers to build their own system, with suitably thorough hardware and software documentation as well as a team of researchers who are eager for collaborations. At the time of writing, there are currently 17 mesoSPIM systems worldwide for light sheet imaging of cleared tissue. The mesoSPIM system uses a zoom lens, which supports imaging within FOVs of between 2 mm to 21 mm. However, a zoom lens has a variable NA which scales with magnification as does a conventional objective lens. Therefore, for the largest of the FOVs available to this system, spatial resolution is forfeited for the large imaging field.

1.7.1 The Mesolens

The Mesolens was designed to image full mouse embryos while retaining sub-cellular detail throughout its large imaging volume. The physical size and thorough testing of optical quality of each large Mesolens component gives rise to an optical throughput 25-fold higher than that of a comparable magnification microscope objective lens, [71]. This enhancement in optical throughput allows for a much-improved light collection efficiency over the large FOV afforded by the low magnification.

The Mesolens was designed to a lens prescription including an NA of 0.47, which for the chosen magnification of 4x is much higher than comparable magnification conventional objective lenses. Through equations (1.8) and (1.10) it is clear that decreasing N.A. somewhat affects lateral resolution but severely affects axial resolution (this is highlighted graphically in Figure 1 - supplement 1 of [71]). This specification of a high NA and a low magnification was chosen to allow for imaging of large tissue volumes

while retaining sub-cellular resolution.

Previous optical performance measurements of the Mesolens provided a lateral resolution better than 1 µm and a 7 µm axial resolution over the full 6 mm x 6 mm FOV and so is capable of sub-cellular resolution imaging over a large volume, with a working distance of 3 mm. The Mesolens was also designed with correction collars to adjust the position of the internal optics to refractive index match to the immersion fluids of water, glycerol and Type DF oil. This allows for imaging of a wider range of specimens, including live specimens in water (or in media with a comparable refractive index to water), than those suitable for single immersion fluid corrected objective lenses.

The Mesolens was designed with its 6 mm x 6 mm x 3 mm imaging volume because these dimensions match the size of a 12.5 day old mouse embryo. Imaging of this cleared embryo with all nuclei labelled with acridine orange and neurones labelled with AlexaFluor 594 was performed using confocal laser scanning mesoscopy with the Mesolens, and sub-cellular resolution imaging was proven [71]. Imaging of whole third instar larvae and adult *Drosophila melanogaster* was also performed with the Mesolens, [72], where the entire internal structure of the fly could be resolved, allowing for 3D identification of intact organs and extremities of a mesoscopic specimen.

Further developments to the already impressive ability of the Mesolens have involved the inclusion of high resolution imaging modalities. A computational method for speeding up the process of optical sectioning across the millimetre length scales of the Mesolens was introduced, [73]. Two different light sheet modalities were demonstrated, one based on Gaussian optics and the other generating an Airy-like illuminator [74]. Both of these methods dramatically speed up the process of capturing fluorescence from deep within a full organ or body with excellent optical sectioning. The Airy-like light sheet provided sub-cellular resolution in 3D comparable to laser scanning confocal mesoscopy at a 14 fold quicker imaging rate. With the improved axial resolution of the Airy-like light sheet for the Mesolens, Battistella et al. demonstrated the neuronal activity of an intact mouse brain under parasitic infection [75].

While the full lateral imaging field of the Mesolens is 6 mm x 6 mm, these dimensions are truncated slightly in widefield acquisition mode as we currently do not have camera

technology within the lab capable of capturing this full field at Nyquist sampling. As such, to capture the large, high-resolution images produced by MesoTIRF a chip-shifting camera sensor (VNP-29MC; Vieworks) which records images by shifting a 29-megapixel CCD chip in a 3 x 3 array was used [73]. Reconstruction of each image (260 Megapixels, 506 MB) takes approximately 5 s on a typical computer workstation. Recent innovations in camera technologies, notably the development of cameras using large, high resolution 250 Mpixel sensors such as the Canon 2U250MRXSAA CMOS sensor, tenfold higher imaging speeds (2.4 fps) can be achieved by avoiding the need for chip shifting. Additionally, sensor shifting technology has advanced in recent years, a new sensor shifting camera providing a 604 MPixel image with a 1.5 fps imaging speed is now commercially available (VNP-604MX-MC-6-H, Vieworks).

While the Mesolens is certainly a state-of-the-art, versatile means of imaging on the mesoscale with sub-cellular resolution, there are a number of other systems which demonstrate comparable abilities. The real-time ultra-large-scale high-resolution (RUSH) microscope [76] is another bespoke imaging system with a 8x/0.35NA lens prescription. This impressive system allowed authors to demonstrate a FOV of 10 mm x 12 mm, a resolution of 1.2 µm and due to the employment of a camera array of 35 scientific grade CMOS sensors, video rate imaging of 5.1 gigapixels per second was achieved. While RUSH does not have the same sub-cellular resolution of the Mesolens, the rapid imaging rate lends itself well to the mesoscopic study of fast, dynamic processes. The system has been demonstrated by imaging cardiomyocytes fluorescently labelled for the calcium activity [76] in the brains of awake mice. This has led onto work of high content drug screening for testing novel drug cardiotoxicities [77].

1.8 Super-resolution microscopy

The optical microscopy methods which have been expanded into the mesoscale as a result of the work of this thesis can be described as super-resolution techniques in their own right, as both TIRF and SW microscopy utilise diffractive and interference properties of light to bypass the axial diffraction limit of imaging objective lenses. Furthermore, TIRF is used for the illumination technique in all single molecule lo-

calisation microscopy (SMLM). As such, a brief review of the ever-expanding field of super-resolution microscopy is provided here.

As microscopy has developed as a field, microscopists have utilised phenomena in physics and chemistry in order to elucidate detail of biological structures and dynamic processes beyond the reach of a conventional optical microscope. This microscopy niche, broadly known as super-resolution microscopy or nanoscopy, [78], has evolved into a whole research field in its own right. Super-resolution microscopy enables the scientist to probe specimens previously only observable to electron microscopy or atomic force microscopy, without the rigorous preparation steps required by these techniques. Specialised fluorophores have allowed for the progression of photoactivable and photoswitchable localisation of single molecules, such as those employed in Photoactivated Localisation Microscopy (PALM), [79] , or Stochastic Optical Reconstruction Microscopy (STORM), [80], [81].

Structured illumination microscopy (SIM) [25] involves imaging with an intensity modulated illumination pattern. This pattern is shifted, rotated or translated to acquire nine images with different applied intensity patterns. These nine images can be used together with a computational method to produce images with twice the resolution of the original image. SIM has been further adapted in order to image multiple spectrally separate fluorophores with near isotropic resolution in 3D, [82].

By utilising the photonic properties of a high powered structured (donut-shaped) laser beam, scientists have shown that by "switching off", effectively forcing a fluorophore into a dark, emissive state, one can resolve detail on the order of about 30 nm laterally. This technique, Stimulated Emission Depletion (STED) microscopy, is also capable of localising a single molecule, [83]. Finally, a super-resolution technique which almost stands in its own category is the chemical technique of expansion microscopy. Here, a specimen is physically magnified using a hydrogel polymer and imaged using diffraction limited optics, [84].

Each of these super-resolution modalities is illuminated via one of three techniques; widefield, point scanning confocal or TIR, [78]. Of these, only the latter is in itself a super-resolution modality in its own right, and as such is the technique used for il-

lumination in single molecule localisation methods due to the improved contrast and out-of-focus fluorescence rejection. While a significant benefit to imaging with a confocal set-up, the out-of-focus fluorescence rejection observed here is not of a single optical section as in TIRF.

1.9 Overview of thesis

The aim of this work was to improve the axial resolution of the Mesolens. As mentioned in Section 1.7.1, the axial resolution of the Mesolens is nominally 7 µm. In this work, I developed two different approaches to perform imaging in 2D and 3D with higher axial resolution.

The first, and more hardware and optical development intensive, project spans two Chapters of this thesis. A prism based Total Internal Reflection Fluorescence (TIRF) illuminator for the Mesolens would overcome the bottleneck of the widely utilised TIRF microscopy which is the approximately 100 μm^2 FOV - a handful of mammalian cells in a single image - over which the axial super-resolution and contrast enhancement is observed.

Firstly, in Chapter 2, a prism based TIRF illuminator is built around the modified body of an upright Olympus microscope and fully characterised. In this Chapter, a key focus is put on accurately measuring the evanescent field depth of the beam undergoing TIR. Several issues are identified with the measurement of this feature of the illuminator and are discussed at length. However, the distinct characteristics of the evanescent field are measured and the imaging capability of this custom TIRF microscope illuminator is demonstrated.

In Chapter 3, the system designed in Chapter 2 is adapted, installed and demonstrated with the Mesolens. This modality, which we call MesoTIRF, is presented, alongside proof of concept MesoTIRF imaging of fixed, fluorescently labelled specimen and thorough characterisation of the imaging quality. A focus of this Chapter is the ability of the modality to discriminate structures near the basal membrane of the cell to organelles within the cytoplasm. The work of this Chapter is published, see Research Output.

Finally, Chapter 4 describes a project to improve the axial resolution limit of the Mesolens using Standing Wave (SW) illumination. The structure of a SW yields topographical information from the antinodal planes from a single 2D acquisition. By extending this illumination method across the 4.4 mm x 3.0 mm FOV of the Mesolens, we were able to demonstrate our fast 3D imaging technique across more than 100 fixed fibroblast cells and more than 16,000 live red blood cells. We also laid the groundwork for future SW mesoscopy work to screen for blood disorders, with a custom flow chamber system with a reflective substrate. The work of this Chapter is published, see Research Output.

Chapter 2

Development and characterisation of a prism TIRF prototype illuminator

2.1 Introduction

This Chapter focuses on the design, development and characterisation of a custom prism-based TIRF microscope, laying the groundwork for Chapter 3 where we have demonstrated TIRF mesoscopy. In this introductory section, I will provide a brief overview of the field of TIRF microscopy, leading on from Chapter 1.5, to highlight the lateral limitation of current TIRF systems. I will then describe our proposed means of expanding TIRF microscopy into the mesoscale to benefit from the axial super-resolution and enhanced image contrast synonymous with the technique over large populations of cells.

Total Internal Reflection Fluorescence (TIRF) microscopy is a staple imaging technique in cellular biology whereby an optical phenomenon is utilised to generate a thin sheet of excitation light that will only propagate to fluorophores within a few hundred nanometres of a refractive index boundary. The technique was introduced to biological imaging in the early 1980s by Axelrod et al, [39], who demonstrated the axial super-resolution and contrast enhancement of TIRF on adherent epithelial cells. The thin

field illumination of TIRF elucidated detail on contact regions between the membrane, tagged with a lipophilic fluorescent stain, and the growth substrate which was dwarfed by fluorescent signal deeper in the cell in widefield epifluorescence microscopy.

Since this introduction, TIRF has proved itself an invaluable tool for examining biological structure and processes occurring at the basal plasma membrane [85], studying cell adhesion after viral infection, [42], analysing calcium channel signals through cell ion channels, [86], and more recently as an illumination technique for lateral super-resolution methods, such as the various single molecule localisation microscopies that have been developed in recent decades, [87]. In its earliest and simplest incarnation, TIRF microscopy was achieved with a prism, [39]. Now, as a staple imaging technique in many cellular biology imaging facilities, the more common means of TIRF illumination and imaging is achieved with a commercial TIRF objective, which is available from most microscope manufacturers.

While the resolution and contrast improvement in TIRF is well understood and exploited, TIRF illumination is an inherently spatially restricted wide field imaging method. The nature of evanescent light restricts propagation axially and commercially developed TIRF objectives require high numerical apertures (1.4 - 1.5) to allow for steep critical angles to be achieved at the specimen plane, and so the imaging field is generally restricted to a diameter of around 50 µm. Sequential imaging is usually required to look at population properties and dynamics of specimens with improved axial resolution and contrast.

With the inclusion of TIRF as an illumination technique for lateral super-resolution microscopies, more compact, cost-effective means of achieving evanescent illumination have been demonstrated. Waveguide based illuminators utilise the refractive index difference between the waveguide core and cladding to achieve multiple, tunable area wells of evanescent excitation and when used in tandem with a TIRF imaging objective, lateral super-resolution microscopy can be achieved, [51], [54] . The decoupled illumination and detection of TIRF waveguides allows for any chosen imaging objective lens to be used and the comparison of dSTORM and entropy-based super-resolution imaging with waveguide illumination has been demonstrated with; (1) a low magnification/low

NA (20x/0.4) and (2) a higher magnification/NA imaging objective (60x/1.2), [49]. As expected, while evanescent illumination was still achieved across a 0.5 mm x 0.5 mm lateral field, the lower NA of the 20x objective loses the fine spatial detail afforded by dSTORM imaging with an appropriately high NA objective lens.

Despite the wide spread use of TIRF imaging, each of the current means of producing evanescent illumination for TIRF imaging suffers from a common limitation; the FOV is limited to a handful of cells. TIRF objectives prescriptively have high numerical apertures (NA $\geq$ 1.4) in order to ensure a high incidence angle at the specimen plane of the lens and while prism and waveguides can, in principle, be used with any chosen magnification imaging objective, these systems are subject to the diffraction limitations associated with conventional optics. A lower magnification objective lens yields a larger imaging field but the resolution associated with the associated NA is poorer, introducing a forfeit of resolvable detail for imaging more of a specimen simultaneously. This issue can be obviated slightly by taking many spatially separated smaller FOVs with a high magnification and NA objective lens (TIRF or otherwise) and stitching and tiling the images together post-acquisition. However, this technique is time intensive and routinely introduces artefacts into resulting tiled images if registration between frames is faulty. This trade-off between the FOV illuminated simultaneously and the production of a high quality evanescent field underpins the work of this Chapter. The largest lateral FOV available to TIRF objectives is currently $<$ 1.4 mm x 1.4 mm with, for example, 16x/0.8NA, 25x/1.1NA or 25x/1.05NA objectives available from Nikon, Leica and Olympus respectively.

The approach explored here aimed to combine TIRF illumination with the Mesolens, [71]. The Mesolens has an unusual lens prescription that produces a low (4x) magnification and a relatively high (0.47) NA with chromatic correction across the visible spectrum and spherical aberration correction using multiple correction collars. This produces a 4.4 mm x 3.0 mm FOV in widefield illumination and an imaging volume of 6.0 mm x 6.0 mm x 3.0 mm with confocal optics, with a lateral resolution of 700 nm afforded by the comparatively high NA (the NA of a conventional commercial 4x objective is generally $\simeq$ 0.1). TIRF illumination would allow for imaging below the

current axial resolution of 7 µm of the Mesolens, utilising the characteristic 100-300 nm evanescent field depth to elucidate detail lost or blurred in widefield epi-illumination.

However, while the principle of this project was to develop an existing means of illumination (prism-based TIRF) for an established optical system (the Mesolens), the small clearance ($\sim$ 10 mm) between the front element of the precision stage (ProScan III, Prior Scientific) and the access limitations of the much utilised Mesolens, a prototype prism-based TIRF illuminator was first designed and built around the modified body of an upright microscope system, was fully characterised before being adapted and moved to the Mesolens (which will be discussed in full in Chapter 3).

Design of a prototype MesoTIRF illuminator necessitated certain parameters. Firstly, a prism based means of illumination was required because a TIRF Mesolens (as a analogue for a TIRF microscope objective) was both impractical and potentially physically impossible. The design, careful testing and manufacture of a Mesolens (as described [71]) takes years of expert work at a high financial cost, when compared with an inexpensive prism and a series of commercially available optics. Unlike microscope objectives, the back focal plane of the Mesolens, where one would have to focus a laser beam off-axis in order to achieve a TIR at the specimen plane of the lens, is not well defined. As such, it is not feasible to produce TIR in this way. We did not have convenient access to waveguide fabrication equipment and as such went down the prism illumination route.

Secondly, each component in the illumination path of both the prism TIRF prototype system and the MesoTIRF modality had to be compatible with the visible wavelength corrected optics of the Mesolens. As such, each optical component is anti-reflection coated between 350 nm - 700 nm and the dove prism (Mesolens Ltd.) was fabricated from the same borosilicate glass as the Mesolens to ensure refractive index matching.

Thirdly, as the Mesolens in conventional widefield and confocal mode is in routine use by other researchers, the optics of the prototype and MesoTIRF illuminator had to be fully removable from around the specimen stage and therefore be optimised to require as minimal an amount of realignment as possible.

This Chapter will discuss the design, implementation and testing of the prototype system alongside a full discussion of the evanescent characterisation of the modality. An in-depth description of an eventually abandoned method for measuring evanescent field depth, alongside the custom analysis pipeline developed, will also be presented.

2.2 Methods

2.2.1 Custom TIRF illuminator setup

The prism based illuminator developed in this work was set up as shown in Figure 2.1. The prism used was a BK7 dove prism (Mesolens Ltd) of height 25 mm. The prism was mounted on a translation stage for setting the height of the prism relative to the objective. The body of an Olympus BX50WI upright microscope was modified by removing the existing stage and incorporating the prism below the objective lens.

The epifluorescence pathway of this microscope was fitted with a CoolLED pE-300 Ultra light emitting diode engine with a green LED (central wavelength 575 nm with a FWHM of 120 nm) to allow for comparison with the developed TIRF mode. A 532 nm 5 W maximum output power (Verdi V5, Coherent) was used for TIRF illumination. The full power of this beam mostly undergoes TIR and does not reach the sample plane.

A 532 nm dichroic filter (Di01-R532-25x36, Semrock) and a 561 nm long pass filter (FF562-Di03, Semrock) mounted in the imaging pathway of the microscope allowed spectral filtering of fluorescent emission. A scientific CMOS camera (Zyla 5.5, Andor) with a 1-2 s exposure time was installed on the camera port. An aperture A was included directly after the laser (see Figure 2.1) as a spatial filter. Periscope mirrors (M1-3) guided the beam to the gimbal mirror (GM) (GMB1/M, Thorlabs) which was used to control the incidence angle of the beam entering the prism (P).

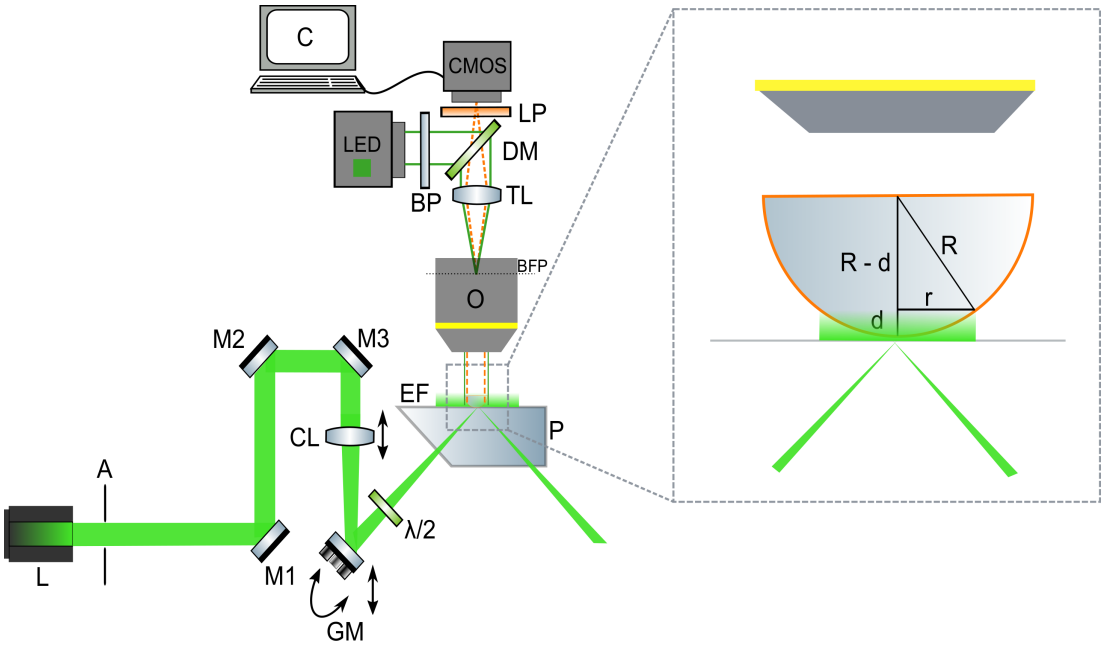

Figure 2.1: ,
A: aperture, M1-3: broadband dielectric mirrors [BB1-E02, Thorlabs] on periscope mounts [RS99, Thorlabs], CL: 100 mm cylindrical lens [LJ1567RM-A, Thorlabs], GM: gimbal mounted [GMB1/M, Thorlabs] broadband dielectric mirror, λ/2: half wave plate [WPH10E-532, Thorlabs], P: N-BK7 glass prism [Mesolens Ltd.], EF: evanescent field, O: objective [UPlanSApo10X/0.4NA or PlanN4X/0.1NA, Olympus Life Science] on a Olympus BX50WI upright fluorescence microscope body, TL: 180 mm tube lens [Olympus Life Science from Edmund Optics #36-401], LED: LED set [CoolLed pE-300ultra], BP: 531 nm single band band-pass filter (FF01-531/40-25, Semrock), LP: 561 nm long pass filter [LP02-561RU-25, Semrock], DM: dichroic beamsplitting mirror [FF562-Di03-25x36, Semrock], CMOS: scientific CMOS camera [Andor Zyla 5.5] attached to computer C running acquisition software WinFluor. Inset: Schematic of fluorescently labelled lens specimen of radius of curvature R excited by evanescent illumination with decay parameter d.]Optical set up of prism based TIRF, L: 532 nm, 5 W DPSS laser [Verdi V5, Coherent], A: aperture, M1-3: broadband dielectric mirrors [BB1-E02, Thorlabs] on periscope mounts [RS99, Thorlabs], CL: 100 mm cylindrical lens [LJ1567RM-A, Thorlabs], GM: gimbal mounted [GMB1/M, Thorlabs] broadband dielectric mirror, λ/2: half wave plate [WPH10E-532, Thorlabs], P: N-BK7 glass prism [Mesolens Ltd.], EF: evanescent field, O: objective [UPlanSApo10X/0.4NA or PlanN4X/0.1NA, Olympus Life Science] on a Olympus BX50WI upright fluorescence microscope body, TL: 180 mm tube lens [Olympus Life Science from Edmund Optics #36-401], LED: LED set [CoolLed pE-300ultra], BP: 531 nm single band band-pass filter (FF01-531/40-25, Semrock), LP: 561 nm long pass filter [LP02-561RU-25, Semrock], DM: dichroic beamsplitting mirror [FF562-Di03-25x36, Semrock], CMOS: scientific CMOS camera [Andor Zyla 5.5] attached to computer C running acquisition software WinFluor [88]. Inset: Schematic of fluorescently labelled lens specimen of radius of curvature R excited by evanescent illumination with decay parameter d.

The gimbal, mounted on a translation stage affixed to a bench tower, allowed for an angular range of 48°- 80° at the normal to the prism top face. A 50 mm cylindrical lens (CL) (LJ1695RM-A, Thorlabs) was affixed to a height adjustable mount between the final periscope mirror and the gimbal mounted mirror to focus the laser to a line profile at the sample plane and thus fill the microscope FOV. The position of this lens was moved with changing incidence angle to correct the focus of the beam at the specimen plane. A zero order half-wave plate (λ/2) (WPH10E-532, Thorlabs) was included to vary the polarisation of the beam and analyse the effect of this variation on evanescent power.

2.2.2 Depth of evanescent field

To examine the evanescent field depth with a non-biological model system, we proposed working with a fluorescently labelled lens specimen previously utilised for standing wave microscopy 3D reconstruction of a 2D image [58]. In an attempt to measure this depth experimentally, a prepared lens specimen was placed convex-side down on the top surface of the prism. A portion of the curved surface of the lens was illuminated by the super-critical illumination, and the known geometry of the lens was used to measure the depth d, as in the lens specimen inset in Figure 2.1.

If the convex surface of a plano-convex lens specimen (with dimensions appropriate for the working distance of the imaging objective lens) is coated with a monolayer of a fluorescent dye and then illuminated by a prism generated evanescent field, the field depth can be calculated from known parameters of the lens specimen, [58]. Emission from the apex of the lens specimen with radius of curvature R will yield an imaged 2D fluorescent spot of radius r, allowing depth to be calculated by

$$d = -\sqrt{R^2 - r^2} + R \; . \tag{2.1}$$

By modifying a coating protocol described by Amor et al, [58], lens specimens (of focal lengths 30 mm, 48 mm and 72 mm) were prepared by coating the 6 mm diameter uncoated BK7 plano-convex lenses of a known radius of curvature (Edmund Optics) with a monolayer of the fluorescent dye Atto 532 NHS-ester (Sigma-Aldrich

88793). The lenses were cleaned with dry acetone and submerged in a 2% solution of (3-Aminopropyl)trimethoxysilane (Sigma-Aldrich 281778) in dry acetone for 6 hours. The lenses were then removed and rinsed with dry acetone. A 10 µM solution of Atto 532 NHS-ester was prepared in phosphate buffered saline (PBS). The lenses were submerged in this solution, protected from light and left on a platform rocker to uniformly coat. After 12 hours, the lenses were removed from the dye, cleaned with dH_2O, blow dried and protected from light until imaging.

The angle of the gimbal mirror was incrementally increased to vary the incidence angle of the beam and thus determine the effect of incidence angle on the depth of the resulting evanescent field. The field generated by the super-critical laser beam illuminated a characteristic portion of the fluorescent lens surface, and the recorded 2D image of the emission was a small bright spot a few hundred microns in diameter. The radius of this spot and the radius of curvature of the lens specimen allow for a measurement of d. The extraction of the radius from the image data is a somewhat involved process over the two open source programs of ImageJ, [89], and Python. Here, two different Python analysis pipelines will be presented; one which involves a more manual approach and a second which is automated and self-contained.

2.2.3 Image data processing and analysis

Background correction was achieved in ImageJ, [89], by taking an image without illumination light using the same camera settings. The relation (2.1) only holds if the collected fluorescence was excited at the apex of the lens. To ensure this, the background corrected TIRF image was registered against an epifluorescence image of the same lens specimen. Reflection between the prism surface and the lens specimen under epifluorescence illumination produced a concentric circular standing wave, the centre of which marks the apex of the lens specimen. Registration was achieved by cropping a region of interest around the first three antinodes of the standing wave and cropping this ROI from the TIRF image. A wide line profile (line width = 50 pixels) was drawn through the fluorescent spot as a quick means of averaging the signal. This profile was saved as a .csv file, and the process was repeated for the images with varying incidence

angle.

A simple script written in Python (Appendix A A.0.1) allowed for a quick extraction of the FWHM of the fluorescent spot. By fitting a Gaussian to the line profile through the centre of the fluorescent spot data, the noise in the data was smoothed out and, using the SciPy function *UnivariateSpline*, [90], to find the roots of the Gaussian at half the maximum fluorescent intensity, the FWHM of the data was obtained. The radius was determined by halving this a value and a geometric measurement of depth, (2.1), was then possible. The error on this depth measurement arose from the quadrature sum of the error on the focal length of the lens specimen (quoted by the manufacturer) and the RMS error from the Gaussian fit to the line profile data. The measured depth was then compared against the theoretical value obtained from (1.13) for the same incidence angle and refractive indices of the prism and air interface.

As the measured data is convolved with the point spread function of the objective lens used where the theoretical data is not, the same data set was deconvolved in ImageJ, [89], by extracting a PSF using the plugin 'PSF Generator' and running this through the ImageJ plugin 'DeconvolutionLab2' [91] with the cropped TIRF image. The analysis pipeline in ImageJ and Python described above was followed with the deconvolved data. The second approach in Python involved a slightly more automated procedure, which loaded the full lens specimen image into Python without having to manually draw line profiles in ImageJ (Appendix A A.0.2). A binary mask function written by Nicholas Hall (see Appendix A) was used to mask and analyse an annulus from the centre of a square image, increasing the annulus radius iteratively until the entire image was masked. In every annulus, the script calculated the average intensity within the mask and saved this value in an array indexed by the radial extent of the mask. Following repetition of the procedure for the whole image, a radial profile was obtained and the process described previously for obtaining the FWHM of this profile and hence the evanescent field depth was carried out.

Additionally, 15 µm diameter polystyrene beads with a multi-fluorescent coating (Polysciences Ltd.) were also used to probe the evanescent field depth. This method is most routinely used to characterise evanescent field depth for instances where this

property is fully characterised by users imaging with TIRF objectives.

2.2.4 Evanescent power with varying incidence angle

To provide another means of characterising the illumination as evanescent beyond the suggested depth measurement technique discussed above, power at the specimen plane was measured by recording power at the top prism face in Figure 2.1 as incidence angle was varied. A power meter (Nova II, Ophir) with average readings taken over 3 seconds was used. The incidence angle (θ_i) was increased from 50° to 78° in 3-4° steps by changing the pitch of the gimbal mounted mirror. The raw data were logarithmically scaled and fitted with a straight line to evaluate against exponential expectation. Fitting was performed in Python, using a least squares method in the NumPy class Polynomial. Uncertainty values were calculated from the goodness of fit (see Appendix A.0.3).

2.2.5 Evanescent power with varying polarisation angle

A power meter (Nova II, Ophir) was again used to evaluate proportional power values to (1.14) experimentally, as a further cross validation that the illuminator was indeed producing an evanescent field. A measurement was recorded for 10° rotations of $\lambda/2$, repeating for varying incidence angle. Re-alignment of $\lambda/2$ with respect to the gimbal mirror was carried out with changing incidence angle to ensure any changes in power measured were indeed down to the evanescent properties of the field and not misalignment in the optical path. A linearly polarised beam passing through a zero order half wave plate that was incrementally rotated about the optical axis should have a sinusoidal output power signal, with the peaks and troughs representing p- and s-polarised light intensity respectively. Python was used to plot and measure the power deviation between the peaks and troughs of the data and compare to the theoretical deviation in intensity.

2.2.6 Demonstration of TIRF prototype for fluorescence microscopy

While the proposed depth of evanescent field measurement will be shown to have some issues, the setup was successfully imposing TIR on the incident beam and therefore

should, in principle, be producing an evanescent field as a result. Measurements of power in the evanescent field with varying parameters described in the previous two sections will also consolidate this assumption. Therefore, we chose to use the optical set up to illuminate and image a series of fluorescently labelled specimens to test its ability to act as a TIRF illuminator.

Mammalian cell imaging

Cells of the human breast cancer immortalised cell lines MCF-7 and HeLa were maintained in culture, at 37°C, 5% CO2 in DMEM and RPMI respectively, see Appendix B for full media recipes used.

For fluorescence imaging of fixed samples, coverslips were coated in a 1:500 dilution of fibronectin bovine plasma (F1171-2MG, Sigma Aldrich) in PBS (10010-023, Gibco) prior to seeding and grown in culture conditions for 24 hours (or until visible protrusions from the cell membrane to the coverslip where visible under a 4X/0.1NA objective lens in brightfield). The adherent cells were washed twice with PBS and fixed in freshly diluted 4% paraformaldehyde. For direct fluorescent labelling of structures such as cell nuclei (with DAPI or SYTO dyes) or F-actin (with phalloidin conjugated fluorophores), a working solution of the dye was prepared in the imaging media at the concentration recommended by manufacturers and incubated at room temperature for no longer than 1 hour. Following this time, the labelled specimens were washed three times in PBS before mounting.

For antibody labelling, an immunofluorescence (IF) buffer solution (PBS, 2.5% FBS and 0.3% TritonX-100 (X100-100ML, Sigma Aldrich)) was applied to the fixed cells to both block non-specific binding and permeabilise the cell membranes, for 30 minutes at 37°C. This buffer was replaced by a 1:250 dilution of the desired primary antibody against paxillin (Y113, anti-rabbit, ab32084, AbCam; or 5H11, anti-mouse, MA513356, Invitrogen) or alpha-tubulin (anti-mouse, T6199, Merck) in IF buffer. These coverslips where kept in a stable humidity culture dish, to prevent evaporation, for 24 hours at 4°C. The following day, the primary antibody labelled cells were washed three times with PBS before a 1:200 dilution of the appropriate secondary antibody in IF buffer

was applied (Alexa Fluor 488 donkey anti-rabbit secondary, A21206 Invitrogen, Alexa Fluor 488 donkey anti-mouse secondary, ab150105, Abcam or Alexa Fluor Plus 594 goat anti-mouse secondary, A32742, Invitrogen). The coverslips where kept in light tight conditions at room temperature for 1 hour. Following three further PBS washes, cells were mounted using gelvarol mountant. As discussed in Chapter 3, this was eventually changed to 1% agarose to ensure a known refractive index but existing mountant media were sufficient here for TIRF test imaging. These samples were allowed to dry fully at 4°C in the dark before imaging.

Microbiological imaging

As the Mesolens does not currently have environmental controls which would support long term imaging of live mammalian specimens under physiological conditions, one of the driving motivators for live cell TIRF imaging with the Mesolens was using bacterial specimens which could be achieved at room temperature. As such, further biological test imaging was carried out with the TIRF prototype microscope illuminator with microbiological specimens to elucidate the capability of the developed prototype for TIRF imaging. *E. coli* cells (strain DH5-α) with an pRed_Broccoli plasmid in the pUC57 background were kindly provided by Paul Hoskisson (University of Strathclyde). Upon induction with IPTG, mCherry fluorescence is driven from the T7 RNA polymerase promoter. The fluorescence induced is cytosolic and coupled with the low magnification of the objectives used in the prototype, the benefit of moving from widefield epifluorescence to TIRF is not as obvious from this imaging as it is with the larger, more localised fluorescence from the antibody labelled mammalian cells discussed previously.

2.2.7 Photobleaching decay analysis

The nature of the optical sectioning ability of TIRF illumination localises the depth of the fluorescent specimen that is photobleached during imaging. As such, a further expectation of the prototype behaving as a TIRF illuminator was a reduction in photobleaching rate in TIRF mode versus widefield epifluorescence under the same image acquisition parameters. Duplicate fixed mammalian cell specimens were fluorescently

labelled as described above and imaged under equivalent illumination and acquisition parameters in both techniques.

To quantify the photobleaching rate, ImageJ was used to manually threshold the first frame of the time series to segment the fluorescent signal from background. This thresholded value was converted into a Selection which allowed for a measure of the signal in this region to be calculated from each frame of the time series.

This data was exported from ImageJ as .csv files, loaded into Python, where plotting and fitting of the data was carried out.

2.3 Results

2.3.1 Depth of evanescent field

The protocol described for lens specimen preparation and imaging in Chapter 2.2.2 was performed for various 6 mm diameter lens specimens. In the first instance, imaging of a 37.22 mm radius of curvature, 72 mm focal length lens was performed for 48°, 52°, 55°, 58°, 62°, 65°, and 72° incidence angles by adjusting the angular tilt of the final mirror element in Figure 2.1. Three of these images, separated by 10° are shown in Figure 2.2.

By eye, it is evident that the fluorescent spot size does decrease with increasing incidence angle as expected from theory. By computing the radial average of these fluorescent spots and evaluating the full width at half maximum (FWHM) of the distribution shown in the lower three panels of Figure 2.2, a numerical value for r, the averaged radius of the spot, was determined. By plugging this value into equation (2.1), the plot shown in Figure 2.3 was obtained for this measurement with increasing incidence angle. It is clear that there is not complete agreement between theoretical expectation and experimental measurement for the decay parameter d of the evanescent field. It should be noted that the theoretically calculated field depth is an idealised situation described by equation (1.13). The deviation between experimentally measured field depth and theoretical expectation may partially be accounted for by the convolution of the evanescent field depth with the point spread function of the imaging

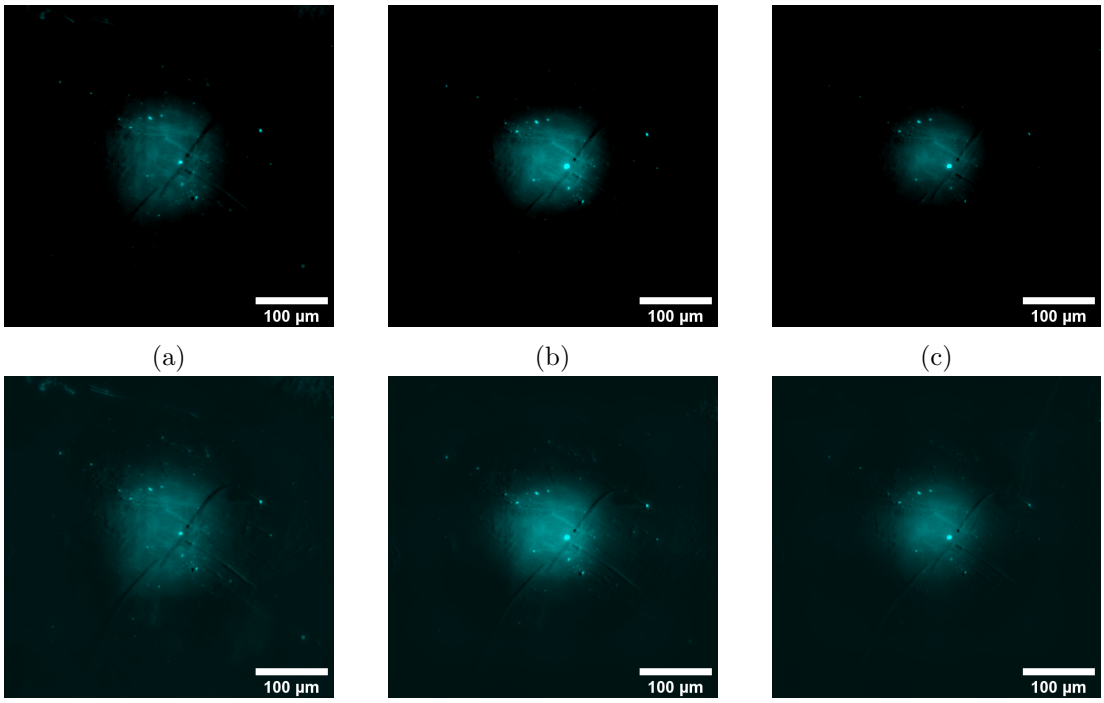

(a) (b) (c)

(d) (e) (f)

Figure 2.2: 72 mm focal length lens specimen labelled with Atto 532 NHS-ester illuminated with increasing incidence beam. Radius of curvature R = 37.22 mm. 2.2a-2.2f: Images undergone background subtraction and cropping. 2.2a-2.2c: Images 2.2a-2.2c following deconvolution using DeconvolutionLab2. For both raw and deconvolved image sets, a subtle decrease in spot diameter can be seen with increasing incidence angle.

objective lens. To this end, deconvolution of the lens specimen images was performed in ImageJ using DeconvolutionLab2 from EPFL [91] (images in panels 2.2d - 2.2f of Figure 2.2) and the analysis pipeline was run again. However, in this instance, the process of deconvolution appears to have minimal effect on the radius of the fluorescence spot measured, as seen by the very similar plots in Figure 2.3 (a) and (b).

The discrepancy of theory versus measurement, which cannot be accounted for by convolution of the fluorescence light by the imaging objective lens, here prompted further experimental and analytical investigation.

Firstly, the same imaging and analytical protocol as described above was repeated for a different lens specimen of focal length 48 mm and radius of curvature 24.81 mm. The resulting images are shown in Figure 2.4.

The images in this instance, while still retaining the same trend of shrinking fluo-

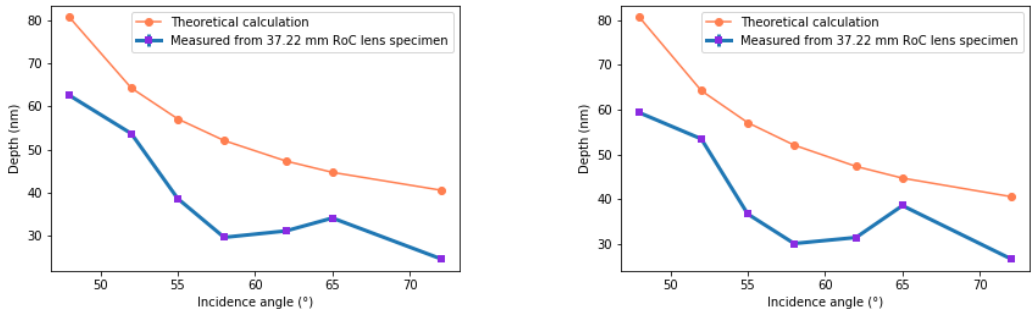

(a) (b)

Figure 2.3: Depth measured from coated 72 mm focal length lens specimen against supercritical incidence angle for raw (a) and deconvolved images (b). Theoretical plot obtained using (1.13) with experimental incidence angle.

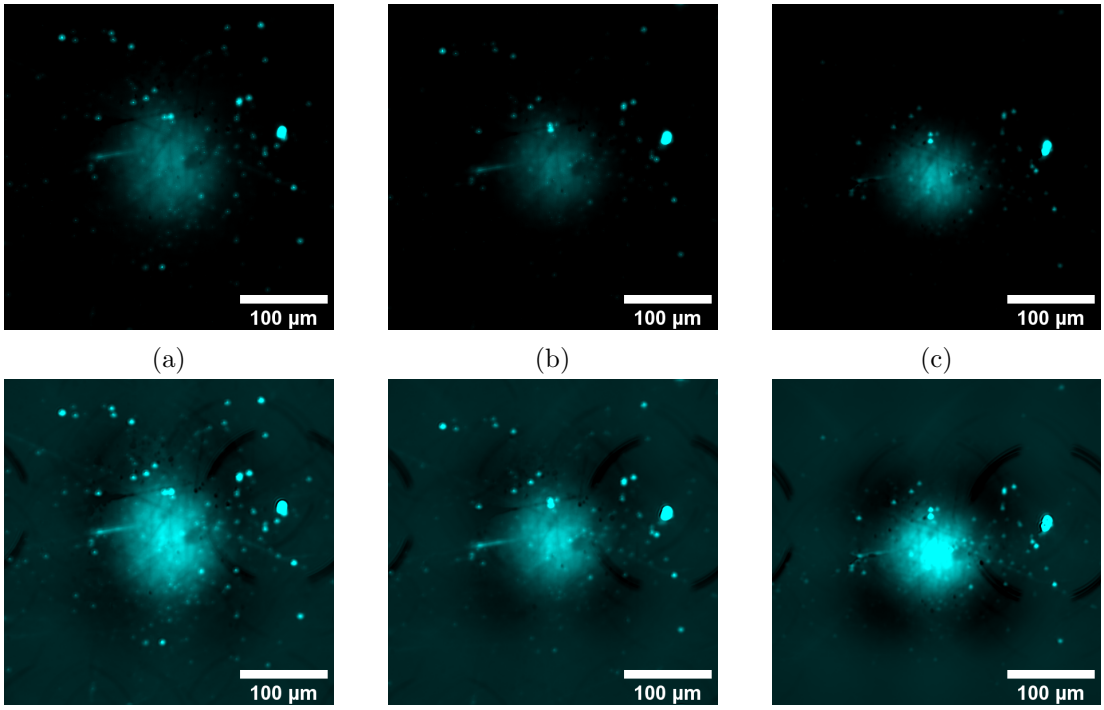

(a) (b) (c)

(d) (e) (f)

Figure 2.4: 48 mm focal length lens specimen labelled with Atto 532 NHS-ester illuminated with increasing incidence beam. Radius of curvature R = 24.81 mm. 2.4a-2.4c: Images undergone background subtraction and cropping. 2.4d-2.4f: Images 2.4a-2.4c ran through DeconvolutionLab2.

rescent spot for increasing incidence angle, the lens surface prepared under the same APTMS and dye coating protocol were less uniform than those illustrated in Figure

2.2. This appears to skew the analysis quite heavily which takes direct measurements of the FWHM, particularly in the deconvolved case where the speckled background of dye clusters is more prominent (Figure 2.4d- 2.4f). The resulting measurements are presented in Figure 2.5.

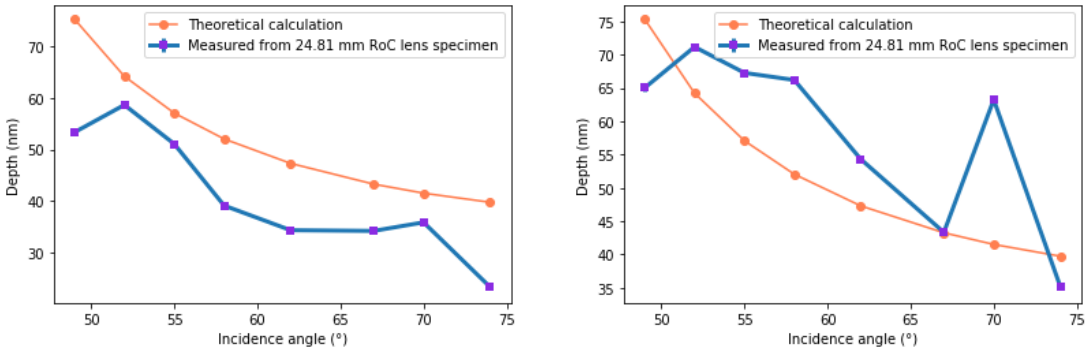

Figure 2.5: Depth measured from coated 48 mm focal length lens specimen against super-critical incidence angle. Theoretical plot obtained using (1.13) with experimental incidence angle.

The measurement obtained from the raw image data agrees well with the result from the previous lens specimen, with the same deviation which could be partially accounted for by the convolution of the fluorescence emission through the objective lens. However, after deconvolution, the artefacts within the resulting image significantly alter the measurements. This instigated an adapting of the analysis pipeline to remove some of the manual extraction of raw data, into the second code described in Chapter 2.2.2. This code produced a result from direct measurement of a Gaussian fit to find the FWHM of the intensity signal alongside an interpolation to find the same value (Appendix AA.0.2).

Following an observation of fluorescent residue on the prism surface post imaging, repeat imaging with the same imaging parameters of the same lens specimen was carried out. This repeat imaging and analysis pipeline was replicated for three varying radius of curvature lens specimens (15.5 mm, 24.81 mm and 37.22 mm).

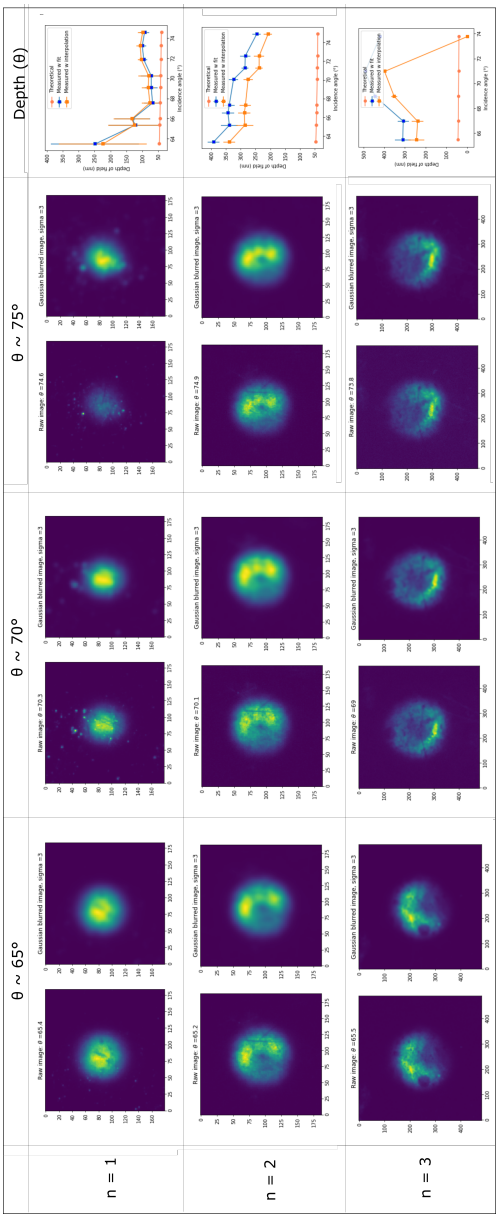

Figure 2.6: Repeated (where n denotes repeat number after preparing lens) depth measurement with Python script #2 (A A.0.1) with a 15.5 mm radius of curvature lens specimen

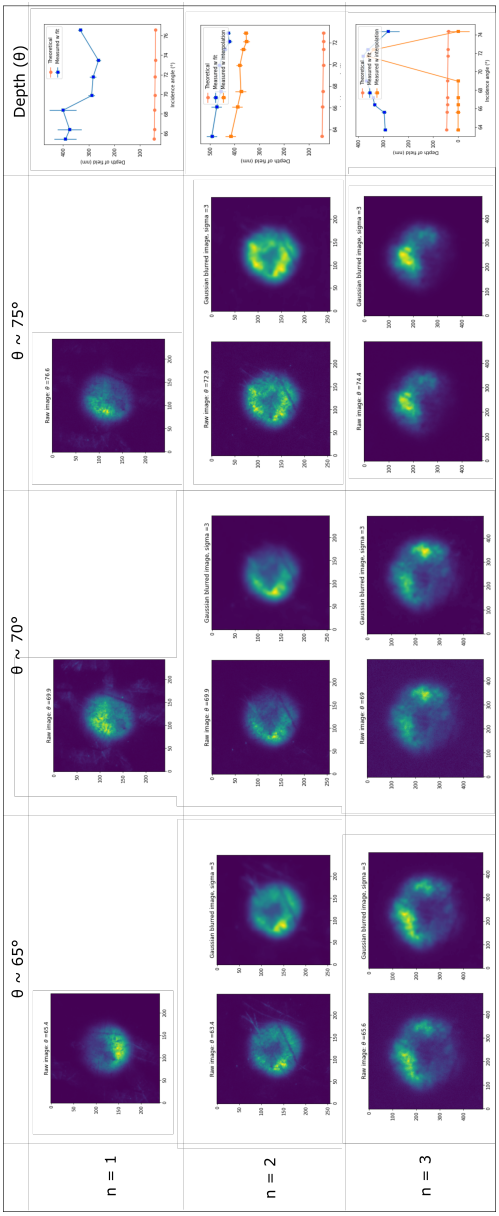

Figure 2.7: Repeated (where n denotes repeat number after preparing lens) depth measurement with Python script #2 (A A.0.1) with a 24.81 mm radius of curvature lens specimen

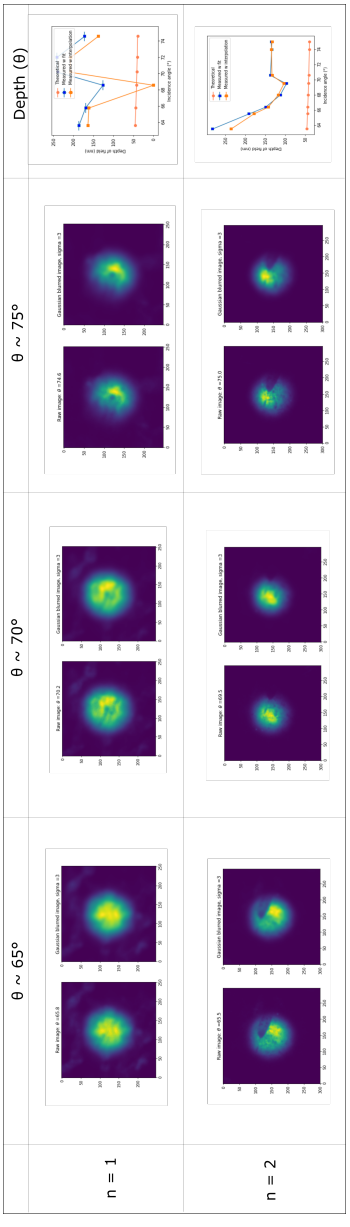

Figure 2.8: Repeated (where n denotes repeat number after preparing lens) depth measurement with Python script #2 (A A.0.1) with a 37.22 mm radius of curvature lens specimen

These repeated measurements indicated several issues with the proposed depth measurement technique. Firstly, it appeared the imaging was damaging to the fluorescent monolayer. To test this, epifluorescence images of the lens surface at the same focal plane where the TIRF excited spot was visible were obtained prior to and following TIRF imaging to observe any bleached regions, and the lens was then placed on a first reflector mirror surface and the focal plane of the objective was adjusted such that the bleached region relative to the apex of the lens was observable. These data for the 30 mm focal length lens discussed above are shown in Figure 2.9. Measuring the diameter of the TIRF excited spot in 2.9(a) yields a value of 416.9 µm which leads to an evanescent depth measurement of 1.6 µm. The epifluorescence check of the lens surface following this, without changing the focal plane of the objective lens, obtained the image shown in 2.9(b). The diameter of this bleached dark spot was measured as 419.2 µm, indicating that the TIRF-regime imaging did indeed photodamage the area of lens where the generated field interacted with it. The very short (exposure time = 300 ms) time window between the lens being coated, imaged in TIRF and then bleached in this spot size an order of magnitude lower than the beam waist of the laser used to excite fluorescence is suggestive that we are in or close to a TIRF regime with the designed setup but that the laser may be coupling into the lens at the interface between the convex surface and the prism and propagating much deeper into the specimen than a TIRF field would ordinarily. In Chapter 3 of this thesis, further methods to answer the question of whether we are operating in a TIRF regime are described in detail.

Ultimately, this led to irreproducible evanescent field depth data with this method which is why the rest of this Chapter and thesis will discuss very different characterisation techniques. In principle this method could work if one could have a lower refractive index planoconvex lens specimen (lower with respect to the glass of the prism, n = 1.51) and refractive index matched to its surroundings as the light coupling into the lens is a physical limitation that proved difficult to avoid with the experimental setup described here.

Furthermore, when the same principle for measuring field depth was examined using micron diameter commercially available beads, refractive index mismatch appeared

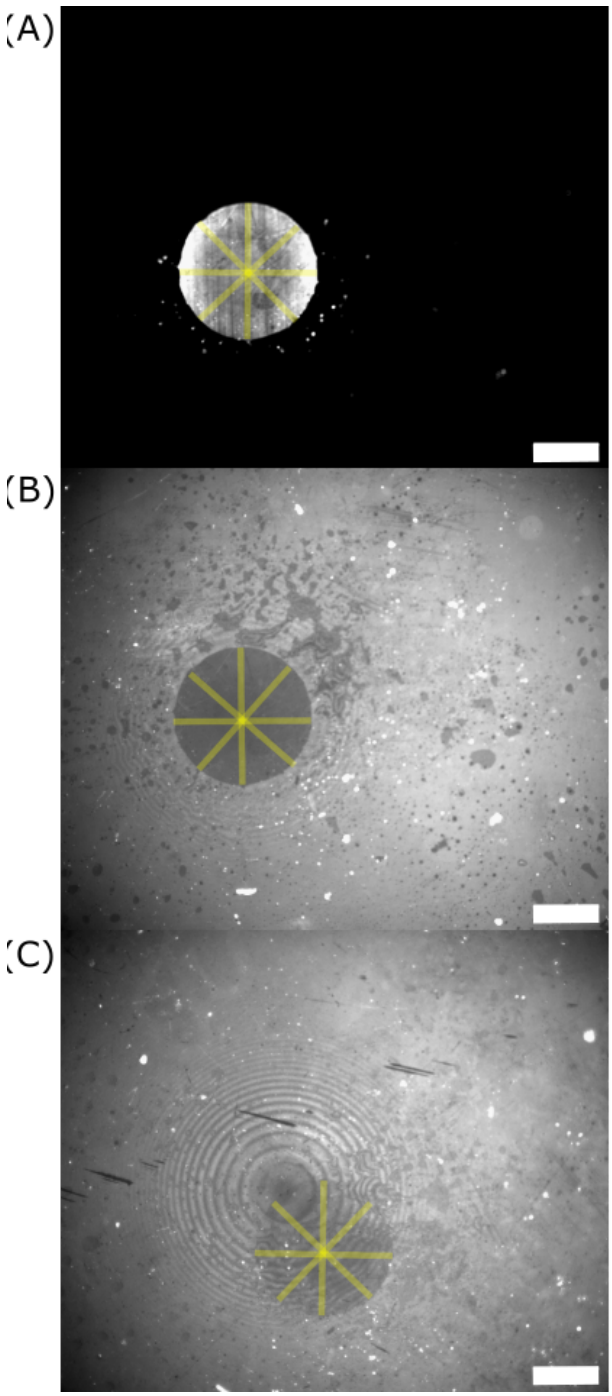

Figure 2.9: (A) 30 mm focal lens under TIRF excitation, (B) same field as (A) imaged in widefield epifluorescence, (C) same lens placed convex side down on a mirror to identify the apex of the lens. Scale bars = 200 µm

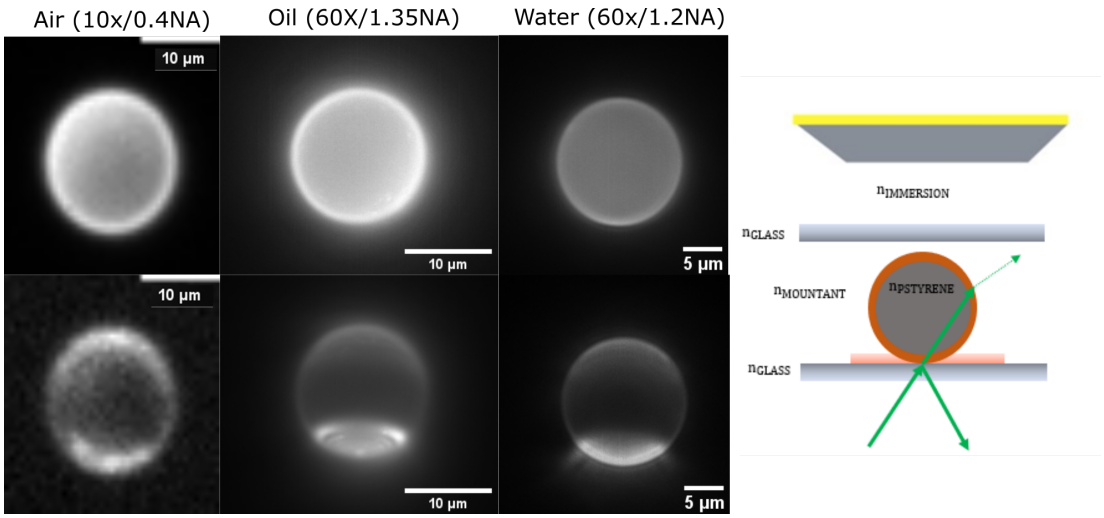

Figure 2.10: Same fluorescent shell beads imaged in air (with a 10x/0.4NA objective), oil (60x/1.35NA) and water (60x/1.2NA in widefield epifluorescence (top line) and in TIRF, lower line, at a 70°incidence angle. Schematic illustrating refraction into bead given refractive indices of situation.

to be an issue, Figure 2.10. Again, the specimen is altering the evanescent field in attempting to measure it and refracting the beam that would otherwise undergo TIR due to its high refractive index, as shown schematically in Figure 2.10.

2.3.2 Evanescent power with varying incidence angle

The good linear fit to logarithmically scaled exponential data observed in Figure 2.11, falling within 97% confidence intervals with a goodness of fit R^2 of 0.986, indicated that the power measured at the sample plane of the system was indeed decaying exponentially. While not a direct measure of evanescent intensity, assuming the area illuminated by the beam does not change, power can be used as a proxy here, and would be theoretically expected to exponentially decrease with increasing incidence angle above the critical angle for TIR. This is not a necessary step for characterising all TIRF systems but was useful here as a control to the depth measurement protocol (and ultimately rejected) presented.

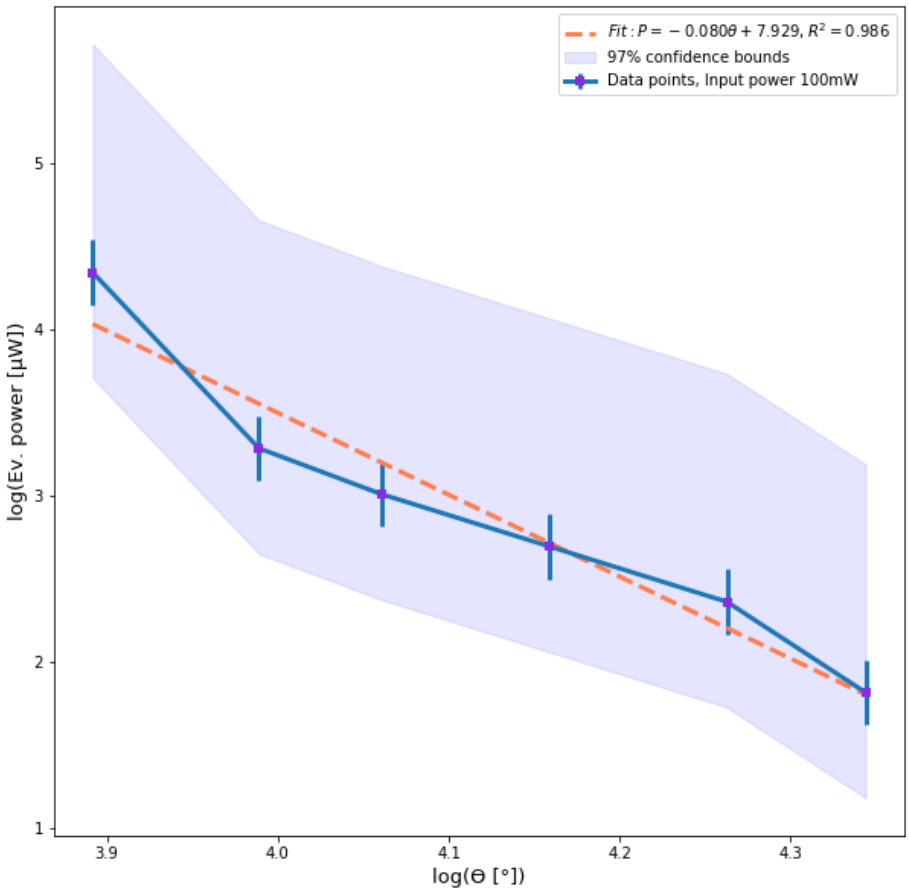

Figure 2.11: Power at sample plane versus incidence angle of beam, logarithmically scaled and fit to a straight line. Error bars from RMS residuals from fitting function, 97% confidence boundaries computed with SciPy Student t-function. Theory for this measurement is shown for the proportional quantity of intensity against incidence angle in Figure 1.10b.

2.3.3 Evanescent power with varying polarisation angle

For each 10° rotation of the half wave plate, an averaged value for power at the sample plane was recorded, and this process was then repeated for increasing incidence angle. The power signal against orientation angle of the half wave plate was sinusoidal (as shown in Figure 2.12), and so the maximum and minimum values of this signal gave a

measure of the evanescent power from the p- and s-polarised components of the incident beam respectively.

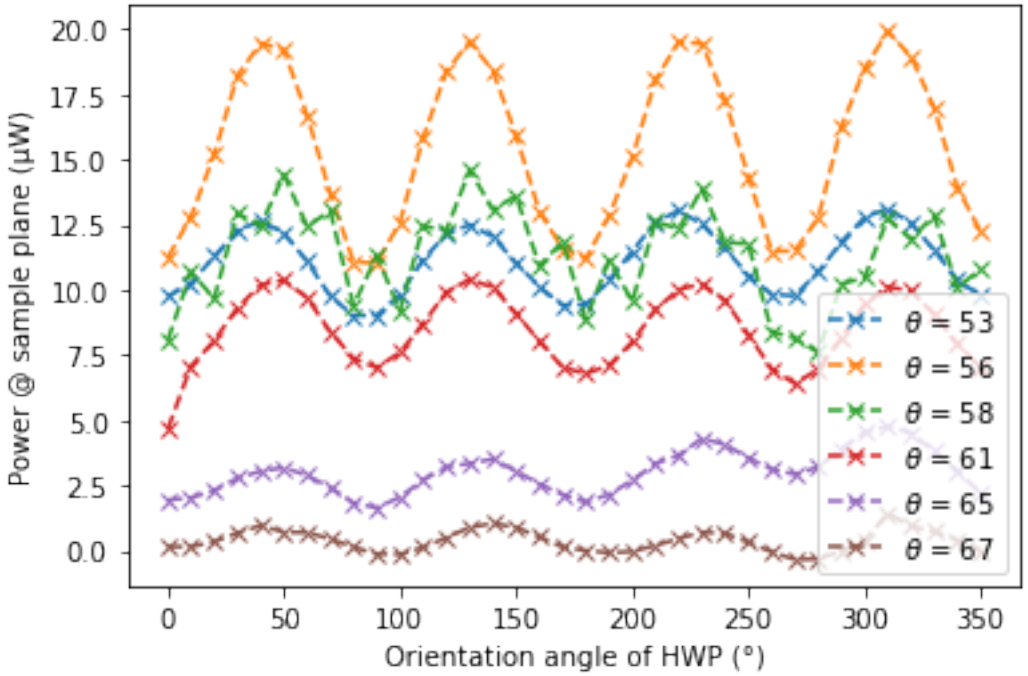

Figure 2.12: Power at sample plane versus orientation angle of half wave plate about optical axis for varying incidence angle.

The difference between these two measurements are shown in column 2 of Table 2.1, with a % deviation found by scaling against the maximum power measured, shown in column 3. Using (1.14), the relative deviation between these components can be calculated theoretically, shown in column 4.

θ_i (°)	Power deviation (μW)	% power deviation	% theoretical deviation	Δ (%)
56	8.89	36.7	41.2	4.5
58	6.99	36.9	40	3.1
61	5.75	39	39.4	0.4
65	3.12	34.3	38.3	4.0
67	1.77	30.7	37.9	7.2

Table 2.1: Measured power deviation between peaks and troughs of power data in Figure 2.12 compared against expected theoretical deviation, (1.14), using experimental θ_i, n and normalising incident polarisation

For the range of incidence angles recorded, measured evanescent power differed less

than 7.2% from expected evanescent intensity. A smaller deviation between s- and p-polarised light was observed for higher incidence angles, following evanescent theory. The shallowest field recorded, corresponding to 67° incidence, represents the largest difference between measurement and theory. The expected evanescent field thickness for a beam incident at 67° to a borosilicate glass to air boundary is $\sim 43\,\mathrm{nm}$. This incredibly thin field is unlikely to be measured accurately with the power meter used in this work, the sensor face of which was inset slightly several hundred microns into the plastic casing, so an error is to be expected. This inset maintains the assumption that the evanescent field is propagating from a 1.51 refractive index of glass into $\tilde{1}$ refractive index in air (rather than the much higher refractive index of the silicon of the sensor head) but decreases the liklihood that the sensor will be within the reach of the evanescent field. This meter and sensor head where the only partially suitable means available to us to characterise this measurement and as such these drawbacks must be considered when evaluating this result. However, 7.2% of a difference is a reasonable agreement and suitable to characterise this result as evanescent.

2.3.4 Demonstration of TIRF prototype for fluorescence microscopy

Despite the issues identified with the proposed depth measurement method, each of the control measurements involving power at the sample plane confirmed the presence of an evanescent field from a beam which was measured to be at a super-critical angle at the top face of the prism. Therefore, attempting some TIRF imaging with the developed set-up was a feasible next step.

Mammalian cell imaging

Using the preparation and labelling protocol described in Chapter 2.2.6, two different coverslips of fixed human breast cancer cells were fluorescently labelled with an Alexa Fluor 555 antibody against the focal adhesion protein paxillin, Figure 2.13, and with a rhodamine conjugated phalloidin stain labelling F-actin in the cells cytoskeleton, Figure 2.14.

For each specimen, the coverslips were sequentially imaged with the 575 nm LED in

widefield and then with the 532 nm beam undergoing TIR. For a 20% LED power set on the CoolLED controller, the power at the top surface of the prism was measured to be 45 mW. For a 50 mW free space 532 nm laser undergoing TIR, the power measured at the top surface of the prism was 1.04 µW. These are clearly not comparable illumination powers however, matching widefield and evanescent powers is a challenge. The nature of evanescence for a super-critical angle which is need for TIRF is an exponentially decaying intensity, whose power over a millimetre squared area will be incredibly difficult to measure accurately with even a µW sensitive power meter. This issue is compounded further if the face of the sensor is more than a few hundred nanometres away from the prism face where the incident beam is undergoing TIR, where the sensor would simply be measuring ambient light levels, with perhaps some scattered laser light. Regardless, fluorescent intensity levels in cell images were endeavoured to be matched in widefield epifluorescence and TIRF modalities.

The reduction in background signal is quite clearly evident in Figure 2.13. These images were obtained with a 10x/0.4NA objective lens, with the cylindrical lens (Figure 2.1) in sharp line focus. The background signal observable in widefield epifluorescence can be accounted for by non-specific binding or cytosolic binding of the Alexa Fluor 555 antibody.

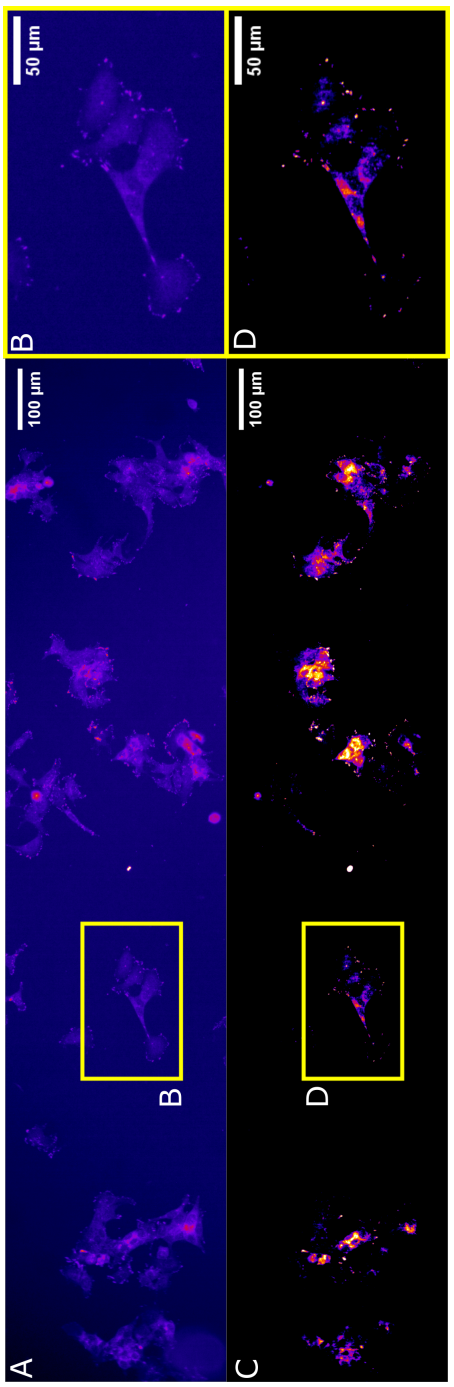

Figure 2.13: (A) MCF-7 cells labelled against paxillin with an Alexa Fluor 555 secondary antibody imaged with widefield epifluorescence with a region of interest highlighted by a yellow box, (B) digitally zoomed ROI of epifluorescence image (A). (C) Same microscope FOV with TIRF illumination focused with a cylindrical lens with a region of interest highlighted by a yellow box, (D) digitally zoomed ROI of TIRF image (C).

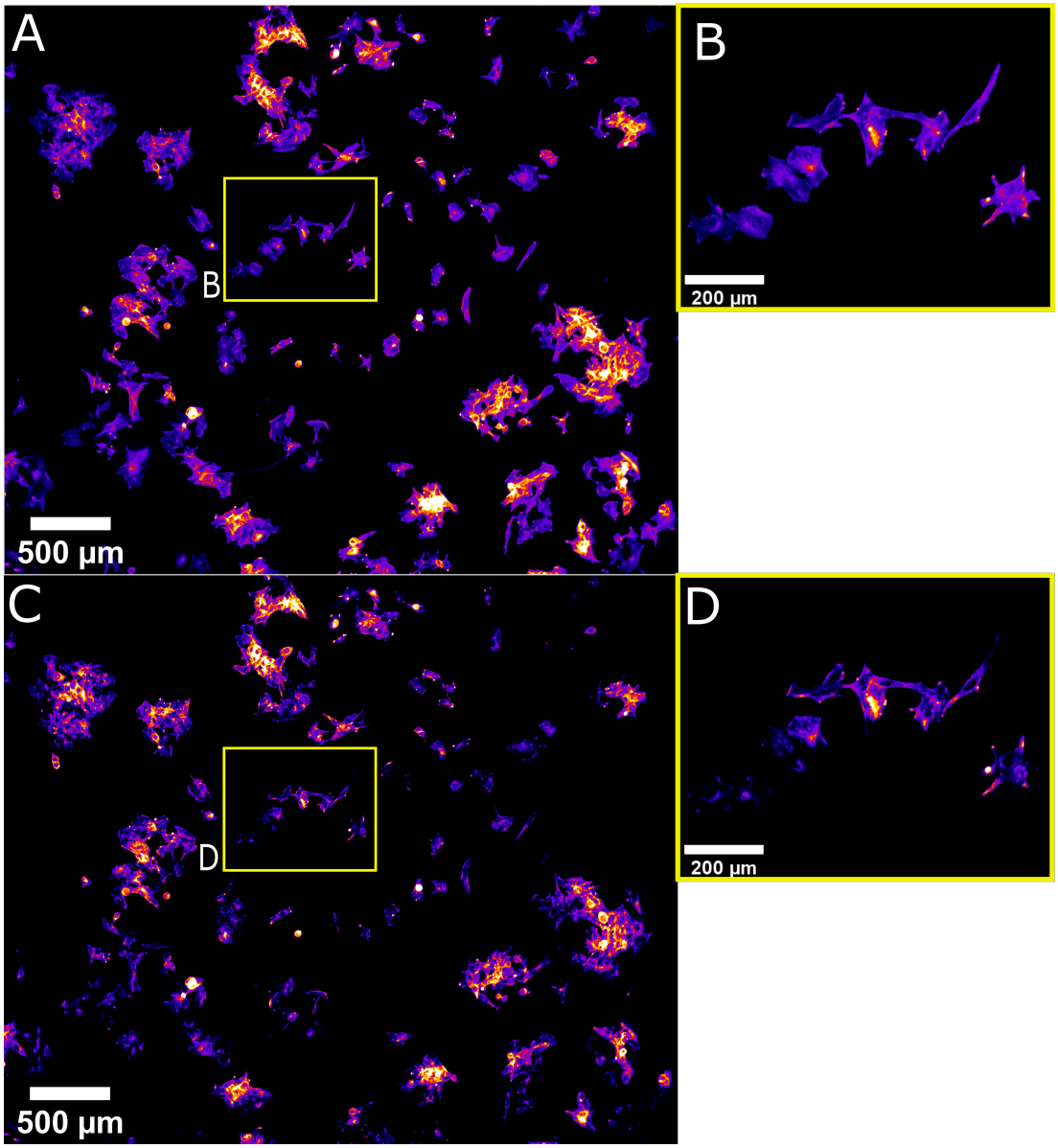

Figure 2.14: (A) MCF-7 cells labelled against F-actin with Rhodamine Phalloidin imaged with 10X/0.4NA objective lens in widefield epifluorescence mode with highlighted ROI indicated by yellow box, (B) digital zoom of ROI in A. (C) Same FOV as A with TIRF illumination with same ROI indicated. (D) Digital zoom of ROI in C.

The displacement between the cylindrical lens and the prism was adapted here to change the area of evanescent illumination at the specimen plane. The gimbal mirror was adjusted to achieve a 66° incidence angle as previously and imaging of the F-actin stained specimen was carried out, Figure 2.14. The abundance of actin filaments in the

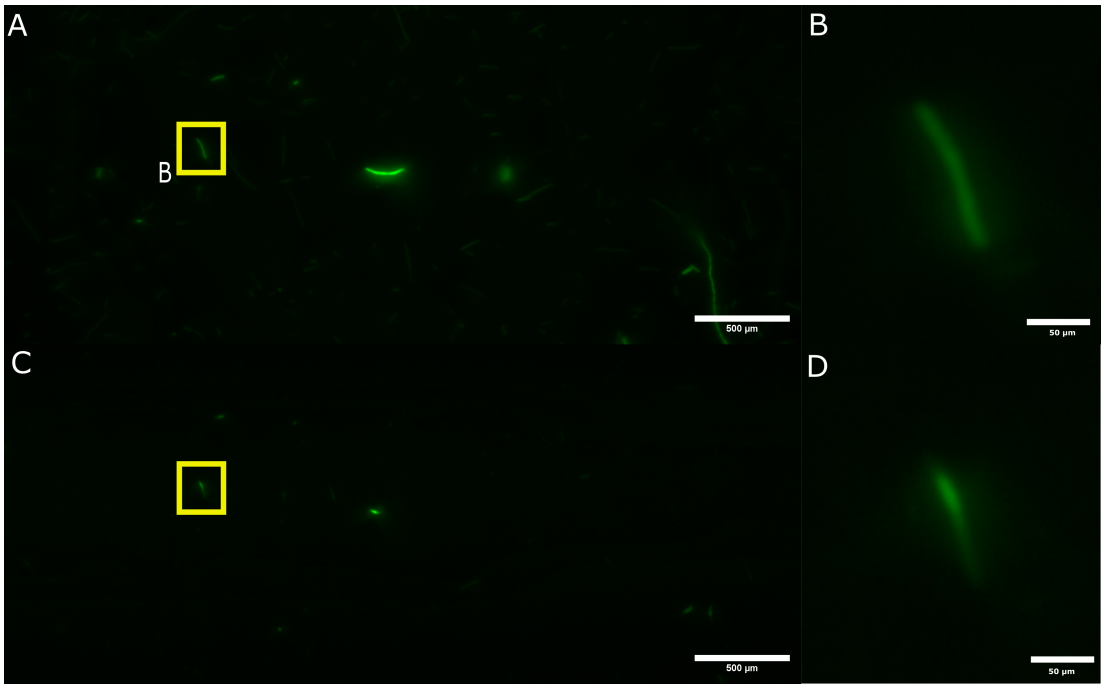

Figure 2.15: *E. coli* expressing mCherry ubiquitously visualised with a green LUT for clarity. (A) imaged in widefield epifluorescence with a yellow bounding box indicating a region of interest. (B) digital zoom of ROI indicated in A. (C) 72.9° incident TIR beam exciting fluorescence across same field as A . (D) digital zoom of ROI indicated in C.

cells compared to the number of focal adhesions in contact with the coverslip in Figure 2.13 imaged with a 10x/0.4NA lens slightly obscures the improvement of imaging with TIRF illumination. However, in Figure 2.14B and D, it is evident that less of the cells are being illuminated and the actin at the peripheral points of the cells in contact with the coverslips are clearer in TIRF (2.14D) than in widefield epifluorescence (2.14B) and that closer to the centre of the cells, fine detail is evident in TIRF that is dwarfed in the widefield epifluorescence image from fluorescent signal deeper in the cell.

Microbiological imaging

As with the mammalian cell imaging, there is a visible difference between widefield epifluorescence illuminated mCherry expressing *E. coli* DH5α cells and sequentially imaging in TIRF: lower background, less cells and less of the cell bodies observable in TIRF, Figure 2.15. However, the mCherry plasmid is ubiquitously expressed every-

where within the cell, lacking the fine detail localised to the membrane which is most well suited to TIRF imaging. Additionally, unlike the mammalian case, these *E. coli* cells are imaged live, introducing a temporal lag between epifluorescence and TIRF images shown in Figure 2.15 which could introduce a spatial drift between illumination channels.

While not explored further at this prototype illuminator stage, microbiological imaging in TIRF was shown to be feasible here and was further studied upon scaling the prototype up for the Mesolens.

2.3.5 Photobleaching decay analysis

While in principle, a reduction in photobleaching rate in a single optical section in TIRF versus widefield illumination where the entire depth of specimen is illuminated simultaneously is somewhat to be expected, there is no literature to this authors knowledge that fully quantifies this. Furthermore, the improved SBR in TIRF allows for a lower illumination power to be used, further minimising the effects of photobleaching.

In an attempt to relate the photobleaching effects of widefield versus TIRF illumination, two identically prepared specimens under the same imaging parameters for either modality and analysis of the photobleaching signal was carried out. As shown in Figure 2.16, the rate of photobleaching of the specimen over a 60 minute imaging window in widefield epifluorescence was linear, with a very good fit to a straight line decay (Figure 2.16(A)). Photobleaching is a nonlinear process and this fit to widefield epifluorescence data is only linear within this short imaging time window. If imaged for longer, this would also show an exponential decay as for the TIRF case and is indicative of a slower rate of bleaching. However, for the equivalent TIRF case, the photobleaching signal follows an exponential decay, fitting very well to a straight line of logarithmically scaled average power measurement (Figure 2.16(B)). While this is not a comparison of rate, where a reasonable assumption would be this would be lower for TIRF, this linear and exponential result agrees with expectation for widefield and evanescent illumination.

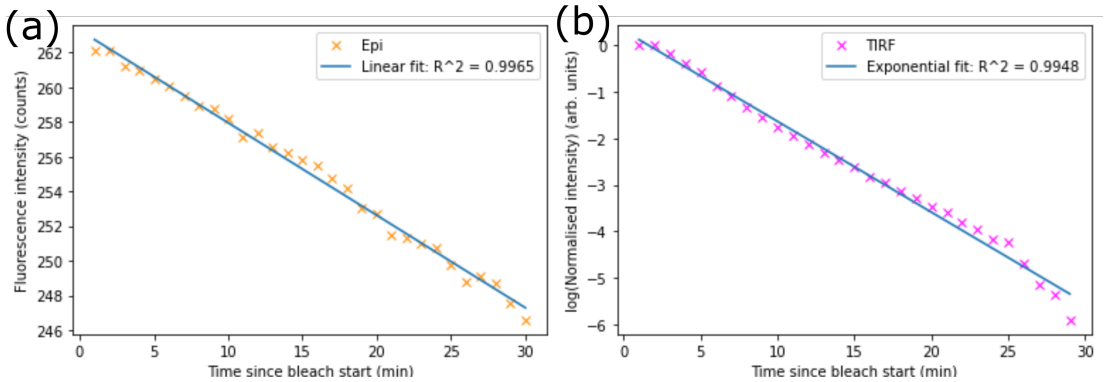

Figure 2.16: Photobleaching decay of intensity signals under (a) widefield epifluorescence and (b) normalised TIRF with a 10x/0.4NA objective, 1s exposure time, comparable optical powers at sample plane, 2 minute intervals over 1 hour of continuous illumination. Note, logarithmic scaling of data in B in order to use a simple linear fit to fit to exponential in Python. The data in (a) is not normalised to show that the intensity does not drop significantly over the 30 min time window as is the case for bleaching in TIRF.

2.4 Discussion

The presented depth measurement technique involves a simple sample preparation by salinizing a borosilicate glass lens specimen in a monolayer of an amine binding dye with a excitation wavelength suitable for the imaging system. This lens specimen can then be placed in direct contact with the TIRF prism, avoiding the preparation step of suspending in a refractive index matched mountant.The error on this method of depth calculation arises from simple quadrature of the error on the radius of curvature (quoted by lens manufacturer) and the standard deviation of FWHM extracted for the radius parameter. In previous methods for measuring evanescent field depth with micron-diameter beads, [46], the error on the depth was estimated purely by the fluorescence signal excited from the beads. Unlike the complex work in another previous method, [92], our presented depth measurement protocol only relies on the imaging objective lens used in TIRF, not requiring an additional technique such as AFM.

The negative outcome of this method was cross validated by examining other characteristics of the evanescent field, power with varying incidence angle and polarisation. However, while the power measurements did confirm the presence of evanescent illumi-

nation, the imaging procedure appeared to damage the lens specimen used to visualise the evanescent field depth, resulting in inconsistent and a lack in reproducible measurements of the same field parameters with the same lens specimen.

While the presented data shows a discrepancy between theoretical expectation and measured depth of evanescent field, the evanescent field depths measured using the lens specimen protocol are below the depth of field of the imaging objective and agree with the theoretical trend that a higher incidence angle will yield a thinner evanescent field. Discrepancy between theory and measurement in this case, where evanescence has been validated through other measurements, is useful in describing the physical system.

Crucially, the depth values measured are significantly lower than the axial diffraction limit of the imaging objective, proving the capability of this illuminator to resolve fine spatial detail axially.

While the protocol for measuring evanescent field power was relatively standard, the data obtained agrees with the conclusion from measurement of field depth that this illuminator is indeed producing an evanescent field, albeit not a scatter free evanescent field. The evanescent power with respect to incidence angle in Figure 2.5 agrees well with the theoretical expectation that evanescent intensity decays exponentially with increasing incidence angle. The similar data of varying this power with the orientation of the linearly polarised incident light presented in Table 2.1 shows the variation between vertically (or s-) polarised light at the minima of the sinusoidal signal and horizontally (or p-) polarised light at the maxima. The combination of measuring field depth and power at the sample plane with two relatively simple experimental protocols and the developed image analysis pipelines presented here would allow for a complete characterisation of an evanescent field produced by a prism based TIRF imaging modality. However, simply focusing on the depth measurement protocol would yield an axial resolution measurement obtained via a much simpler experimental method.

However, the presented depth measurement requires an objective working distance that allows for a 1-2 mm thick lens specimen to be placed in the imaging path, which limits this technique to prism based TIRF modalities.

Chapter 3

MesoTIRF: scaling a prism-TIRF illuminator for axial super-resolution across 4.4 mm x 3.0 mm FOV

3.1 Introduction

In this Chapter, the technique of illuminating a mesoscopic field of view with an evanescent field, shortened to MesoTIRF, will be discussed. This work follows on from the prototype designed, tested and demonstrated in Chapter 2 and a thorough introduction to both TIRF and the Mesolens is provided in Chapter 1.5 and 1.7.1 respectively. A custom TIRF illuminator optical set up, centred around a 45° dove prism, has been developed as an additional illuminator for the existing custom mesoscopic objective, the Mesolens, [71]. The custom giant objective lens combines the large field of view (4.4 mm x 3.0 mm) yielded from a low 4x magnification with a relatively high numerical aperture of 0.47. This allows for mesoscopic sub-cellular imaging with a lateral resolution of 700 nm and a widefield axial resolution of 7 µm. Following from proof of concept measurements and imaging, this Chapter will include biological imaging with the novel MesoTIRF modality and a discussion of the current limitations and some

potential avenues for future work.

3.2 Methods

3.2.1 Optics

The choice of optics of the MesoTIRF modality were informed by those included in the TIRF prototype discussed in Chapter 2, with some adjustments to account for the physical size of the Mesolens objective element. A different excitation laser source was chosen and implemented in order to have finer control over evanescent field power and to allow for multi-wavelength imaging with minimal realignment of the setup.

Optical set-up

A schematic diagram of the optical set-up is shown in Figure 3.1. The illumination laser source was a tunable wavelength (Chameleon Ultra II, Coherent) Titanium Sapphire laser pumping an optical parametric oscillator (OPO) (Compact OPO-Vis, Coherent). The second harmonic generation (SHG) of the signal wavelength output of the OPO was used as the laser source, choosing laser wavelengths of 500 nm and 585 nm for dual-wavelength MesoTIRF imaging. This choice of wavelengths was informed by the specification of the 100 mm diameter Pinkel-type chromatic reflector and barrier filters used for Mesolens imaging which allows excitation/emission combinations of 415 ± 35 nm/465 ± 10 nm, 505 nm ± 25 nm/542.5 ± 7.5 nm, 575.5 ± 22.5 nm/677.5 ± 72.5 nm.

For comparison of the performance of the MesoTIRF illuminator with widefield epifluorescence, two light emitting diodes (central wavelengths 504 nm and 584 nm) were for wide-field illumination (pE-4000, CoolLED).

The optical power of the SHG OPO output wavelengths delivered to the specimen stage of the system were adjusted using a combination of a polarising beam splitter and a variable neutral density filter wheel. The beam was first expanded by a Keplerian beam expander consisting of a 50 mm and a 100 mm focal length achromatic plano-convex lenses. A half-wave plate polariser was used to adjust the polarisation angle of

the beam for polarised TIRF, and a first surface reflecting mirror in a kinematic mount was used to adjust the angle of incidence of the beam to 86° into a 45°dove prism made of borosilicate glass which served as the MesoTIRF prism. The 25 mm thick prism had a top surface of 20 mm by 70 mm, and was placed on top of the computer-controlled specimen stage (ProScan III, Prior Scientific) for accurate positioning of the prism in three dimensions. To capture the large, high-resolution images produced by MesoTIRF, a chip-shifting camera sensor (VNP-29MC, Vieworks), which recorded images by shifting a 29-megapixel CCD chip in a 3 x 3 array, was used. Reconstruction of each image (260 Megapixels, 506Mb) took approximately 5 s on a typical computer workstation [73].

In order to build the MesoTIRF optical setup such that it could reliably be used as a microscope illuminator, each parameter of the system was fully characterised.

Laser power at key positions in the beam path

The output power of the Chameleon OPO in SHG mode varied slightly depending on temperature fluctuations, mechanical disruptions from the optical bench or following periods of non usage. This was likely due to back reflections into the OPO cavity or slight shifting of the mirror elements effecting the amplification process. As such, optical power was measured before each experiment.

Due to the exponentially decaying nature of an evanescent wave and the clearance of around 10 mm between the top surface of the prism and the front element of the Mesolens, a direct measure of evanescent field power was difficult to obtain experimentally. Instead, we took the evanescent field power of our set-up to be a measure of the laser power entering the MesoTIRF prism scaled by the Fresnel reflection losses at each prism face the beam interacts with and with the theoretical drop in intensity for a s-polarised (of laser relative to optical axis) beam reflecting at the measured incidence angle. This value of evanescent power, or power at the specimen plane, is quoted for each MesoTIRF imaging experiment carried out in this thesis.

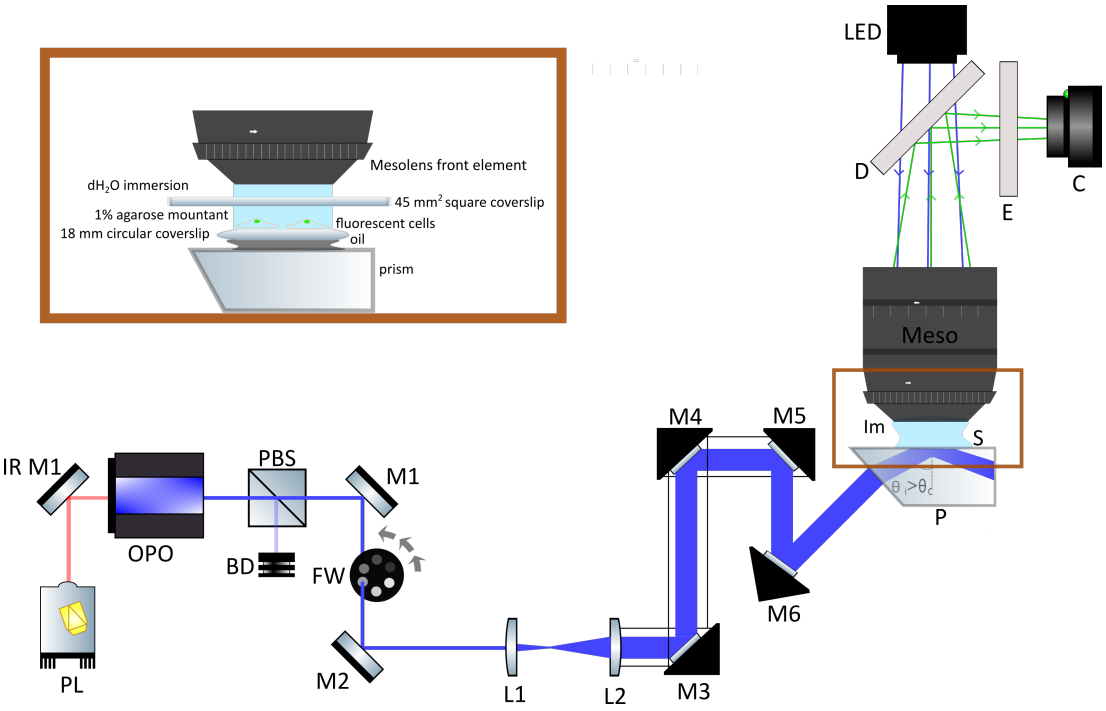

Figure 3.1: Optical schematic of MesoTIRF setup. PL: Titanium Sapphire pump laser (Ultra II, Coherent), IR M1: Infrared mirror (BB1-E03, Thorlabs), OPO: Optical Parametric Oscillator (Chameleon OPO-Vis, Coherent), PBS: polarising beam splitter (CCMS-PBS201/M, Thorlabs), BD: beam dump, M1-6: visible broadband dielectric mirrors (Thorlabs, BB1-E01), FW: filter wheel with 5 neutral density filters (Thorlabs, FW1A), L1: 50 mm planoconvex lens (LA1131-A-ML, Thorlabs), L2: 100 mm planoconvex lens (LA1509-A-ML, Thorlabs), M3-6 mounted in right angled cage mounts (KCB1C/M, Thorlabs), P:45° borosilicate glass prism (Mesolens Ltd.), S: sample, Im: immersion fluid (distilled water), Meso: Mesolens objective element [71], D: dichroic filter & E: emission filter(custom from Chroma), C: chip-shifting camera sensor (VNP-29MC; Vieworks), LED: 504 nm and 584 nm LEDs from LED module (pE-4000, CoolLED). Inset: illustration of specimen mounting procedure for MesoTIRF imaging.

Illumination source emission spectra

As the choice of MesoTIRF illumination wavelengths were chosen to match the specifications of the custom large diameter dichroic and emission filters in place in the Mesolens, the emission (i.e. directly from the LED, not fluorescent emission in this case) spectra of the existing CoolLED pE-4000 LED diode engine at the specimen plane of the Mesolens was measured to ensure no spectral bleedthrough would occur and to directly match the peak wavelength of the LED to the chosen laser wavelength. The true peak wavelength of the measured LED spectra was then used to inform the wavelength chosen on the tunable wavelength Ti:Sapphire pumped OPO in SHG mode.

To obtain a 585 nm output beam from the laser source, the use of the second harmonic generation (SHG) function of the OPO cavity. The OPO unit had 4 beam exits: one for direct Ti:Sapphire pump laser (tunable from 680 nm to 1080 nm) which simply passed through the OPO with no modification, one which performed SHG of the Ti:Sapphire input (340 nm to 540 nm wavelength range), one which emitted output light from the OPO crystal (1000 nm to 1600 nm) and one which performed SHG on the OPO signal (500 nm to 800 nm).

In order to simplify the realignment of the following optical setup when utilising the multi-wavelength imaging capability of the MesoTIRF illuminator, it would be beneficial for the beam path through the OPO unit to remain constant between changing wavelengths. As such, the peak wavelengths of the existing LED illuminators was compared against the peak wavelengths of corresponding wavelengths directly from the Ti:Sapphire SHG and the OPO SHG.

Beam width & uniformity

While the output beam of the OPO SHG was very high quality ($M^2 < 1.1$) with low divergence, the TEM00 mode used was not totally symmetric. As any defects were too small to correct with spatial filters in the beam path (this simply introduced more diffraction effects into the beam), the beam was directed to a Keplerian 2x beam expander consisting of two plano-convex spherical lenses. The $\simeq$ 4.5 mm diameter beam was then examined using a fluorescent test target at the specimen plane of the

MesoTIRF illuminator.

A measure of uniformity of each method of illuminating specimens imaged in this Chapter was performed using two plastic slides which strongly autofluoresce at 500 nm and 585 nm (Chroma, 92001). The slides were sequentially oiled to the top surface of the prism, topped with a wide column of distilled water and small defects in the slides were used to aid focus. Iterative imaging was then performed with widefield epifluorescence and MesoTIRF illumination, of each wavelength.

Determination of TIR incidence angle

A schematic diagram demonstrating how the TIR angle was measured is shown in Figure 3.2. Due to the lack of clearance between the prism and the front element of the Mesolens, the incidence angle at the top surface of the prism was determined using the 45° angled entrance face of the prism, as opposed to the planar exit face used in the previous Chapter. The height of the beam from the Mesolens stage as it entered the 45° prism face was measured using a millimetre ruler, as was the distance between this point and the point where the beam was level with the front of the Mesolens stage. This measured height and distance yielded values for the adjacent and opposite sides of a right angled triangle where the laser beam formed the hypotenuse.

3.2.2 Imaging

Prior to imaging, alignment of both the 500 nm and 585 nm excitation wavelengths was verified using a fluorescent test target (Thorlabs, ADF5) oiled to the top surface of the prism using immersion oil (Type LDF, Cargille) and a large column of distilled water was used as immersion fluid between the target and the Mesolens. The chip-shifting camera imaged the resultant fluorescence from the test target to ensure that the TIRF beam filled the FOV of the Mesolens and matched the area imaged in widefield epifluorescence mode with LED illumination.

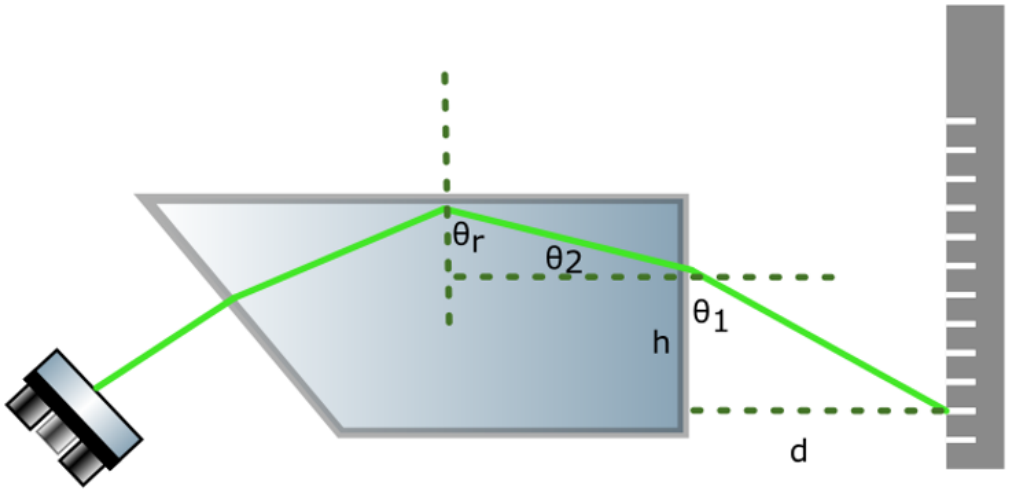

Figure 3.2: Geometric measure of incidence angle using height of reflection beam at a set point in the far field.

Proof of concept imaging

To confirm that the optical set up illustrated in Figure 3.1 was generating an evanescent field as expected, we labelled fixed a sample of murine fibroblast cell line (3T3-L1) stained with both a fluorescent nuclear marker (SYTO Green) and fluorescent antibody labelling of paxillin, and we performed a comparison of image signal-to-noise ratio in both widefield epifluorescence and MesoTIRF imaging. The detailed cell preparation protocol is given later in this Chapter, 3.2.4. We hypothesised that with MesoTIRF the cell nucleus would be too far from the basal membrane to be excited by the evanescent wave, but that the fluorescent emission from the nuclear marker would be visible with widefield epifluorescence illumination. The fluorescently labelled focal adhesions in the basal membrane served a dual purpose. They were used both to find focus of the basal membrane for cell imaging, and the fluorescence images were used to compare the image quality, namely background signal and signal-to-noise, using MesoTIRF and widefield epifluorescence imaging. For this imaging experiment, an exposure time of 2s and a camera gain of 1X was used to for acquisition of the widefield epifluorescence and TIRF illuminations of both SYTO Green and AlexaFluorPlus 594 tags. Due to the nature of

evanescence, it was not possible to match the power supplied by the TIRF illuminator with that of the LEDs in widefield epifluorescence, 3.48 mW of evanescent illumination was produced by each laser wavelengths at the specimen plane (calculated by the freely propagating laser power by the Fresnel losses it would incur at the prism interfaces and then by the evanescent losses at the TIR plane). In widefield epifluorescence, 25 mW of the 504 nm LED was used to excite the nuclear tag and 22 mW of the 584 nm LED for the paxillin tag.

Resolving fine structure

In order to quantify the ability of the MesoTIRF illuminator to resolve fine spatial structure, another fluorescent test sample of 3T3-L1 cells were fixed and prepared with an AlexaFluorPlus 594 tag conjugated to the focal adhesion protein paxillin. Focal adhesions served as a useful organelle of interest to quantify the ability of the MesoTIRF illuminator to pick out fine detail in the dramatically low background, comparing against the standard of widefield epifluorescence. As in conventional TIRF, we expected a reduced fluorescent background with the MesoTIRF, improved signal-to-noise ratio and less out-of-focus fluorescence when imaging fluorescently-labelled focal adhesions with MesoTIRF when compared to widefield epifluorescence.

The improved image contrast of MesoTIRF over widefield epifluorescence with the Mesolens allows for identification and classification of structure over cell membrane proteins across the full 4.4 mm x 3.0 mm FOV. Fixed 3T3-L1 cells labelled for paxillin with AlexaFluor 488 were mounted in 1% agarose and imaged first with widefield epifluorescence and then MesoTIRF (full specimen preparation detailed i Chapter 3.2.4. Subsequently, 5 line profiles were drawn through neighbouring focal adhesions (in FIJI) in both widefield epifluorescence and TIRF and the intensity along each pixel in these profiles were saved as .xlsx files. The saved data was loaded into a Python DataFrame using Pandas. A measure of contrast from each widefield epifluorescence and MesoTIRF image was estimated here as the peak fluorescence intensity over the mean of the intensity signal. Improvement in MesoTIRF contrast versus widefield epifluorescence was taken as the ratio between these two values.

The widefield epifluorescence and MesoTIRF intensity signals were then normalised with respect to their own maximum intensity and compared in a single plot. This allowed for a clear comparison of the drop in background signal in MesoTIRF with respect to widefield epifluorescence.

Finally, to quantify the number of focal adhesion features distinguishable from background in each image, the noise floor from each signal was subtracted such that the baseline intensity would match in widefield epifluorescence and MesoTIRF and then a confidence boundary of minimum intensity peak value would be considered as a focal adhesion. In all data presented here, a forgiving boundary of 0.5 (half of the peak normalised intensity) was taken as the lower limit for a focal adhesion detection. The areas of each signal that agreed with this condition were visualised on separated plots as indigo regions, where a continuous indigo line represents one resolved focal adhesion (Python code in Appendix A.0.4).

Uniformity of evanescent field

The uniformity of the MesoTIRF illumination field at the sample plane was demonstrated biologically using a dual labelled fixed specimen of the human breast cancer line HeLa. The specimen was antibody labelled against the focal adhesion protein paxillin with AlexaFluorPlus 594 and the cytoskeletal protein F-actin with fluorescein phalloidin. Due to the high brightness of the fluorescein tag, we adjusted the illumination powers of the 500 nm OPO SHG laser appropriately to get similar fluorescent signals from both proteins; 2.00 mW of the 500 nm laser and 3.28 mW of the 585 nm remained for MesoTIRF excitation following attenuation through the prism and TIR. For each image, an exposure of 2 s and a camera gain of 30 X was used.

Widefield epifluorescence following MesoTIRF bleach

The optical sectioning ability of TIRF is claimed to minimise photobleaching throughout literature, as discussed in detail in the Introduction to this Chapter and in Chapter 1.5. The extent of photobleaching is confined to the thin evanescent field depth, while the bulk of the labelled specimen is unaffected. As a means to potentially further

characterise this MesoTIRF modality, confluent HeLa cells were plated on coverslips, fixed and antibody labelled against the paxillin component of their plasma membranes with an AlexaFluor488 secondary antibody. Sequentially to this, to test the other MesoTIRF illumination wavelength, confluent MeT-5A cells were also prepared and antibody labelled against the α-tubulin component of their plasma membrane with an AlexaFluor594 secondary. Each of these coverslips were mounted in 1% agarose on a 45 mm width square coverslip. Detailed specimen preparation is included in Chapter 3.2.4. These specimens were then inverted and oiled to the top surface of the prism, such that the cultured coverslip was in optical contact with the prism surface. In each instance, the specimens were constantly irradiated with the maximum output power of the illumination laser (170 mW for 500 nm OPO SHG and 200 mW for 585 nm OPO SHG) continuously for 1 hour with a full 3 x 3 pixel-shifted Mesolens image acquired every 2 minutes. For the HeLa specimen, an exposure time of 2 s and a camera gain of 30X were used, while for the MeT-5A sample, an exposure time of 1 s and a camera gain of 10X. Prior to and following these MesoTIRF 1 hour long bleach steps, each sample was imaged in widefield epifluorescence with the maximum LED powers of the relevant wavelength and the same acquisition parameters as used in MesoTIRF, as shown schematically in Figure 3.3. This was done in order to relate the effect of the bleaching in the MesoTIRF optical section relative to the fluorescence through the full depth of the specimen.

The rate of photobleaching in TIRF was examined in Chapter 2. Here, however, we wanted to examine how the fluorescence intensity compared in widefield epifluorescence post-bleaching in the optical section of the MesoTIRF modality.

Biological imaging with MesoTIRF illuminator

The dual-colour imaging capability of the MesoTIRF modality was also examined with the nuclear and paxillin tagged specimen used to determine the illumination quality of the developed illuminator. To illustrate the dual-colour imaging capability for cell imaging, we prepared a fixed specimen of the human mesothelial cell line MeT-5A with the two membrane proteins of paxillin and tubulin labelled with AlexaFluor488 and

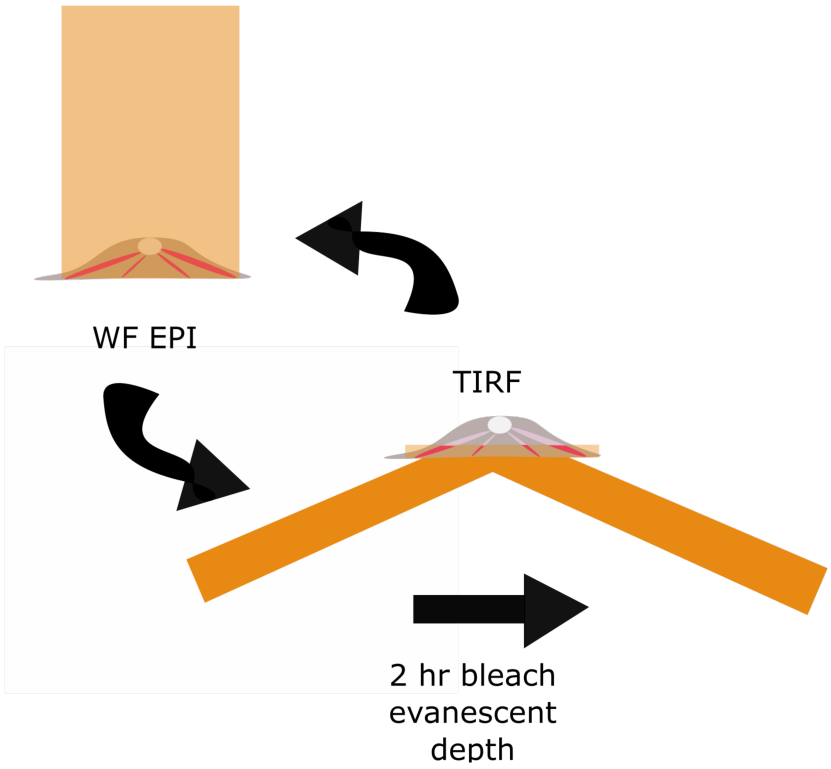

Figure 3.3: Schematic illustration of comparing bleaching rate in widefield epifluorescence and MesoTIRF. Firstly, sample is imaged in widefield epifluorescence (WF EPI), then under 2 hours of constant MesoTIRF irradiation to bleach just the TIRF depth, and then re-imaged in widefield epifluorescence.

AlexaFluorPlus594 respectively. The specimen was sequentially imaged under 3.48 mW of 500 nm and 585 nm laser lines, with a 2s exposure and a 40X camera gain.

3.2.3 Analysis

Signal to background ratio measurement

For the images obtained of F-actin and tubulin structures, a method that took into account the dark unlabelled space between the organelles while identifying the punctate or spindled proteins was required, rather than a simple threshold. To this end, Trainable Weka [93] was trained in ImageJ to identify and segment each of these proteins from both widefield epifluorescence and TIRF images. A selection mask was extracted from

this segmentation, copied over to the original raw image and the mean cell signal was measured in ImageJ. The background signal was calculated from each individual analysed image by selecting three regions of interest of background, calculating the mean intensity, and averaging these measurements.

Resolvable detail comparison between MesoTIRF and widefield epifluorescence

In order to further qualify the image quality of the developed TIRF modality and quantify its ability compared to widefield epifluorescence to identify resolved focal adhesions. To this end, 5 line profiles were drawn through neighbouring focal adhesions (in ImageJ) in both widefield epifluorescence and TIRF and the intensity along each pixel in these profiles were saved to .xlsx files. The saved data was loaded into a Python DataFrame using Pandas. A measure of contrast from each widefield epifluorescence and TIRF image was estimated here as the variation along each line profile over the mean of the intensity signal, [31]. Improvement in TIRF contrast versus widefield epifluorescence was taken as a ratio between these two values.

The widefield epifluorescence and TIRF intensity signals were then normalised with respect to their own maximum intensity and compared in a single plot. This allowed a comparison of the drop in noise floor in MesoTIRF with respect to widefield epifluorescence.

Finally, to quantify the number of focal adhesion features resolvable in each image, the noise floor from each signal was subtracted, by taking an average measure of intensity counts in the background areas and manually subtracting it from each of the images in question in FIJI [89] such that the base line intensity would match in widefield epifluorescence and MesoTIRF and then a confidence boundary of minimum intensity peak value would be considered as a focal adhesion. In all data presented here, a forgiving boundary of 0.5 (half of the peak intensity) was taken as the lower limit for a focal adhesion detection. The areas of each signal that agreed with this condition were visualised on separated plots as indigo regions, where a continuous indigo line represents one resolved focal adhesion.

3.2.4 Biological specimen preparation

Culture of immortalised mammalian cell lines

The cell lines 3T3-L1, HeLa, HEK293 and Met5A were maintained in culture, at 37° 5% CO2 in their recommendated media (see Appendix B).

Antibody labelling of fixed membrane proteins

Coverslips were coated in a 1:500 dilution of fibronectin in PBS prior to seeding with highly confluent cells and grown in culture conditions for 24 hours (or until visible protrusions from the cell membrane to the coverslip where visible). The adherent cells were washed twice with PBS and fixed in freshly diluted 4% formaldehyde. An immunofluorescence (IF) buffer solution (PBS, 2.5% FBS and 0.3% TritonX) was applied to the fixed cells to both block non-specific binding and permeabilise the cell membranes, for 30 minutes at 37°. After removing this buffer, this was replaced by a 1:250 dilution of the desired primary antibody (paxillin: Recombinant Anti-Paxillin antibody [Y113], AbCam, ab32084) or Paxillin Mouse anti-Human, Mouse, Rat, Clone: 5H11, Invitrogen), (tubulin: Anti-α-Tubulin antibody, Mouse monoclonal, Merck T6199) in the IF buffer. These coverslips where kept in a stable humidity culture dish, to prevent evaporation, for 24 hours at 4°. The following day, the primary antibody labelled cells where washed three times with PBS before a 1:200 dilution of the appropriate secondary antibody in IF buffer was applied [(AlexaFluor488 donkey anti-rabbit secondary, Invitrogen), (AlexaFluor488 donkey anti-mouse secondary, Abcam ab150062), or (AlexaFluor594Plus goat anti-mouse secondary, Invitrogen A32742)]. The coverslips where kept in light tight conditions at room temperature for 1 hour. Following a final three step PBS washes, the antibody labelled samples could be mounted in 1% agarose with a 45 x 45 mm coverslip, to allow both for evanescent illumination through the plated coverslip and imaging through the larger one. To aid with cleaner imaging, these samples were allowed to dry fully at 4° in the dark. If specimens were dual labelled, the primary antibody step for each target protein were carried out simultaneously while the fluorescent secondaries were applied sequentially, separated by PBS

wash steps.

Nuclear staining of fixed mammalian cell specimens

The nuclei of fixed cell lines were labelled with a 1:150 dilution of Syto16 Green (SYTO 16 Green Fluorescent Nucleic Acid Stain, Invitrogen S7578) in IF buffer for 20 minutes at room temperature. This was followed by the usual three PBS washes before mounting in 1% agarose.

F-actin staining of fixed mammalian cell specimens

For fluorescent labelling of F-actin, fluorescein phalloidin (ThermoFisher, F432) was diluted 1:100 in IF buffer and fixed, buffered and permeablised cells were incubated in this solution at room temperature for 1 hour, protected from light. Following this time, the cells were removed from the staining solution, washed twice with PBS and mounted in 1% agarose.

3.3 Results

3.3.1 Optical characterisation

Using the height which the beam passed through the 45° face of the prism, the known height of the prism itself and the measured angle of incidence, one could approximate the amount of BK-7 glass the incident laser beam propagated through to calculate the attenuation of the prism. With the centre of the beam measured to enter the 45° face at a height 18 mm (total prism height = 25 mm) to be incident at the top surface at 86°, the beam had to propagate through 4.88 mm of BK-7. Further loss of the benchtop laser power can be attributed to Fresnel reflection factors from both of the prism faces the laser interacts with before reaching the specimen plane. The final attenuation factor arises from the nature of evanescent field generation.

Illumination source emission spectra

Spectrophotometer data yielded a peak LED wavelength of 584 nm with a bandwidth of 27 nm. Therefore, we could reliably set the tunable wavelength of the SHG signal of the OPO to 585 nm when using fluorophores excited in this region. As such, this allowed for a fair comparison between imaging in the 585 nm channel in MesoTIRF and widefield epifluorescence.

However, the peak wavelength for the labelled 490 nm CoolLED measured a 504 nm peak wavelength with a 19 nm bandwidth. For future imaging, only the OPO SHG will be used for MesoTIRF imaging, not requiring the LED comparison, and the discussion of bandwidth would be moot. However, for characterisation purposes, as the OPO and the LED bank demonstrated some drift from their quoted peak wavelengths, it was necessary to confirm that the set wavelengths for each modality agreed with each other. Therefore, the OPO SHG set at 500 nm (measured output of 508 nm) yielded illumination more similar to the LED than the Ti:Sapphire direct output of 490 nm (measured 495 nm). As such, to ease realignment between switching from 500 nm to 585 nm excitation and to maintain comparable illumination wavelengths, only the OPO SHG output of the laser was used in all imaging performed in this Chapter.

Beam width & uniformity

The beam images obtained are displayed in panels A, B, D and E of Figure 3.4. These are raw images without any processing beyond the LUTs used for the purposes of presentation. A line profile (width = 1000 pixels) was drawn in ImageJ from the top left hand corner to the bottom right corner of each of these images for the purposes of examining the fluorescent intensity profile of the illumination. The raw intensity values were normalised and the profiles for each illumination were compared for the same excitation wavelength (500 nm - Figure 3.4C, 585 nm - Figure 3.4C). It is of note that, firstly, MesoTIRF illumination at 500 nm suffers from slight banding in the laser beam incident at the top surface of the leading to an approximately 20% dip in fluorescent intensity in the right hand side of the field. Secondly, for the 585 nm illumination case, a flatter field was measured with the MesoTIRF illumination than that illuminated

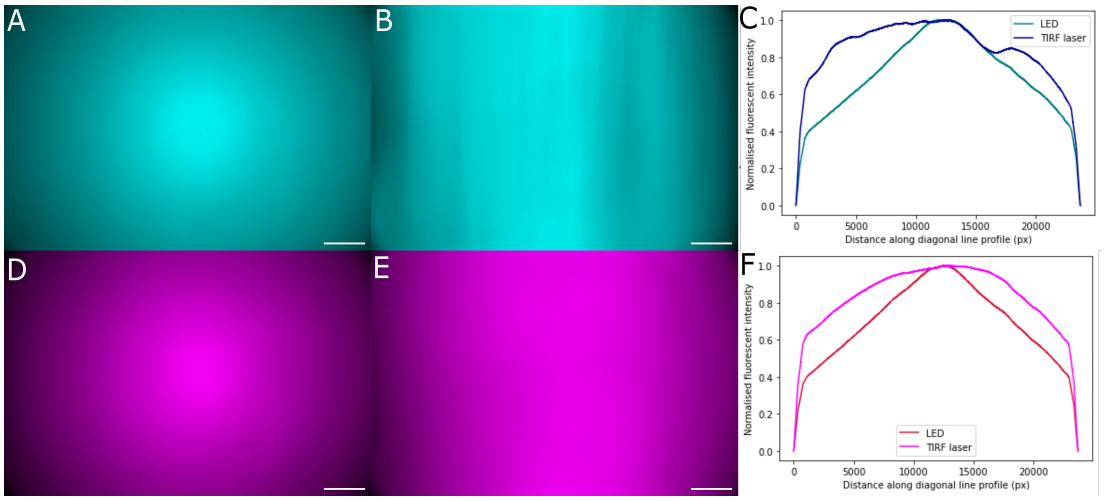

Figure 3.4: Yellow Chroma block under (A) 490 nm LED illumination and (B) 500 nm OPO SHG MesoTIRF illumination (B), with (C) a fluorescence intensity profile of each image (A and B) measured in cross section across the central region of the 3.0 mm dimension. Pink Chroma block imaged with (D) 585 nm LED illumination and (E) 585 nm OPO SHG MesoTIRF illumination, with (F) a fluorescence intensity profile of each image (D and E) measured in cross section across the central region of the 3.0 mm dimension. Scale bars for A, B, D and E are 500 µm.

with the LED.

3.3.2 Imaging

Proof of concept imaging

Figure 3.5 shows a comparison of widefield epifluorescence and MesoTIRF images of dual-labelled fixed 3T3-L1 cells prepared with nuclei displayed in green and paxillin protein displayed in magenta. The full FOV widefield epifluorescence image is shown in 3.5A, with a digitally zoomed region of interest (ROI) indicated by a yellow box in 3.5B. Figure 3.5C shows the same area of the specimen imaged using dual-wavelength MesoTIRF, with the same ROI expanded in 3.5D. Each colour channel was imaged sequentially and collated in FIJI [89].

In widefield, the cell nuclei are clearly visible in 3.5B. These nuclei do not fluoresce when imaged with MesoTIRF as shown in 3.5D, thus confirming that the evanescent wave in MesoTIRF is restricted to a shallow depth close to the coverslip and does not penetrate sufficiently deep into the sample to reach the nuclei. As stated in Meth-

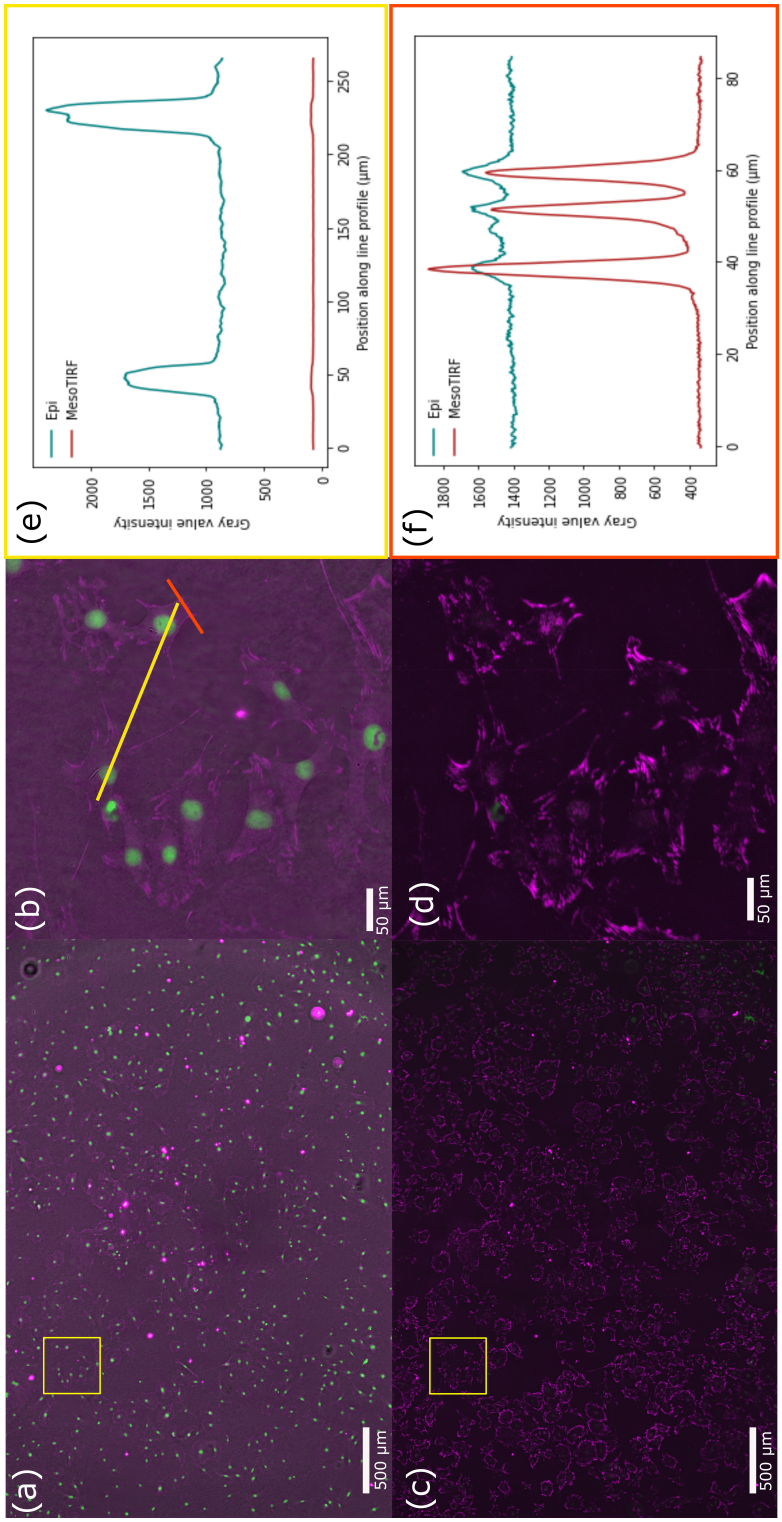

Figure 3.5: Comparison imaging of WF epi and MesoTIRF: fixed 3T3-L1 cells labelled with SYTOGreen stain visualising nuclei (shown in green) and with an anti-paxillin antibody conjugated to Alexa Fluor Plus 594 (shown in magenta). (a) WF epi image with 504 and 584 nm LEDs, (b) ROI digital zoom of (a) with line ROIs in yellow and orange to study nuclei and paxillin, respectively, (c) MesoTIRF image obtained with 500 and 585 nm OPO SHG illumination, (d) ROI digital zoom of (c), (e) yellow line profile intensity plot of neighbouring nuclei in WF epi (teal) and MesoTIRF (dark red), and (f) orange line profile intensity for three neighbouring focal adhesions in WF epi (teal) and MesoTIRF (dark red). Fluorescently labelled nuclei are visible in WF epi data but disappear when imaged with MesoTIRF. A considerable reduction image background signal is also observed in the MesoTIRF images.

ods for this Chapter (3.2.2), the maximum available laser powers for each MesoTIRF channel were directed to the prism, which yielded 3.48 mW of evanescent field power Non-specific binding or binding of the anti-paxillin antibody to cytosolic protein is apparent when imaged with widefield epifluorescence, but this fluorescence signal also disappears when using MesoTIRF illumination. This is further evidenced by the intensity profiles through two neighbouring nuclei (Figure 3.5E) and through 3 neighbouring focal adhesions (Figure 3.5F) for both the widefield epifluorescence image (dark blue) and MesoTIRF (cyan). The difference in background is clearly evident, with MesoTIRF yielding a 4.2-fold reduction in background through the neighbouring focal adhesions over widefield epifluorescence, with a less noisy baseline than that of the widefield epifluorescence image. While the focal adhesions are still visible in widefield epifluorescence, the contrast enhancement afforded by MesoTIRF allows for the elongated features to be easily distinguished from background. SBR improvements of 4.84-fold, 3.9-fold and 3.87-fold were observed in focal adhesions 1, 2 and 3 (measured from peaks in Figure 3.5F left to right) respectively when switching from imaging with widefield epifluorescence to MesoTIRF (see Appendix A.0.4 for analysis script. Furthermore, there is negligible nuclear signal in the MesoTIRF image (Figure 3.5E) because, as discussed previously, the 86° incident beam (resulting in a calculated evanescent field depth of 56 nm) does not penetrate the cell specimen deep enough to excite the nuclear stain. Using the Imaris based 'Surfaces' feature in the nuclear channel, 743 cells were counted

in this single image. For the purposes of presentation, each image presented in Figure 3.5 underwent the 'Contrast Limited Adaptive Histogram Equalization (CLAHE)' local contrast adjustment function in ImageJ. [89]. However, all analysis has been performed on raw image data.

Resolving fine structure

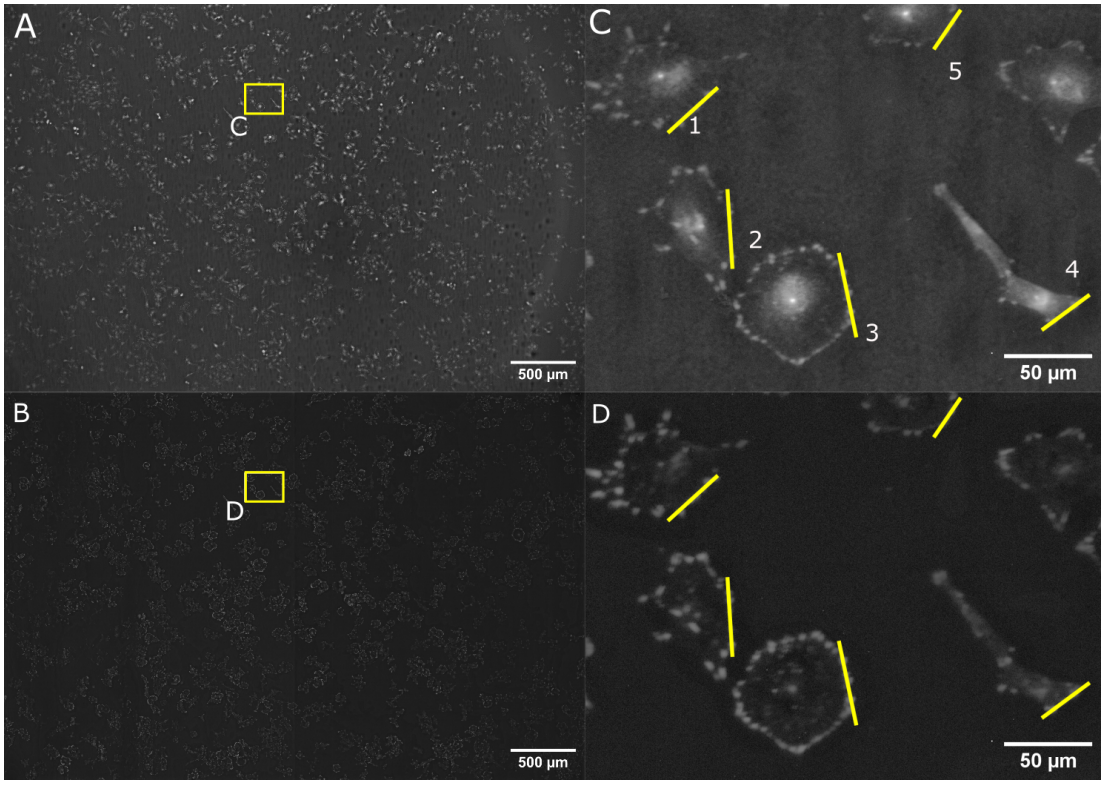

Figure 3.6: Fixed 3T3 cells labelled for the focal adhesion protein paxillin with AlexaFluor488 and mounted in 1% agarose. A: full Mesolens 4.4 mm x 3.0 mm FOV in WF epi, B: full Mesolens 4.4 mm x 3.0 mm FOV in MesoTIRF, C: WF epi zoom with 5 chosen line profiles through neighbouring focal adhesions on 5 cells, D: MesoTIRF zoom with same 5 line profiles.

Boxes in Figure 3.6A and 3.6B indicate ROIs that are digitally zoomed and presented as 3.6C and 3.6D respectively. Line ROIs (n=5) were chosen (1 - 5 read anticlockwise around each ROI), as indicated by numbered yellow lines in 3.6C and 3.6D, and fluorescence intensity profiles of each line were obtained using ImageJ. The fluorescence signal intensity plots for the numbered lines are shown in Figure 3.7, with WF epi

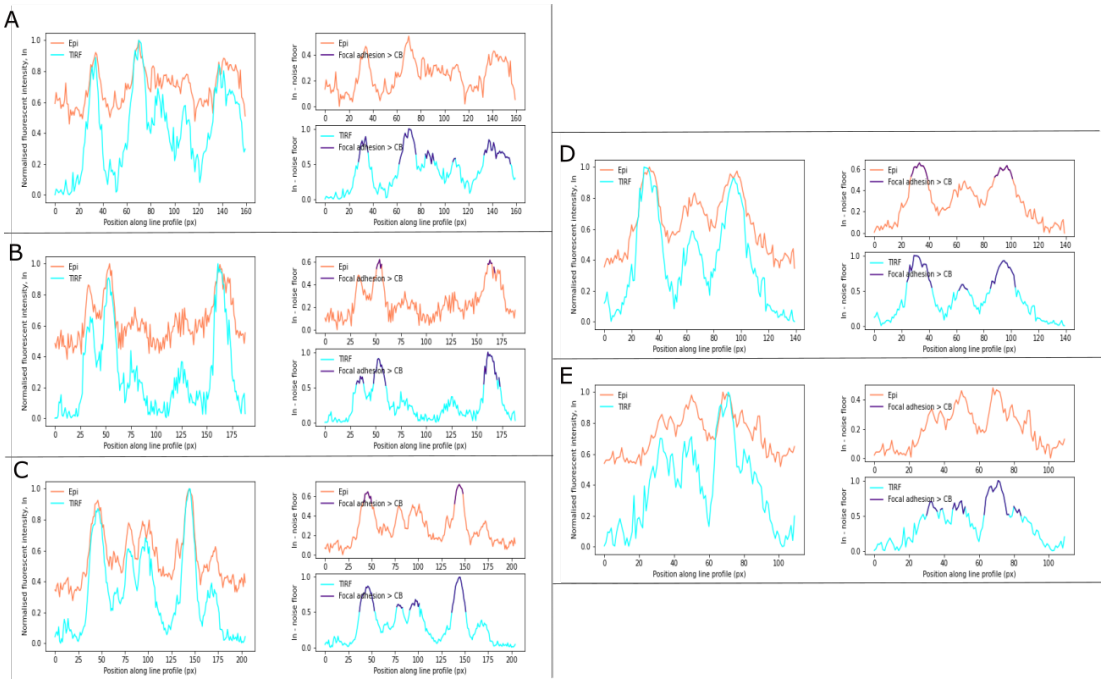

Figure 3.7: A corresponds to line profile 1 in Figure 3.6, B to line profile 2, etc. Left plot in each panel: normalised fluorescent intensity along line profiles, right: individual WF epi (coral) and MesoTIRF (cyan) normalised fluorescent intensity along line profiles to pick out focal adhesions (indigo).

intensities in orange and MesoTIRF fluorescence intensities in cyan. A improvement in contrast of 1.85x was measured for MesoTIRF versus WF epi.

The position and intensity of the identified focal adhesions with a confidence boundary of 0.5 are overlaid in indigo on the line intensities in 3.7, firstly with widefield epifluorescence and MesoTIRF overlaid on each other, and secondly considered individually. In the case of Figure 3.7A, an additional focal adhesion is resolvable in MesoTIRF given the improved contrast afforded by MesoTIRF. The single optical section of MesoTIRF allows for the rejection of signal in WF epi that could be misidentified as focal adhesions. No corresponding peaks are observable in the MesoTIRF image 3.7B so it can be concluded that the membrane is not in contact with the coverslip here. In the next two 3.7C and D, the same number of focal adhesions are resolvable in both imaging modalities. Finally, in ROI 3.7E, a lateral offset is observed for the same focal adhesion in each imaging modality. As this specimen was fixed and stage drift was not observed across the full FOV, a reasonable conclusion is that the paxillin component of the focal adhesion deeper in the cell, imaging with WF epi, is slightly tilted with respect to the component in direct contact with the coverslip, imaged with MesoTIRF.

Uniformity of evanescent field

To examine the uniformity of the MesoTIRF illumination for a biological specimen, a dual labelled specimen was prepared, illuminated and imaged, resulting in Figure 3.8. While the illumination uniformity was previously assessed using a Chroma standard, the evanescent uniformity was not examined in this way. In other words, the ability of the MesoTIRF illuminator to pick out fine spatial detail across the full 4.4 mm x 3.0 mm FOV was yet to be studied. Figure 3.8 shows a 4.4 mm x 3.0 mm FOV dual-color MesoTIRF image, following application of CLAHE, with focal adhesions in magenta and F-actin in cyan. Yellow boxes show digitally zoomed images of six separate ROIs separated by a minimum distance of 0.5 mm. In all images, focal adhesions and the F-actin network adjacent to the basal cell membranes are clearly visible. We note that there is a less than a 50% decrease in fluorescence signal from the centre to the edge of the imaged field, which we attribute to the Gaussian intensity profile of the illumination

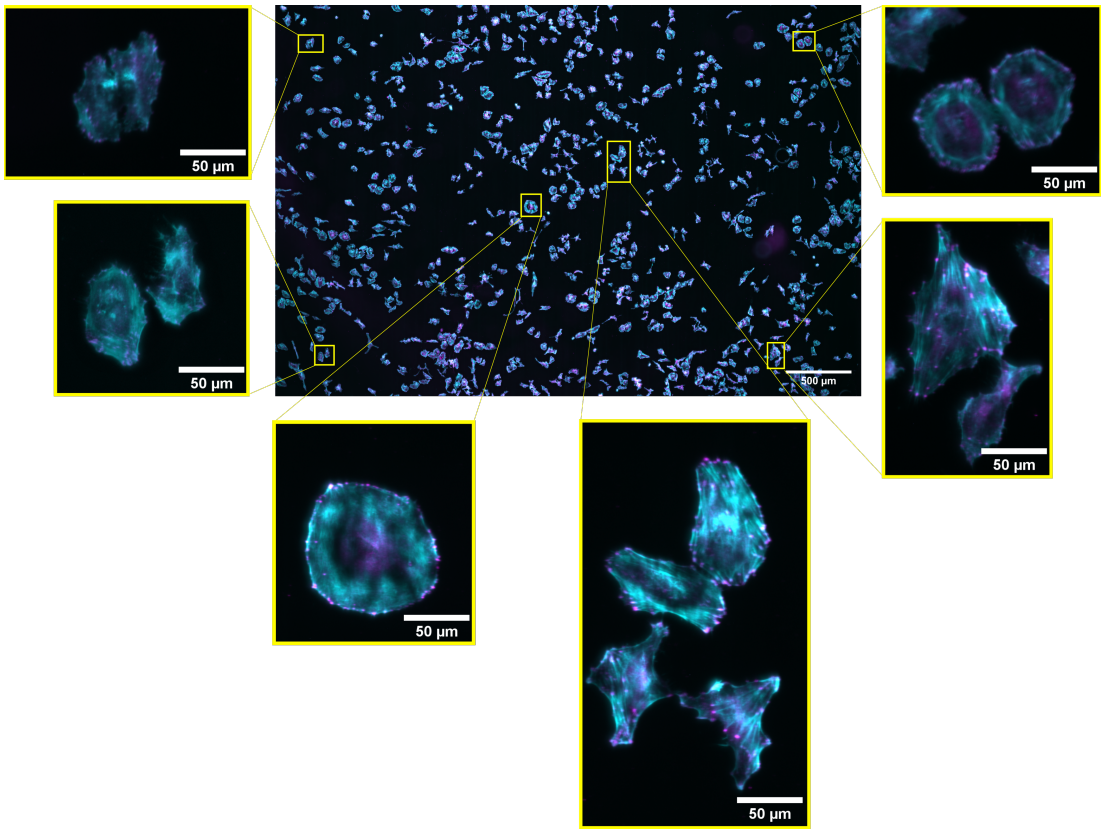

Figure 3.8: Uniformity of MesoTIRF: fixed HeLa cells labelled with an anti-paxillin antibody conjugated to Alexa Fluor Plus 594 (magenta) and Fluorescein Phallodin, which stains the actin cytoskeleton (cyan). A full FOV MesoTIRF image is shown in the centre with six ROIs indicated by yellow boxes. These show digital zoomed areas from the original dataset and confirm a small variation in the fluorescence intensity and little difference in the resolvable detail across the multi-millimetre FOV.

yielded from the optics chosen in Figure 3.2.1.

Here, a quantification of the number of focal adhesions that can be resolved across the 4.4 mm x 3.0 mm FOV serves here as a determination of the evenness of illumination. To this end, the indicated ROIs of the 585 nm (paxillin) channel of Figure 3 in the main manuscript was analysed in Figure 3.9. A pixel intensity value of 500 counts was subtracted from each image, as this removed the majority of the non-specific background in ROIs labelled A1 - F1 in the centre of the cells. The polygon selection tool in ImageJ was then used to segment each resolvable focal adhesion, shown in Supplementary Figure 3.9 A2-F2. Here, a single resolvable feature was considered as unbroken

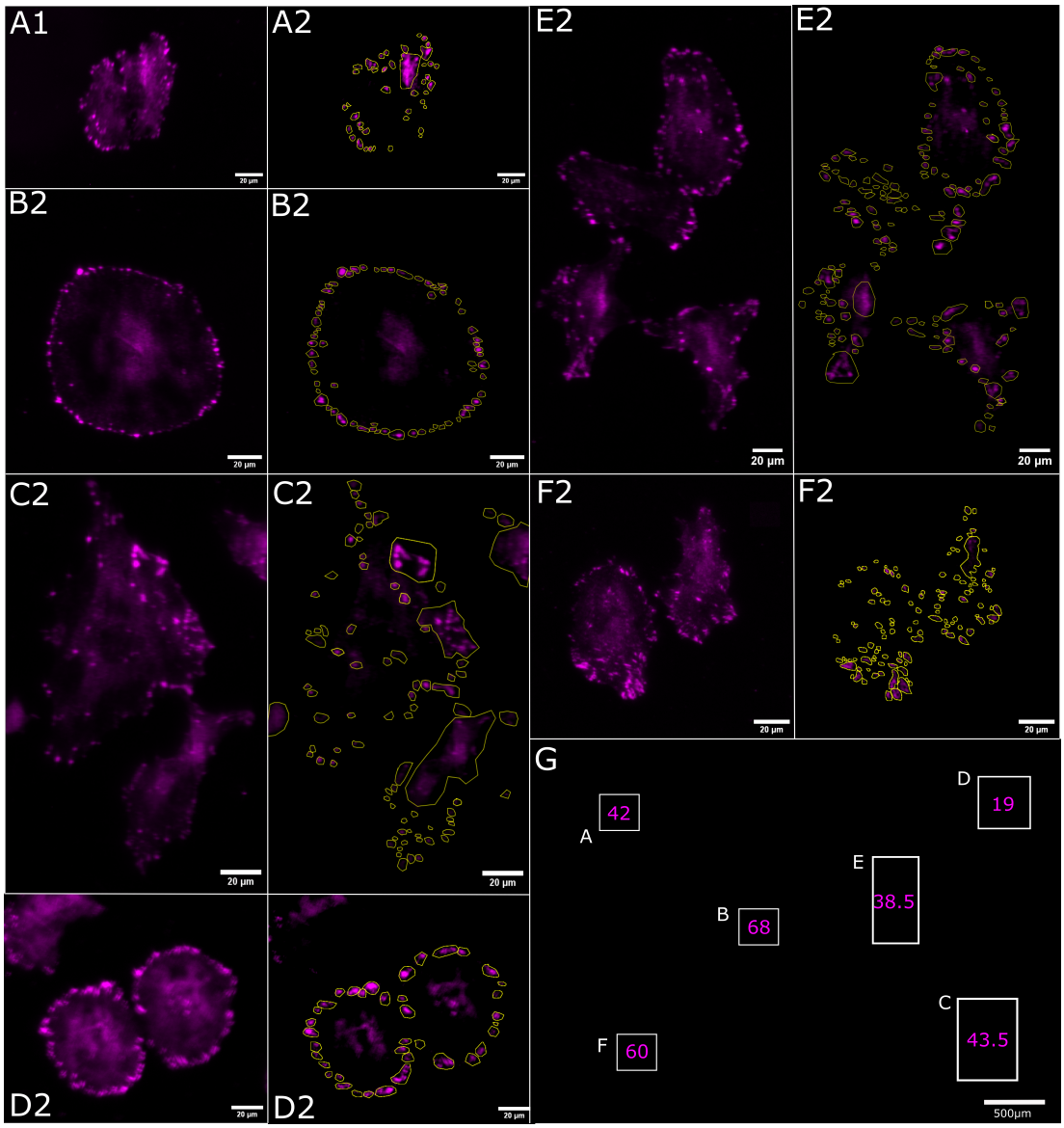

Figure 3.9: Quantification of uniformity of MesoTIRF illumination using number of resolvable focal adhesions/cell across Mesolens FOV. A1 - F1: 585 nm laser line channel imaging paxillin for complementary region of interest in panel G. A2 - F2: manually segmented focal adhesions. G: indication of number of resolvable focal adhesions per cell in indicated ROI at position in full FOV.

fluorescent signal surrounded by low (dark) background. This resulted in relatively large areas being considered as a single focal adhesion even in the clear instance in ROI C1 where four higher intensity regions are seen and could be considered as four focal adhesions. These peaks are connected by a non-negligible background, so was determined to only be a single resolvable point. This same approach was used for manual segmentation of all ROIs.

Similar numbers of resolvable focal adhesions per cell were measured in the center the field (B) and the periphery (F), with 60 and 68 resolvable focal adhesions per cell respectively. Analysis demonstrates that inhomogeneity in the illumination profile across the large FOV does not lead to differences in the number of focal adhesions that can be resolved. Therefore, any measured difference in the number of focal adhesions per cell is due to the different morphologies of these imaged cells and is not an artefact of the illumination.

Widefield epifluorescence following MesoTIRF photobleach

To study the localised photobleaching under constant MesoTIRF irradiation, cells were prepared and imaged following the protocol outlined in Chapter 3.2.2 and schematically represented in Figure 3.3. These images are shown in Figure 3.10. A reference image of the specimen in widefield epifluorescence was obtained before continuing to image (3.10A). Following a 2 hour bleach under constant illumination with MesoTIRF (3.10C - 3.10D, with photobleaching rate shown in 3.10E), the evanescent fluorescent intensity dropped to 31% of the maximum pre-imaging. However, when reimaged in widefield epifluorescence with the same imaging parameters (3.10E) bulk fluorescence intensity throughout the sample dropped to only 74% of its initial value (as shown by purple and blue data points in Figure 3.10E. This indicates a localisation of photobleaching, which is expected of TIRF and MesoTIRF, and software enabled shuttering has now been installed for future timelapse MesoTIRF imaging to minimise this. This result is further confirmation of the optical sectioning ability of this novel modality, with conventional, sub-critical illumination, the full depth of field of the Mesolens would be bleached in the specimen.

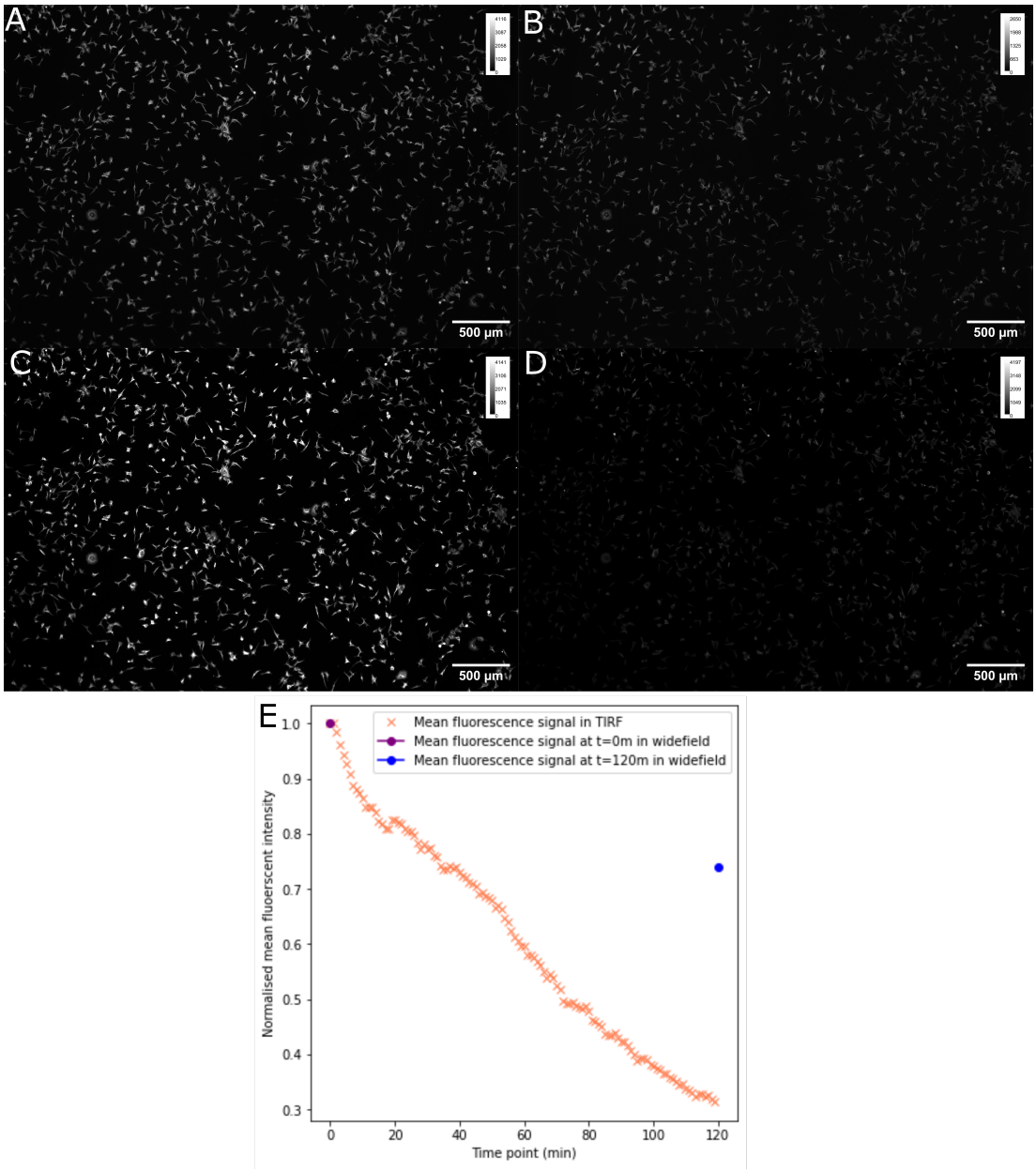

Figure 3.10: Localised photobleaching in MesoTIRF modality demonstrated by imaging in widefield epifluorescence before and after a 2 hour bleach of the TIRF optical section. A: full FOV Mesolens image of HEK-293 cells labelled against tubulin with AlexaFluor 594 imaged in widefield epifluorescence at t = 0 min (before bleaching in MesoTIRF) , B: full FOV Mesolens image of HEK-293 cells labelled against tubulin with AlexaFluor 594 imaged in widefield epifluorescence at t = 120 min (after bleaching in MesoTIRF), C: full FOV Mesolens image of HEK-293 cells labelled against tubulin with AlexaFluor 594 imaged in MesoTIRF at t = 0 min. D: full FOV Mesolens image of HEK-293 cells labelled against tubulin with AlexaFluor 594 imaged in widefield epifluorescence at t = 120 min E: Linear photobleaching decay plot from 2 widefield epifluorescence images and MesoTIRF time series.

Further fixed mammalian cell specimen imaging with MesoTIRF illuminator

To demonstrate the wider applicability of MesoTIRF a different cell line (MeT-5A) was cultured, fixed, and fluorescently labelled against tubulin and paxillin. This result, Figure 3.11, confirms the contrast enhancement and improvement in image quality expected of TIRF was achieved over hundreds of cells simultaneously, and was not a specimen dependent effect. The highlighted ROIs (3.11B and C) clearly visualise the punctate focal adhesions and bundles of spindled microtubules against a dark background in MesoTIRF. The variable density of cells across the substrate is also apparent due to the large FOV (4.4 mm x 3.0 mm) of the MesoTIRF image. Using a conventional TIRF objective, a comparable FOV could only be observed after extensive stitching and tiling of multiple images; a time consuming process which is not necessary with MesoTIRF. This is a clear example of the Mesolens, and specifically the MesoTIRF illuminator, quickly detecting rare events that would be otherwise missed by a conventional objective lens.

3.4 Discussion

This Chapter has detailed the characterisation of MesoTIRF and the subsequent imaging of a range of different biological samples. Coupling a custom prism TIRF illuminator with the Mesolens [71] provides an unprecedented combination of a large FOV with high spatial resolution and high contrast image quality. The 25 fold improvement in optical throughput of the Mesolens [71] facilitated lower optical power specimen illumination with corresponding reductions in photobleaching and phototoxicity than that of imaging with a conventional 4x microscope objective lens. The MesoTIRF modality was based on the prism illumination method, allowing for ease when changing evanescent field depth by varying the incidence angle of the incident beam, and for much reduced manufacturing costs.

As the means of characterising evanescent field depth presented in Chapter 2 proved to not be reproducible, confirmation of the generation of evanescent illumination was achieved using fixed mammalian cell specimen dual-labelled for the cell nuclei and the

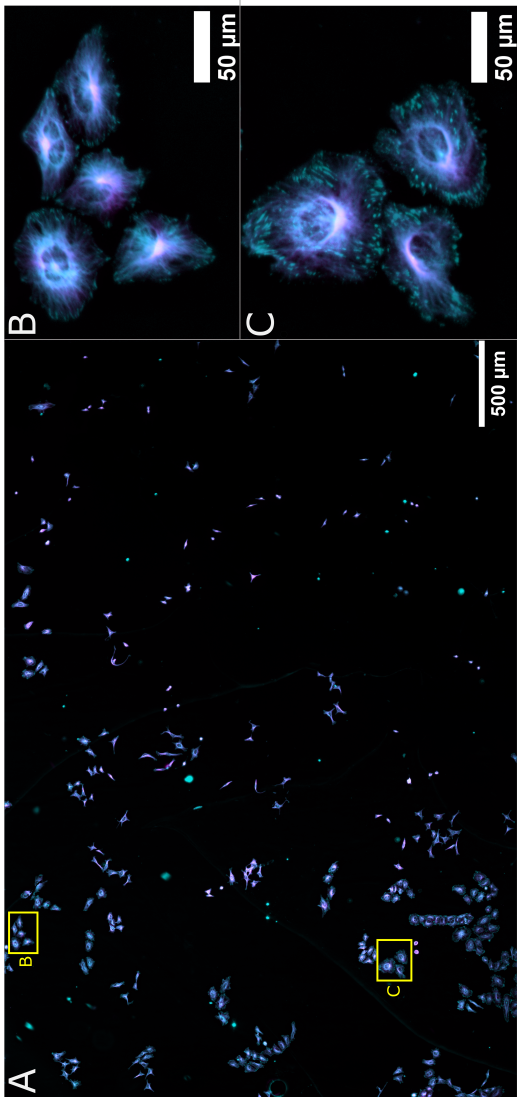

Figure 3.11: MesoTIRF image of fixed MeT-5A cells labelled for tubulin with Alexa Fluor Plus 594 (magenta) and paxillin with Alexa Fluor 488 (cyan). (A) A full FOV MesoTIRF image, with two ROIs separated by several millimetres indicated by yellow boxes, and denoted by 3.11B and 3.11C. These insets B and C on the right show digital zoomed areas from the original data set, and show little change in fluorescence intensity and resolvable detail across the multi-millimetre FOV.

focal adhesion protein paxillin residing in the plasma membranes. It is noteworthy that the position of the nuclei will be dependent on where in their life-cycle the cells were at the point of formaldehyde fixation [94]. However, it was expected that the nuclear envelopes of each imaged cell rendered the nuclei, on average, as sufficiently distal from the basal cell membrane [94] such that they were beyond the penetration depth of an evanescent field occuring at the basal cell membrane.

The ability of the MesoTIRF modality to capture fine details and the contrast improvement over WF epi was examined using a fixed mammalian cell line labelled for the focal adhesion component paxillin [95]. Using the intensity signals through neighbouring focal adhesions, an average 4.2-fold improvement in SBR was measured in MesoTIRF over WF epi, with the improvement in contrast allowing for more focal adhesions to be resolved with this novel modality (Figure 3.5), while additionally yielding some topographical information, Figure 3.9

The drop off in intensity from the centre to the edge of the MesoTIRF FOV was to be expected for an evanescent field generated using a Gaussian beam. This can be corrected either optically with beam shaping components to change the Gaussian profile to, for example, a top-hat [96], or computationally, with algorithms such as flatfield correction [97], a commonplace post-processing technique for many imaging modalities.

However, as evident from the chosen ROIs in Figure 3.9, the structural detail resolvable even in these dimmer peripheral areas remains of the quality expected of TIRF,

with the same low background and individual punctate focal adhesions and spindled actin filaments that would be blurred by fluorescent signal excited from deeper in the cell in WF epi. A quantitative analysis of this uniformity, both from the biological specimen image provided in Figure 3.11 and with a uniform non-biological test specimen, is shown in Figure 3.9 and 3.4

Excitation wavelengths for MesoTIRF are presently limited to the two discussed here by the large diameter Pinkel-type custom filters [98] used for fluorescence detection. Additional custom filters would allow this to be extended for further wavelengths.

Mesolens data are rich in information [99] but we recognize that an imaging rate of 0.2 Hz for MesoTIRF is insufficient for several applications *in vitro*, such as cell signalling studies as reported by Crites et al [100]. However, with recent innovations in camera technologies, notably the development of cameras using large, high resolution 250 Mpixel sensors such as the Canon 2U250MRXSAA CMOS sensor, tenfold higher imaging speeds (2.4 fps) can be achieved by avoiding the need for chip shifting. Additionally, sensor shifting technology has advanced in recent years, a new sensor shifting camera providing a 604 MPixel image with a 1.5 fps imaging speed is now commercially available (VNP-604MX-MC-6-H, Vieworks). In combination with environmental control, this will offer opportunities to study faster dynamic processes, for example, the action of fast-acting antimicrobial peptides [101] or imaging of calcium transients in the plasma membrane [86].

MesoTIRF may have applications in high-content screening [50] or wound healing models [102], where large cell populations must be imaged to obtain statistically significant results. However, at present MesoTIRF is only compatible with imaging at room temperature as there is no environmental imaging chamber that is compatible with the Mesolens. We are presently considering chamber designs that would be suitable for long-term imaging applications including MesoTIRF.

A present limitation of MesoTIRF is the numerical aperture of the Mesolens: at 0.47, this is much lower than a typical TIRF lens and hence the lateral resolution is around three-fold poorer than a commercial objective TIRF microscope. With the principle of MesoTIRF now proven, one solution would be to increase spatial resolution

using structured illumination [103], [104] introducing the possibility of super-resolution MesoTIRF-SIM. However, achieving SIM on the Mesolens is not trivial and would require either further optics in the MesoTIRF path to impose variable modulation patterns on the incident excitation beam or utilising computational methods such as blind-SIM [105] algorithms. This would facilitate applications in single molecule localisation microscopy in cell specimens approximately two orders of magnitude larger than current technology can image. At present we are again limited by the chip-shifting camera technology, but we are carefully following developments in this field.

The analysis here was carried out over a few ROIs for the purposes of presenting the MesoTIRF modality as a tool for identifying structural features of a specimen of interest and while most focal adhesions are observed in both modalities, the contrast improvement expected (and measured) of MesoTIRF allowed for more informative study of the focal adhesions under examination.

Chapter 4

Standing wave mesoscopy

4.1 Introduction

Standing wave (SW) microscopy [57] is a simple imaging technique for obtaining axial information from a 2D image. A thorough introduction is provided in Chapter 1, and so only the main principles are reviewed here in brief.

In SW microscopy, no adaption to the microscope is required. Instead, the specimen preparation is modified slightly such that the specimen is mounted between a first surface reflector and a coverslip. The mirror surface imposes a π phase change on the incident excitation light upon reflection such that the incident and reflecting wave interfere with each other, generating planes of constructive and deconstructive interference. In the antinodes of this standing wave, bands of fluorescence are excited from a fluorescently labelled specimen, the thickness and separation of which are dependent on the wavelength of light and height from the mirror surface. Therefore, using this setup, detail below the axial diffraction limit of the imaging objective can be extracted from a single widefield 2D image. This topographical extension to fluorescence microscopy, [58], [60], has been further developed to fill the gaps left by the nature of a standing wave using different excitation wavelengths. This method is called TartanSW microscopy, [61].

In an effort to extend SW imaging from the microscale to the mesoscale, we proposed using the same simple setup with the Mesolens (see Chapter 1.7). The ideal configu-

ration for SW imaging is using an objective lens with a low magnification to visualise large cell populations while retaining high lateral resolution in order to examine sub-cellular structure and to resolve axial anti-nodal fringes from the 2D acquired image. Such a system would allow for analysing cell population heterogeneity and detection of rare events in large populations. The unusual lens prescription of the Mesolens and how this allows for high resolution imaging across millimetre length scales in discussed in depth in Chapters 1 and 3. This prescription of the Mesolens gives rise to a 25-fold increase in optical throughput when compared against a conventional 4x/0.1NA microscope objective lens, allowing for a significant increase in optical brightness.

Ultimately the limiting factor for standing wave imaging is whether the lateral profile of fluorescence emission which is excited by axial anti-nodal fringes can be resolved with the imaging objective lens. This both depends on the NA of the objective lens and the topography of the specimen. As an example, using equation (1.29) using standing wave illumination with the epifluorescence path of the Mesolens, choosing a 490 nm LED (to excite conventional dyes/proteins such as FITC/GFP) propagating through a specimen mounted in water (n = 1.33) would yield an anti-nodal FWHM of 92 nm (as calculated from equation (1.29)).

The Mesolens has previously been demonstrated operating as the imaging objective for confocal laser scanning microscopy across a several cubic millimetre imaging volume, [71], [106], but this process is slow to point-scan across the full field. In context, to acquire a confocal z series with the Mesolens with a reduced imaging volume of 4.4 mm x 3 mm x 20 µm specimen at Nyquist sampling (4 px/µm in the lateral dimension and 10 images in the axial direction), a pixel dwell time of 1 µs and a frame average of 2 takes 1.17 hours [71]. Using confocal laser scanning illumination on a commercial microscope system and stitching and tiling together multiple smaller FOVs of the same resolution to acquire a similar volume takes a comparable amount of time. A means of illumination which reduces this acquisition time significantly is light sheet microscopy, [70], [74], [107], [108] which uses complex optical systems to focus illumination to a long diffraction limited focus in the specimen plane such that a sheet of light is scanned through one lateral dimension and rastered through z rather than using point wise

illumination. This now well utilised technique lends itself well to imaging full cleared bodies and organs with near isotropic resolution [107], however the alignment of the optics required is very much non-trivial and only single excitation wavelengths have thus far been demonstrated with the Mesolens, [74].

In this Chapter, SW illumination has been combined with the Mesolens to achieve high resolution imaging of different specimens which enables axial detail to be elucidated from a single 2D image. A confirmation of SW illumination was performed with a fluorescently labelled glass plano-convex lens specimen, allowing for the FWHM of the axial fringes to be obtained. Furthermore, multi-wavelength standing wave (TartanSW) images of more than one hundred fixed and labelled fibroblasts were acquired, as well as imaging of more than 16,000 live red blood cells with high lateral and axial resolution. This method was also applied to study a large population of cells that were genetically modified to express green fluorescent protein (GFP) in the GLUT4 receptors.

4.2 Methods - specimen preparation

The following methods detail the means of culturing and fluorescently labelling specimen for the SW mesoscopy imaging in this Chapter.

4.2.1 Preparation of large fluorescent lens specimen

Due to the large FOV of the Mesolens, a larger diameter lens specimen with a larger radius of curvature than those used for the characterisation of traditional standing wave microscopy was required, [58], [60], [61]. This was required to record to the best of the lens' and camera's ability, the antinodal fringes observed as fluorescent lateral fringes in the periphery of the imaging field. While in principle the same experiment could be attempted on a standard 4x microscope objective, one would not be able to resolve the antinodal fringes with the poor lateral resolution of these lenses.

As such, a 400 mm focal length plano-convex lens specimen (400 PQ 25, Comar Optics) was chosen as its radius of curvature (equation (2.1)) would allow for resolving fringes across the Mesolens FOV. This lens was coated with a layer of poly-l-lysine

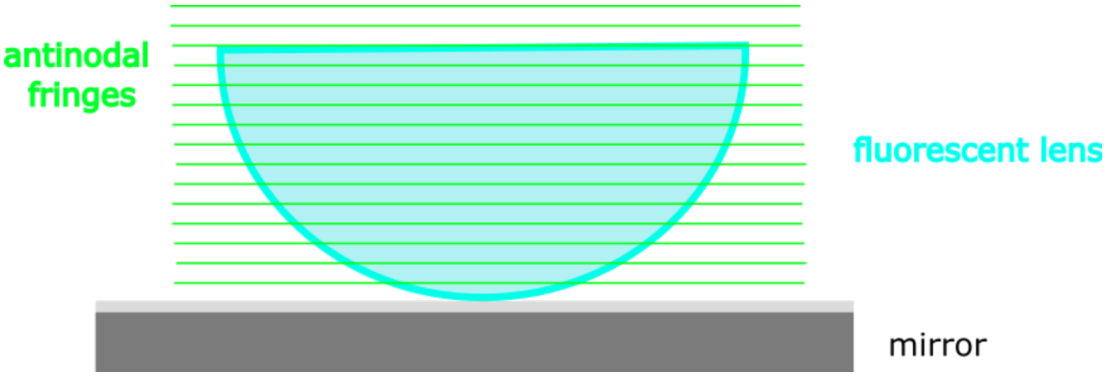

Figure 4.1: Schematic illustration of a fluorescently coated plano convex lens specimen of known radius of curvature R on mirror surface to measure antinodal fringe spacing.

before coating with a 10 µM solution of DiO (3,3'-Dioctadecyloxacarbocyanine Perchlorate) (D275, Thermo Fisher, Paisley, UK). DiO was chosen as the dye's excitation and emission profiles are broad, and both single wavelength and TartanSW characterisation was desirable. The radius of curvature of this lens was calculated using the thin lens formula, [12], to be 208 mm. For imaging, this prepared lens specimen was placed convex side down on a high flatness ($\lambda/10$) first surface reflector (TFA-20C03-10, Laser 2000, Huntingdon, UK) as shown schematically in Figure 4.1. For the purposes of obtaining a proof of concept lens specimen image to confirm the presence of standing wave excitation with the Mesolens, this set up was imaged with no fluid mountant, that is the lens was imaged in air to ensure the specimen was flat to the front element of the Mesolens. While the Mesolens is not corrected for imaging in air, for the purposes of imaging standing wave antinodes from a known geometric surface, this was suitable.

4.2.2 Preparation of fixed mammalian cell specimen for proof of concept imaging

Fibroblast murine cells (3T3-L1) were maintained in culture, at 37°C, 5% CO2 in supplemented DMEM (see Appendix B). The mirrors described above for imaging with a lens specimen were cleaned in 100% ethanol and UV sterilised in a microbiological safety cabinet. The mirrors were then placed reflective side up in 6 well plates, thoroughly washed with sterile PBS to remove any residual ethanol, and submerged in a

1:500 dilution of fibronectin bovine plasma (F1171-2MG, Sigma Aldrich) in PBS for 30 minutes at room temperature before seeding with cells to the desired density. Seeded cells were incubated for 24 hours to achieve approximately 80% confluence and to allow for adherence to the mirror surface.

Confluent adherent cells were then rinsed with PBS and incubated with 4% PFA for 20 minutes. Following three PBS wash steps, the fixed cells were then blocked and permeabilised with a buffer of FBS and Triton-X100. The F-actin of the cells were labelled with a 1:2000 dilution of fluorescein phalloidin in the buffer solution, by incubation at room temperature for 20 minutes in light tight conditions. Following three PBS washes to remove any unbound dye, the plated cells were sandwiched between the cultured mirror surface and a large 70 mm x 70 mm type 1.5 coverslip (0107999098, Marienfeld, Lauda-Koenigshofen, Germany) to allow for the large column of immersion water required to utilise the full NA of the Mesolens.

4.2.3 HA-GLUT4-GFP 3T3-L1: axial study of glucose transporter immortalised cell model

Embryonic mouse fibroblast cells can be induced to differentiate into adipocyte (fat) cells with a protocol involving a steroid, an AMP inhibitor and insulin [109]. This differentiation process is of particular use for laboratory study of molecular pathways relevant to glucose uptake into the fatty cells and the means by which this is compromised in Type 2 diabetes. The trafficking of the glucose intracellular transporter protein GLUT4 is known to be regulated by insulin stimulation [110]. To study this trafficking in detail, researchers have developed a stable fluorescently labelled 3T3-L1 cell line which expresses GFP intracellularly from within glucose transporting vesicles whose lipid bilayer is embedded with GLUT4 molecules, and a human influenza hemagglutinin (HA) epitope in the first extracellular loop of the GLUT4 molecule. This HA epitope can be immunofluorescently labelled with any anti-mouse secondary antibody. In the basal state (i.e. in the absence of insulin) GLUT4 freely diffuses within cells, docking spontaneously with the plasma membrane and recruiting glucose from the extracellular space. In the presence of insulin, binding events of GLUT4 containing

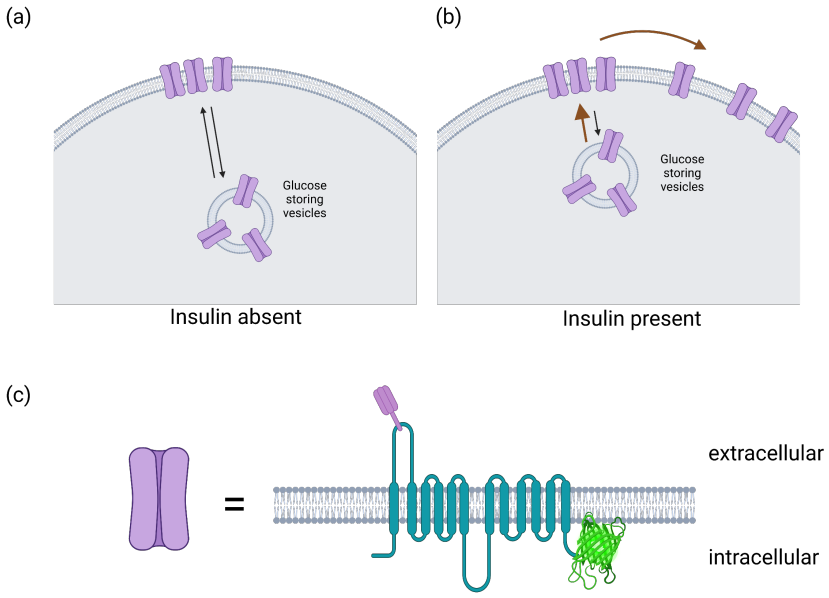

Figure 4.2: Schematic illustrating GLUT4 trafficking in insulin responsive cells. (a) in basal state, GLUT4 storing vesicles dock spontaneously with plasma membrane, but this process is up-regulated 60 fold in presence of insulin (b) [111]. (c) stable murine 3T3-L1 cell line used to study GLUT4 trafficking with HA epitope conjugated to the first extracellular loop of the molecule and a GFP molecule conjugated on the terminus intracellular end of the GLUT4 molecule. Figure made in Biorender (Kay Polland, agreement number: BY25LAR7HL).

vesicles are increased 60 fold [111]. This process is illustrated in Figure 4.2.

As fibroblast and adipocyte cells have dramatically different axial morphologies, SW mesoscopy was proposed as a technique to quantify the percentage of adipocytes in cell population across the hundreds of cells which could be visualised from one frame on the Mesolens. This was hypothesised as the axial profile of populations of fibroblasts which are flat and filamentous [112] and adipocytes which have spherical phenotypes [113], as shown in Figure 4.3, would be discernable from a single SW mesoscopy image. In principle, flatter filamentous fibroblasts should intersect with fewer fluorescent antinodal fringes while spherical, highly curved adipocytes should intersect with more.

Specimens of HA-GLUT4-GFP 3T3-L1 [114] were cultured, differentiated and plated

Figure 4.3: Schematic illustration of fibroblast and adipocyte 3T3-L1 cells with GLUT4 molecules fluorescently tagged under same illuminating standing wave field.

onto sterilised first surface reflectors by Angéline Geiser (SIPBS, University of Strathclyde). Following adherence to the mirror surface after 24 hr incubation at 37°, 5% CO_2, the cells were fixed in 4% paraformaldehyde and the HA epitope was targeted with an AlexaFluor405 anti-mouse secondary (Abcam, ab175660). The plated mirror surfaces were then submerged in Immuno-Mount before being topped with a large 70 mm x 70 mm type 1.5 coverslip (0107999098, Marienfeld, Lauda-Koenigshofen, Germany) to allow for water immersion on the Mesolens without immersion leaking into the specimen. Three different time points through differentiation where imaged with SW mesoscopy, day 0, day 3 and day 8. It follows that day 0 post differentiation is a fully fibroblast cell population, day 3 or 4 is part way through differentiation and so there is a mixed population and day 8, 9 or 10 is a predominantly adipocyte cell population.

4.2.4 Live red blood cells

Human red blood cells (or erythrocytes) are small bi-concave cells which lack a nucleus, mitochondria and other organelles. Their primary function involves a protein called haemoglobin which transports oxygen from the lungs to other parts of the body and recycles carbon dioxide back to the lungs [115]. The characteristic bi-concave shape of the red blood cell allows for continual deformation as the cell flows through capillaries. It also increases the surface area of the cell membrane to allow for optimised diffusion of oxygen and carbon dioxide into and out of the cells. Red blood cells have been measured using electron microscopy; their cell width is between 7-8 µm and their height including the edge thickness of the non-deformed bi-concave membrane is on the order of around 2.5 µm [115]. Abnormalities in the 3D membrane of red blood cells can be early

indicators for blood disorders such as anemia, parasitaemia and other diseases of the blood including hereditary spherocytosis, sickle cell disease, hereditary stomatocytosis or elliptocytosis [116].

Human erythrocytes ($\simeq 0.5$ mL final volume) were collected through fingertip needle puncture. A 100 µL volume of a 5µg/mL FM4-64 working solution (T13320, Thermo Fisher, Paisley, UK) in non-sterile water was spiked into an aliquot of the red blood cell specimen. Following a 1 minute light-tight incubation at room temperature, either 10 µL or 50 µL of this stained suspension was added directly to sterile mirror surfaces. The 10 µL cell suspension was created a scenario where cells were almost all in contact with the mirror, while the 50 µL suspension was used to image cells in a flow environment. This was required as currently there are no flow chambers of a size suitable for imaging with the Mesolens which have a first surface reflector base. The mirror prepared with the 10 µL cell suspension was allowed to settle for 2 minutes at room temperature in the dark, while the specimen prepared with the 50 µL cell suspension was imaged immediately, with no time for the cells to settle on the mirror. In both situations, the specimens were topped with a large 70 mm x 70 mm type 1.5 coverslip (0107999098, Marienfeld, Lauda-Koenigshofen, Germany) to allow for water immersion on the Mesolens without immersion leaking into the specimen.

4.3 Methods - imaging parameters

A diagram of the imaging setup for standing wave illumination with the Mesolens is shown in Figure 4.4. The Mesolens was used in widefield epifluorescence mode with an LED illuminator (pE-4000, CoolLED, Andover, UK) to sequentially deliver wavelengths of 385 $\pm$ 15 nm, 430 $\pm$ 20 nm, and 490 $\pm$ 20 nm to the specimen plane. The resulting fluorescent emission from a specimen was propagated through multi-bandpass (Pinkel-type, [98]) emission filters. These filters were used to detect fluorescence emission at 417 $\pm$ 10 nm, 460 nm $\pm$ 10 nm, 525 nm $\pm$ 25 nm, and 635 $\pm$ 20 nm. Tinning et al, [60], have previously demonstrated with single wavelength SW microscopy that it is not necessary to use a light source with a long coherence length for SW microscopy/mesoscopy, and as such LEDs are suitable for this purpose, [60].

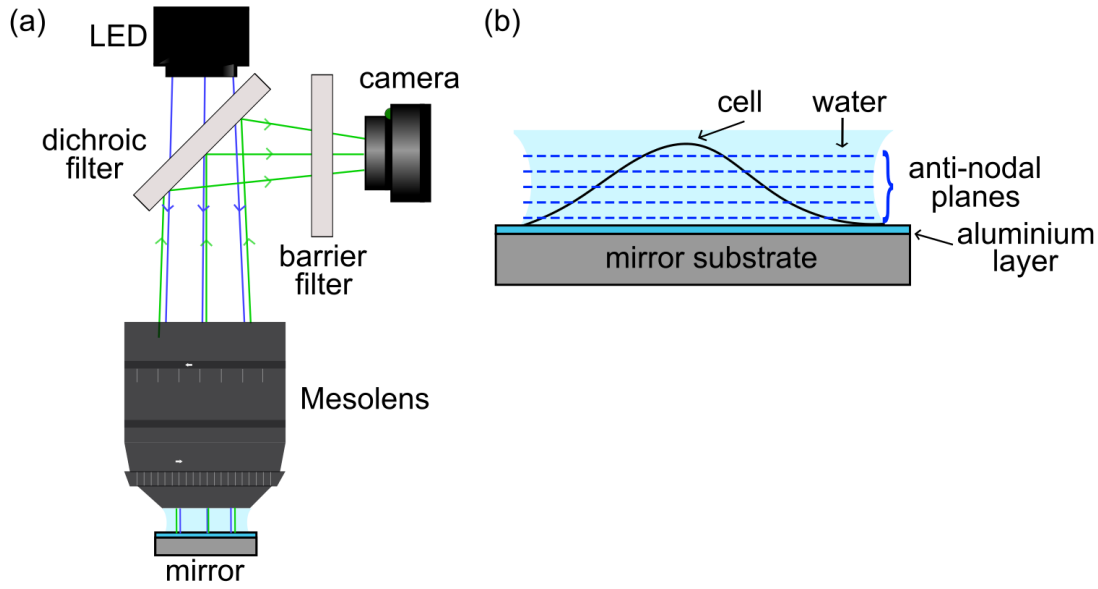

Figure 4.4: Setup for standing wave illumination with the Mesolens. (a) LED ray diagram illumination in blue, fluorescence emission in green. (b) Schematic blown up view of plated mirror surface at specimen plane in (a). Here, a mammalian cell specimen is shown attached to the aluminium surface of the mirror, anti-nodal planes (dotted lines) representing bands of high fluorescence intensity. Not shown to scale.

Single-wavelength SW images of the lens specimen were acquired with 490 ± 20 nm excitation with 1.36 kW/m^2 irradiance at the specimen plane of the convex lens surface, with a 1,000 ms camera exposure and gain of 50x, to obtain sufficiently high fluorescence intensity counts from the monolayer of dye on the otherwise transparent surface.

TartanSW images of the fibroblast cells were obtained using sequential wavelength excitation from all three LEDs: 385 ± 15 nm with an average irradiance of 1.14 kW/m^2, 430 ± 20 nm with an average irradiance of 234 W/m^2, and 490 ± 20 nm with an average irradiance of 371 W/m^2, with all power values measured at the specimen plane. The exposure time was longest for the shortest wavelength at 5,000 ms, and this was decreased to 800 ms at 430 ± 20 nm, and 200 ms for the longest wavelength of illumination. The camera gain was set to 80x for imaging at 385 nm, and this was decreased to 40x for imaging with both 430 ± 20 nm and 490 ± 20 nm. Images from the three different channels were saved individually for analysis and processing.

Day 0 post differentiation HA-GLUT4-GFP 3T3-L1 cells were imaged with 490 nm LED excitation with 1.86 kW/m^2 irradiance exciting the intracellular GFP tag, a 1 s exposure time and 50x camera gain. Day 3 post differentiation cells were imaged for both the intracellular GFP tag with 490 nm LED excitation with 1.02 kW/m^2 irradiance, 1 s exposure time and a 1x camera gain and for the extracellular HA epitope conjugated to an AlexaFluor405 secondary antibody, excited with 435 nm LED illumination with a 0.33 kW/m^2 irradiance, a 2 s exposure time and a 40x camera gain. Day 8 post differentiation cells were imaged with 490 nm LED excitation with 1.67 kW/m^2 of the intracellular GFP tag, a 1 s exposure time and 25x camera gain.

Images of red blood cell specimens prepared as described in Section 4.2.4 were acquired with 490 $\pm$ 20 nm excitation at 371 W/m^2 irradiance from the illuminator with a 100 ms camera exposure, and a gain of 40x. Time-lapse recording of the red blood cell specimens was also performed, with 10 images acquired from the high-volume cell suspension preparations, and 30 images acquired from the low-volume cell suspensions using a 30 s time interval between recordings.

4.4 Methods - analysis techniques

4.4.1 Relating 2D lens specimen image to axial antinodal fringe spacing

The lens specimen image illuminated under SW mesoscopy was contrast adjusted using the Contrast Limited Adaptive Histogram Equalization (CLAHE) [117] function in FIJI [89] with the default parameters (blocksize = 127, histogram bins = 256, maximum slope = 3.00).

As the geometry of the lens specimen was well defined, relation between the lateral fringe spacing from the 2D image of the specimen could be related to height from the mirror surface using a MATLAB script developed by Scrimgeour [60], [118]. This analysis required that the input images loaded into MATLAB were square, centred on the zeroth order node (where the fluorescent lens surface is directly on the mirror surface and in a region of deconstructive interference) and had been processed with a

Gaussian filter (σ= 200). Once the image was loaded, the code extracted a number of line profiles from the centre and edge of the lens to the edge of the cropped image and performed a radial average of the fluorescence intensity values using the custom function *radialavg* [119]. Here, 6,432 lines were measured as the code generated half as many radial profiles as there were pixels in the image width. Using the obtained average lateral intensity profile, Pythagoras' theorem was then used to relate this to height from the mirror surface using the known spherical geometry of the lens specimen. Therefore, the axial height of the fringes d could be obtained from the radial distance of each pixel from the centre of the image r and the radius of curvature of the lens quoted by the manufacturer R:

$$d = R - \sqrt{(R^2 - r^2)} \tag{4.1}$$

To quantify the average FWHM, and therefore the axial resolution of the standing wave illumination, MATLAB's *findpeaks* function was used to find the intensity peaks corresponding to the maximum of the standing wave fringes. The width of these peaks was then extracted from the function and an average of these measured periodically spaced fringes was given as an output. An error on this measurement was computed by acquired multiple images with the same imaging parameters of the same lens specimen and running them through the described analysis pipeline and computing the standard deviation of the FWHM values obtained. For analysis of the FWHM obtained from this measure, the value was compared to the theoretical estimate using equation (1.29), using the illuminating wavelength (λ) of 490 nm and the refractive index (n) of 1, as the fluorescently coated air interface of the lens specimen is the origin of the emission standing waves.

It is of note that in order to run this analysis across a full field Mesolens image acquired at full resolution, the pipeline was run on a server, which was a 64-bit Windows Server 2016 Standard Operating system (v.1607) with two Intel® Xeon® 4114 CPU processors at 2.20 and 2.19 GHz and a 1.0 TB installed RAM.

4.4.2 Biological SW mesoscopy imaging processing

For each presented TartanSW mesoscopy image, sequentially acquired images with different illumination wavelengths were contrast adjusted using the 'Auto' Brightness/-Contrast function in FIJI [89] before merging to a single image with false colours red, green and blue, with red corresponding to the longest wavelength and blue to the shortest.

4.4.3 Flatfield correction

To correct for any inhomogeneity in fluorescence excitation, flatfield correction was applied to each image using SciPy [120]. The background was assumed to be its Gaussian filtered image (σ= 200) and the image was then divided by this background image. Normalisation was performed by correcting to the 5th and 99.8th percentile of the image (chosen here to maximise SNR), including clipping of all pixel intensity values outside of the range of 0 to 1. This procedure was followed in order to smooth out camera noise at low intensity counts for the relatively dim lens specimen used for this measurement.

The Mesolens is flatfield corrected across the central 5.5 mm of the imaging field, which overfills the region which is recorded by the sensor shifting camera. Flatness inhomogeneity in this work arises from a combination of non-uniformity in the LED illuminators (as discussed in Chapter 3) and from non-uniformity in mirror surfaces used. While the mirrors were purchased for their high flatness (λ/10), they were reused for experiments by cleaning with 100% ethanol and UV treating the surfaces which may have damaged the aluminium coating.

4.5 Results

4.5.1 Characterisation of standing wave pattern

As with previous standing wave microscopy studies, the fluorescently prepared plano-convex lens specimen allowed for testing whether single wavelength standing wave illumination was possible across the 4.4 mm x 3.0 mm widefield FOV of the Mesolens.

As such, Figure 4.5(a) shows one of the replicate images obtained from illuminating the lens specimen on the mirror surface with 490 ± 20 nm excitation and simultaneous dual-band fluorescence emission detection at both 525 ± 25 nm and 635 ± 20 nm wavelength ranges using the Pinkel-type filters described in 4.3. The standing wave fringes confirming standing wave excitation were observable across the central 3.0 mm x 3.0 mm section of the image. While not clearly visible, standing wave fringes are likely to extend across the full FOV, but the curvature of the lens surface coupled with the limited depth of field of the Mesolens resulted in the anti-nodal planes in this region were too laterally close together to be resolvable at the periphery of the FOV.

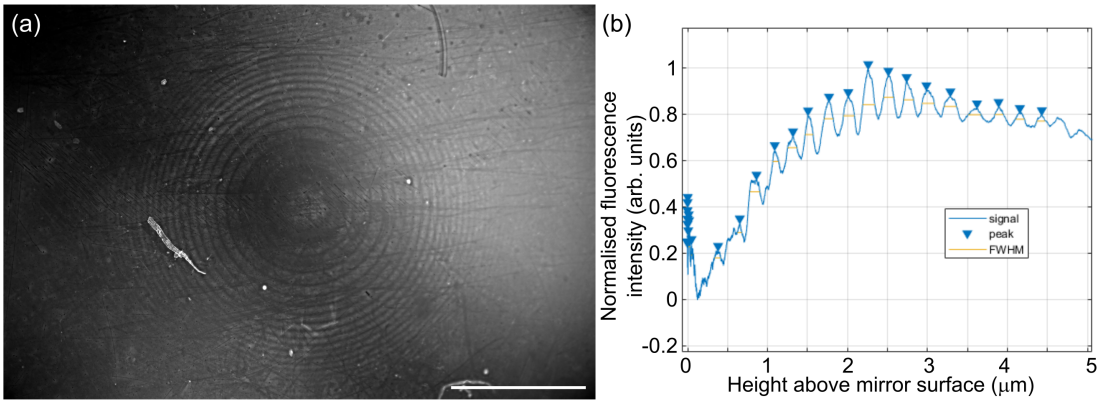

Figure 4.5: (a) Mesolens image of a DiO labelled f = 400 mm plano-convex lens specimen on flat first surface reflector. Imaged in air, n = 1. Excited with 490 nm ± 20 nm LED and detected within 525 ± 25 nm and 635 ± 20 nm. Scale bar = 1 mm. (b) Fluorescence intensity against height from the mirror surface obtained from image. Measured average FWHM thickness = 143 ± 19 nm.

Using the analysis pipeline described in Section 4.4, the average FWHM of the fringes in Figure 4.5(a) and plotted in 4.5(b) was found to be 143 ± 19 nm. DiO was chosen as the fluorescent coating for the lens specimen as it would excite under 490 nm illumination and could be bound to the lens surface simply using an electrostatic binding force with poly-l-lysine. The peak of DiO occurs at 506 nm, so with the filters in place for this imaging, described in 4.3, the image in Figure 4.5(a) was recording fluorescence across a broad spectral range. As such, the theoretical FWHM for this situation, calculated using (1.29) using n = 1 as imaging of the lens specimen was carried out in air, were between 128 nm and 161 nm (using 512.5 nm and 645 nm as

the shortest and longest detected emission wavelengths respectively). As discussed in depth in Section 1.6 of Chapter 1, there is a non-intuitive feature of SW illumination which is that there are both fluorescent excitation and emission SW patterns present. In all cases where the SW pattern is being discussed as an experimental parameter in this work, it refers to this measured emission SW.

The measured FWHM, 143 ± 19 nm, agrees well with the calculated predicted values, allowing for the assertion that standing wave illumination was being achieved across the central 3.0 mm x 3.0 mm of the Mesolens FOV.

4.5.2 SW mesoscopy of fixed mammalian specimen

Following characterisation of the illumination, SW mesoscopy was applied to the imaging of biological specimen. Figure 4.6(a) is a full field TartanSW mesoscopy image of $>$ 100 fibroblasts labelled for F-actin. The false colours represent 385 nm excitation (blue), 430 nm excitation (green) and 490 nm excitation (red), acquired sequentially through the method presented in 4.3.

The image was downsampled to 1000 pixels by 545 pixels for the purpose of presentation. Three digitally zoomed ROIs are presented in Figure 4.6(b -d) to visualise the standing wave fringes on individual cells. Figure 4.6(b) is taken from the top left of the full field (indicated by a yellow box in Figure 4.6(a)). Similarly Figures 4.6(c) and (d) are zoomed regions from the centre (indicated by a magenta box) and bottom right of the full field (cyan box) respectively.

TartanSW illumination results in multiple wavelength SW patterns, generating antinodal planes visible across the full field at different axial positions. These planes correspond to the axial height of the specimen from the mirror surface at this point, are visualised in figures using false colour rendering of merged invidual wavelength frames and confirm the suitability of the method to obtaining 3D information from a 2D image across large cell populations.

It is of note that while the fringes were likely visible across the full field, there is an area in the bottom left of the full field image in Figure 4.6(a) which highlights a much higher blue signal from the 385 ± 15 nm illumination. This could be due to residue

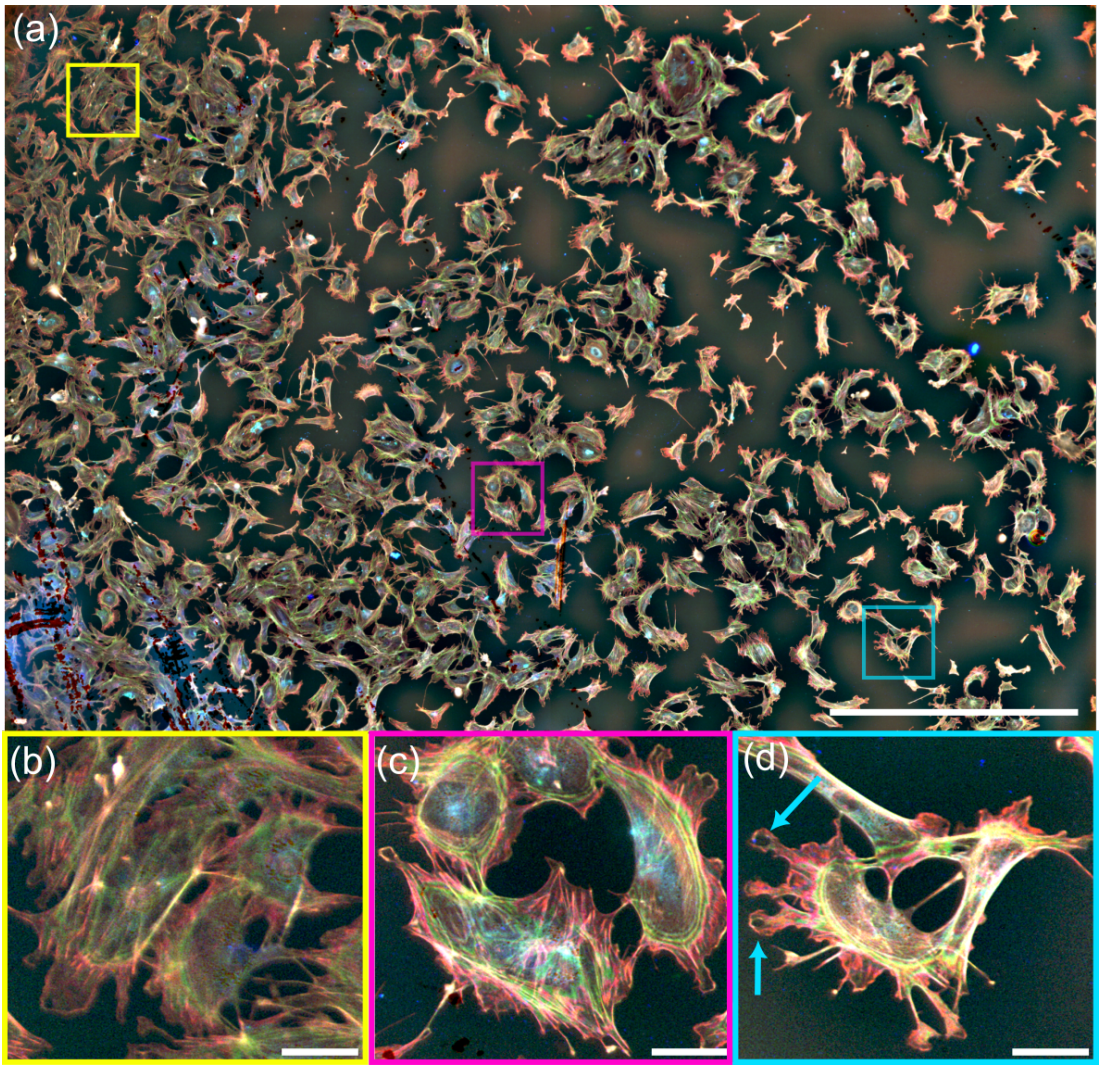

Figure 4.6: (a) Full field TartanSW mesoscopy image of 3T3-L1 cells stained for F-actin with fluorescein phalloidin. Scale bar = 1 mm. (b - d) Three digitally zoomed ROIs, yellow from top left of the field, magenta from centre and cyan from bottom right. Cyan arrows in (d) highlighting dark points in filopodia which are potentially focal adhesions. Scale bars = 50 µm.

on the mirror surface at this region leading to autofluorescence. Additionally, in the top left of the field where the ROI in Figure 4.6(b) was cropped, a lower contrast was observed. This was mostly likely a result of the specimen not being entirely flat and orthogonal to the optical axis of the Mesolens.

As a brief example of the axial detail which can be elucidated from this data, in Figure 4.6(c) the curvature of the cell can be seen on the right hand side of the image

from its leading edge closest to the edge of the image and an increase in fringes corresponding to the cell surface curving over the unlabelled nuclei and other organelles as the observer moves towards the centre of the cell. Additionally, from Figure 4.6(d), dark regions are seen in the centre of hypothesised filopodia (indicated by cyan arrows) which could potentially be focal adhesions in direct contact with the mirror and therefore within the dark node of the standing wave.

In order to confirm the results seen in Figure 4.6 were as a result of the specimen being plated on a first surface reflector and the resultant interference pattern, a control specimen was prepared identically save for plating the cells on a coverslip rather than a first surface reflector. Imaged under much increased imaging parameters (3000 ms exposure time, 50x gain and the full power output of the 490 nm LED), no fringes could be observed in this control dataset, Figure 4.7.

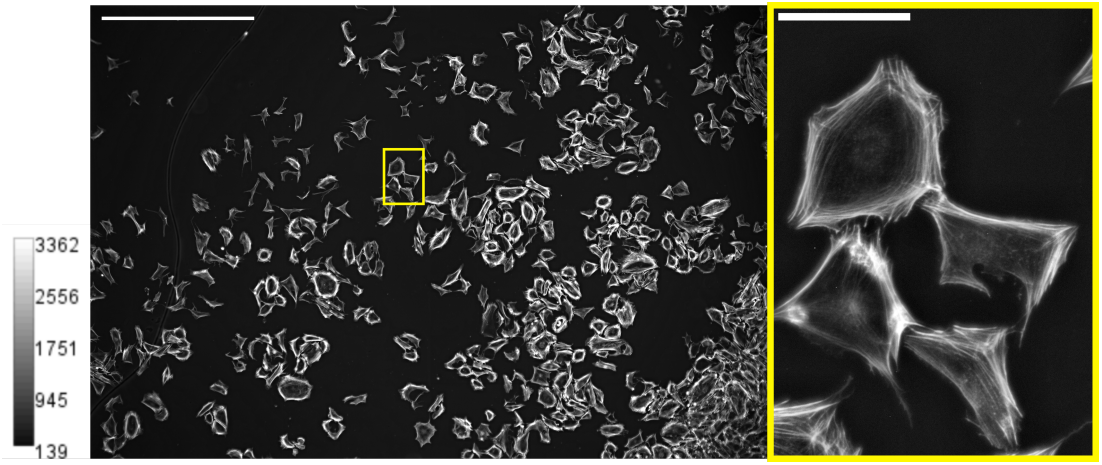

Figure 4.7: 3T3-L1 cells prepared through identical protocol to those in Figure 4.6 , plated on coverslips instead of mirrors. Widefield epi-fluorescence Mesolens image (scale bar for full field image: 1000 µm) excited with 490 nm LED (3000 ms exposure time, 50x gain and 100% CoolLED illumination power, 6.66 fold irradiance increase to presented SW equivalent. Scale bar for ROI: 100 µm. Pixel intensity bar included to illustrate fluorescence intensity counts excited.

4.5.3 SW mesoscopy study of HA-GLUT4-GFP 3T3-L1 fibroblasts differentiating into adipocytes

Following inducing differentiation, HA-GLUT4-GFP 3T3-L1s were fixed on mirror surfaces on the day of differentiation - Day 0 (cells still in fibroblast morphology), 3 days after this (beginning transition into adipocyte morphology) and 8 days after this (cells prodominantly adipocytes). Full field SW mesoscopy images of these specimens are displayed in Figure 4.8. In each dataset, the HA epitope was targeted with an AlexaFluor405 secondary antibody and imaged in sequence to the GFP tag, for clarity in presentation for the datasets of Day 0 and Day 8, a single channel has been shown to visualise the subtle antinodal fringes.

For the indicated line profile 1 in the D0 dataset (Figure 4.9A1) 4 distinct peaks are observed. The first three occur at 2.03 µm, 4.97 µm and 7.46 µm along the line profile, with an almost periodic spacing of 2.94 µm and 2.49 µm between them. The final wider peak further down the line profile is more likely a bright feature in the cell. The periodicity in this line profile indicates that the variation in intensity is indeed coming from the structured illumination of the standing wave rather than an artefact in fluorescence labelling. The lateral bunching of these fringes (relative to the others which will be discussed here) indicates a sharp change in axial topology at this point in the cell. From the data itself, it is difficult to elucidate whether this change corresponds to a flattening of the cell onto the mirror surface or an incline of membrane indicating a thicker specimen at this point

For the profile 2 (Figure 4.9A2) a convincing 9 periodically spaced peaks are detected, with the position and separation of peaks shown in Table 4.1. Relative to the previously discussed line profile, the axial features picked out by this profile indicate a steadier change in topography.

For the final line profile of D0 (Figure 4.9A3) the signal is substantially noisier. Therefore from a rough estimate, the four major (and binodal) peaks at the right hand side of the line profile are approximately 10 µm apart. As such, the significance of these peaks regarding the axial profile of the cell at this point is difficult to accurately comment on.

# peak	Position in line profile (µm)	Spacing from previous antinode (µm)
1	1.13	N/A
2	4.97	3.85
3	9.72	4.75
4	14.24	4.52
5	18.08	3.84
6	20.34	2.26
7	21.69	1.35
8	23.05	1.36
9	25.31	2.26

Table 4.1: Position and separation between antinodal peaks from Figure 4.8C2

For Day 3 of this imaging sequence (D3), large plaques of both fibroblasts and adipocytes were observed (Figure 4.8D). One of these plaques is highlighting by a magenta bounding box and digitally zoomed in 4.8E. The line profile shown by a green line in 4.8E is shown in Figure 4.9B1, demonstrating 7 antinodal peaks, summarised in Table 4.2. The first three fringes along this line profile measure as periodic.

# peak	Position in line profile (µm)	Spacing from previous antinode (µm)
1	9.04	N/A
2	12.43	3.39
3	15.59	3.16
4	19.21	3.62
5	26.0	6.79
6	27.80	1.80
7	30.28	2.48

Table 4.2: Position and separation between antinodal peaks from Figure 4.8F1

A second line intensity profile is shown in Figure 4.9B2. Here, 3 distinct antinodes are seen at 4.29 µm, 10.62 µm and 16.27 µm, again indicating a periodicity expected of a standing wave pattern. For both line profiles taken from the Day 3 dataset, we see a greater spacing between periodic antinodes, indicating that the topography of the cells is flatter and less curved.

Finally, for the Day 8 (D8) cells which are predominantly spherical adipocytes, the image displayed in Figure 4.8E was recorded, with a chosen ROI indicated by a cyan bounding box. This ROI is digitally zoomed in 4.8F which highlights a small cluster, and apparently stacked, of adipocyte cells. The same analysis via intensity line profiles

revealed for a chosen region 1 (indicated by a purple line in 4.8F). For this line profile (Figure 4.9C1), three distinct peaks where observed, at distances 0.90 µm, 7.91 µm and 11.07 µm along the line profile. There are not enough fringes (or perhaps fluorescent features) here to indicate periodicity. For the other chosen line profile (Figure 4.9C2) peaks are observed at 4.52 µm, 8.36 µm and 12.88 µm, indicating periodicity in this case. As with the Day 3 dataset, the measurements made from the Day 8 cells indicate a smoother topography of a less curved object.

Albeit for a handful of chosen ROIs and line profile through fringes seen by eye in the images, this analysis does suggest that the number of fringes decreases with time point into differentiation. This implies, against hypothesis, that fewer antinodal fringes are excited in adipocytes than in fibroblasts. If this were physical, it would indicate that adipocytes are flatter than fibroblasts which has been shown not to be the case in the literature, [112], [113]. Therefore, these data represents a limiting factor in standing wave imaging, that is that high curvature objects, such as stacked adipocyte cells, would result in many, closely grouped antinodal fringes which can not be detected with the 700 nm lateral resolution of the Mesolens. For topographical imaging of high curvature specimens, SW microscopy with a higher NA objective lens would be required, which would increase the lateral resolution but diminish the depth of field, meaning that depth of the specimen imaged would be compromised for detecting more antinodal fringes.

4.5.4 Live red blood cells

The axial detail observable from the fixed mammalian cells in Figure 4.6 instigated a study involving live cell specimen. As such, human erythrocytes were collected and labelled as described in Section 4.2 and imaged with SW illumination on the Mesolens. The FM4-64 membrane dye of the low-volume (10 µL for almost static imaging) red blood cell specimen was excited the 490 ± 20 nm LED. The full field image of this specimen is included in Figure 4.11(a). At this level of display zoom, it is difficult to distinguish cellular or sub-cellular detail of the small red blood cells relative to the large imaging field of the Mesolens. As such, three digitally zoomed ROIs were cropped from the full field, indicated by a yellow box in the top left of the image, a magenta

box closer to the centre of the field, and a cyan box near the bottom right of the field. These zoomed images are included in Figure 4.11(b-d). Visualising these regions in detail confirms multiple planes of excitation were seen across the individual cells, elucidating morphological detail of the cells and the areas of membrane which were in direct contact with the mirror surface. This is a confirmation that the SW mesoscopy method demonstrated here is suitable for small cells *in vitro* across a large FOV capturing 16,636 cells simultaneously (Figure 4.11(a)). To the author's understanding, this is the largest cell population imaged with SW methods reported to date.

The low-volume result prompted the following imaging experiment where a high-volume suspension (50 µL) of red blood cells was applied to the mirror surface and imaged immediately to mimic a flow cell situation with SW illumination.

Ten cells out of the population were cropped from the full time series data set and combined into a movie. The playback speed of this movie was set to 2 frames a second for the 30 second imaging intervals. From this video, cell movement and topology are clearly visible. Cells are travelling at different velocities at different regions of the mirror. As an example at the t = 210 s time point, fluorescence excited by two anti-nodal planes is visible for cells in the first, fourth and fifth rows of the movie. Beyond this time point, the illumination pattern demonstrates the changing topology of the cells as they tumble in the flow, changing axial morphology and connecting and disconnecting from the mirror surface. FM4-64 is not explicitly a photo-stable fluorophore, so the observed lack of photobleaching in this dataset originates from the axial sectioning of the SW illumination, such that only the regions of the specimen within the antinodal fringes are fluorescently excited and therefore photobleaching is restricted to half of the specimen depth. Similarly, no obvious structural changes were observed to indicate any photo-damage.

4.6 Discussion

The most important finding of the work of this Chapter are that SW imaging and TartanSW imaging can be applied at the mesoscale. The Mesolens is suitable for this despite the lower lateral resolution compared to that reported in previous studies [58],

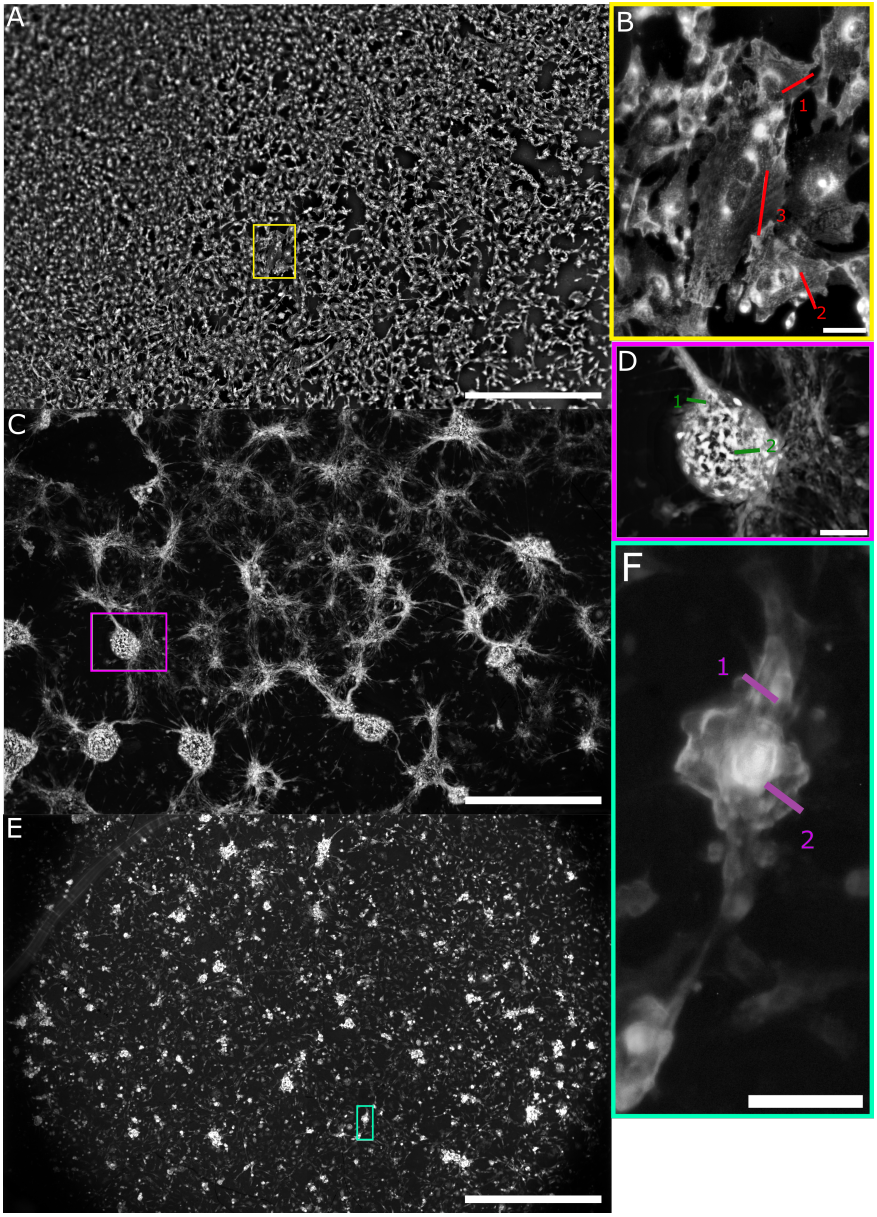

Figure 4.8: A: D0 fibroblast cells visualised with GFP tag conjugated to GLUT4 with a highlighted ROI bounded in yellow. B: ROI from A indicating three line profiles (in red) through antinodal fringes observed in fibroblasts.. C: D3 mid-differentiation cells visualised with 405 antibody conjugated to GLUT4 intracelluarly. Cells form large plaques which have axial curvature. Chosen ROI highlighted in magenta. D: Digitally zoomed ROI from C with two chosen line profiles through antinodal fringes in green. E: D8 adipocyte (mostly) cells visualised with GFP conjugated to GLUT4, ROI highlighted in cyan. F: Digitally zoomed ROI showing bundle of adipocytes with chosen line profiles shown in purple. Scale bars in full field images A, D and G: 500 µm. Scale bars in ROIs B, E and H: 50 µm.

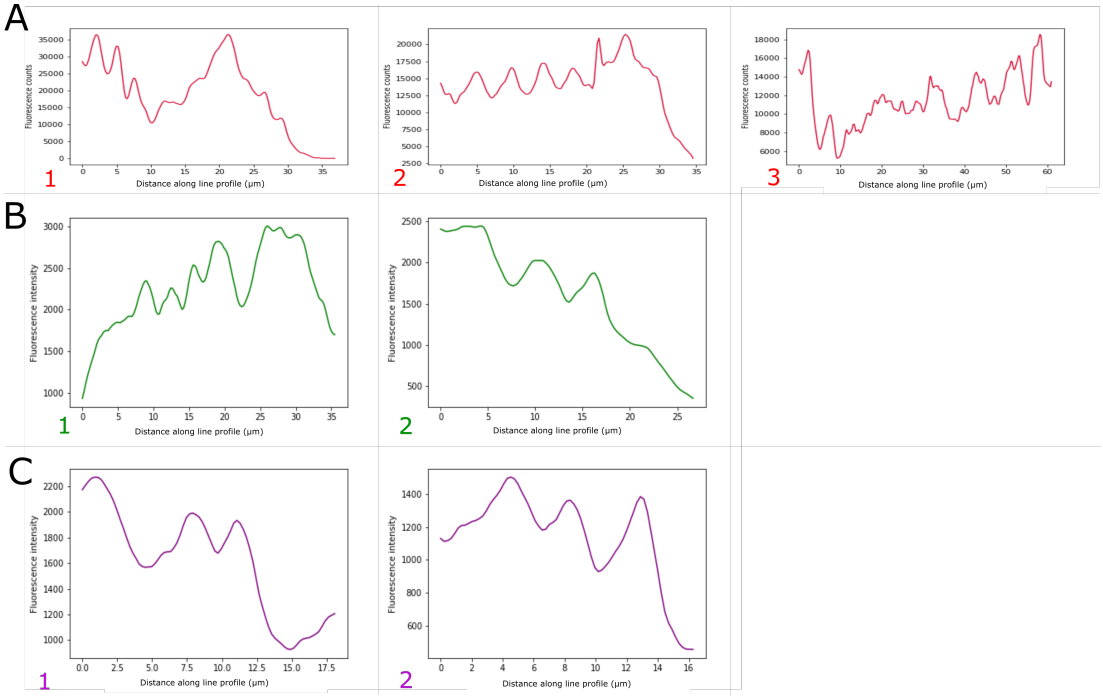

Figure 4.9: Line intensity profiles corresponding to those highlighted in Figure 4.8. A: Line profiles from D0 ROI (Figure 4.8B). B: Line profiles from D3 ROI (Figure 4.8D). C: Line profiles from D8 ROI (Figure 4.8F).

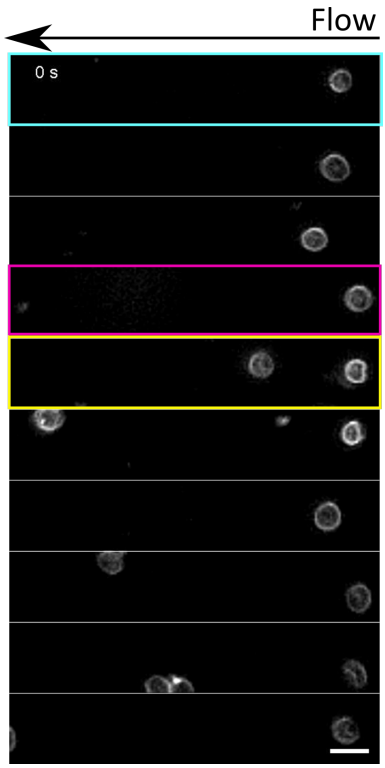

Figure 4.10: Ten red blood cells cropped from full SW illuminated Mesolens field at 30 second time intervals. Cells subject to flow conditions and tumbling and attachment and detachment of cells to mirror surfaces. Cyan, magenta and yellow bounding boxes to indicate cells discussed explicitly in text. Video published in Journal of Microscopy paper listed in Research Output on page xxiv.

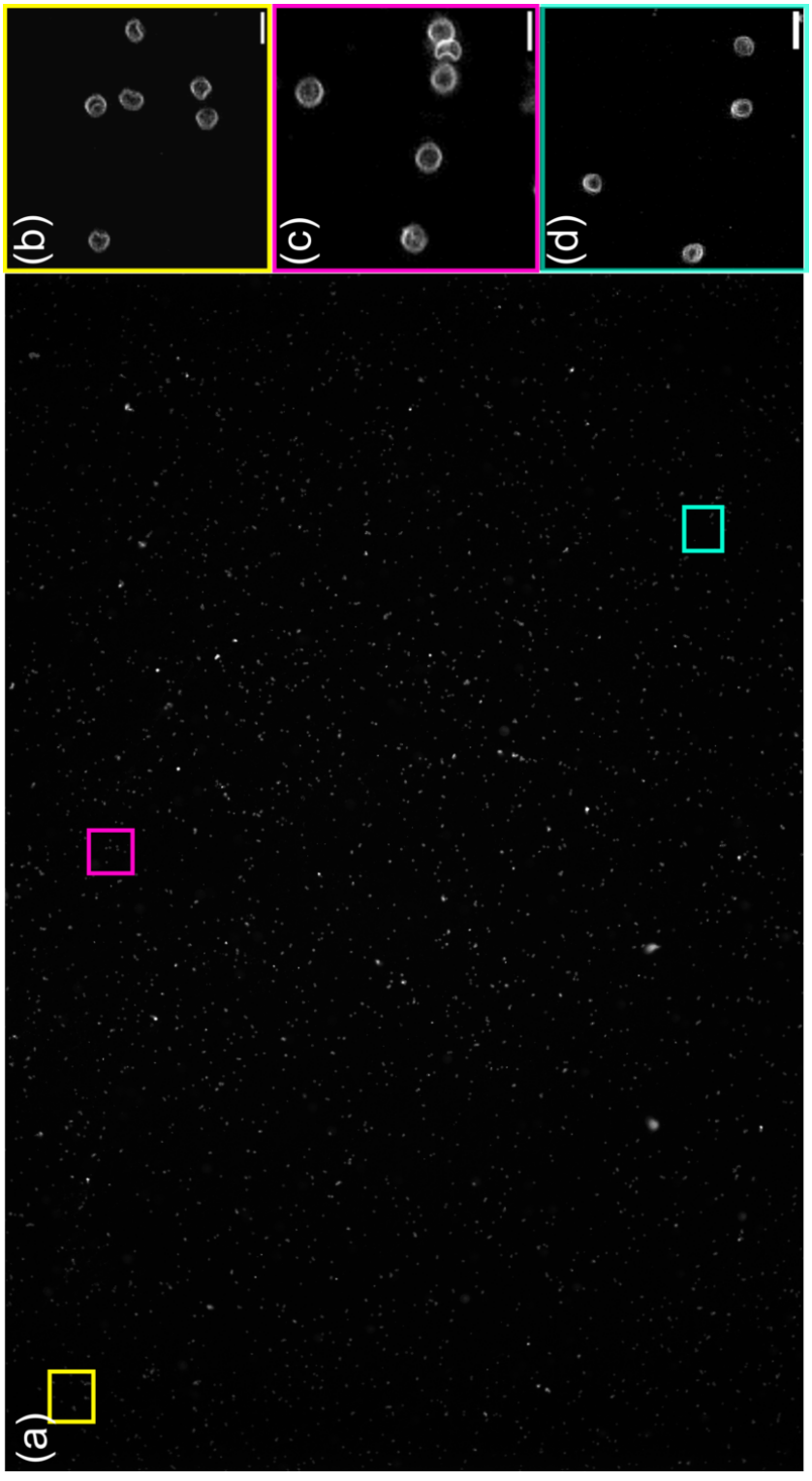

Figure 4.11: (a) Full field single colour mesoscale SW image of live red blood cells labelled for their plasma membrane with FM4-64. Scale bar = 1 mm. (b - d) Three digitally zoomed ROIs, yellow from top left of the field, magenta from centre and cyan from bottom right. Scale bars = 10 µm.

[60], [61]. The specimens imaged in this work include those imaged previously [58], [60], alongside the novel application of SW imaging of two different cell phenotypes in populations of HA-GLUT4-GFP tagged 3T3-L1s. This work has increased the FOV for SW microscopy to 4.4 mm x 3.0 mm, allowing for SW imaging of more than 16,000 cells simultaneously. While a host of biological specimens, both fixed and live, were examined within this work, we found SW mesoscopy to be more suited to some over others. As a general rule, cell types with high curvature were not suitable to be imaged with the limited depth of field across the large FOV of the Mesolens.

The Mesolens has high, sub-cellular lateral resolution such that the topographical information encoded in the lateral dimension of a 2D image can be easily resolved for a wide array of biological specimens. There are, however, further advantages of using the Mesolens over conventional low magnification objective lenses for SW imaging. The optical throughput of the Mesolens is 25-times that of a conventional 4x/0.1NA objective lens, [71]. SW illumination with low magnification, large FOV microscope objectives was attempted prior to this work but the fluorescence signal obtained from such a setup was too low to achieve a good quality image. With the work presented in this Chapter, SW illumination with the Mesolens has obviated this issue. In conjunction with the sensor shifting camera, the SW mesoscopy imaging technique described here has produced high-contrast, high-quality datasets.

From an understanding of the physics of SW illumination across the mesoscale,

the obvious advantage of SW mesocopy is the ability to study cell topology of a large population of cells from a single 2D image. A somewhat less immediately obvious benefit of this technique is speed of acquisition. The most widely used technique for volumetric imaging in cellular biology is confocal laser scanning microscopy. Confocal imaging has been a workhorse for biological imaging for decades but its pixel-wise acquisition is a fundamentally slow process, ideally suited for fixed 3D specimens. For instance, for confocal imaging with the Mesolens we note that with a 4.4 mm by 3.0 mm FOV the number of pixels required to fulfil the Nyquist sampling criterion is 19,728 pixels x 13,152 pixels. Using a minimum practical pixel dwell time of ca. 0.5 µs leads to an acquisition time of 130 s for a full FOV, full resolution scanned image, which gives only two-dimensional information from the specimen. The work presented here demonstrates that Nyquist sampled SW mesoscopy data offers insights into the third dimension, while retaining the imaging speed of a single 2D acquisition, 8 times that of confocal imaging of the same field.

A noteable limitation of the Mesolens is that the depth of field of approximately 8 µm restricts the number of antinodal planes which can be detected by the lens. Therefore, only specimens with a maximum thickness of 8 µm can be imaged with SW mesoscopy. However, to the author's knowledge, no other technique for SW illumination across a volume as large as 4.4 mm x 3.0 mm x 8 µm has been presented and the high throughput of SW mesoscopy lends itself well to diagnostic imaging in a means not achievable by high NA SW microscopy techniques presented previously.

The live red blood cell SW data, Figures 4.11 and 4.10, reveals a maximum of two antinodal planes are individual small red blood cells. This is a different view to previous studies using higher magnification, higher numerical aperture lenses that showed up to four antinodal planes [58], [60]. This reduction is due to the lower resolving power of the Mesolens relative to these high magnification, high NA lenses, there are likely to also be four antinodal planes illuminating the specimens but the 700 nm lateral resolution of the Mesolens is not able to distinguish them against the highly curved cell membrane. Resolving these features via deconvolution was attempted, but such analysis did not change the overall number of resolvable antinodal planes.

As with the original TartanSW microscopy method [61], TartanSW mesoscopy image data are not straightforward to reconstruct the 3D object structure. Unfortunately, the fluorescently stained actin cytoskeleton proved too complex to be able to reliably resolve the colour difference in antinodal planes except in the thinnest part of the cell close to the edge, so resolving adjacent structures in z with a resolution higher than a confocal microscope can provide was not feasible. There are several algorithms for multi-wavelength interferometric surface profiling, but SWs close to a reflector present a much more complex case than the single or multi-wavelength reflections used in surface profilometry [121]. As a consequence, these reconstruction algorithms cannot be easily implemented with TartanSW datasets at either the microscale or mesoscale. It would be interesting to modify phase-unwrapping methodologies previously applied to multi-wavelength images of protozoa to produce three-dimensional reconstructions of SW images [122]. As such, for complex 3D cell morphologies, particularly across the varying structures obtained in a Mesolens FOV, qualitative detail on the axial profile of the cell can be elucidated, but a robust reconstruction of the cell volume from the 2D image has yet to be realised.

The model glucose transporter cell line HA-GLUT4-GFP was imaged at various time points through differentiation from fibroblasts to adipocytes in SW mesoscopy to test the hypothesis that the spherical membrane of adipocytes would excite more antinodal fringes than the flatter filamentous fibroblast membrane. However, this imaging and analysis showed a caveat to the method which previously had only been observed on the periphery of the lens specimen images used to characterise the standing wave (as in Figure 4.5). For high curvature objects, antinodal fringes are lost to the finite depth of field of the Mesolens and are not detected in fluorescence. It is notable, however, that fluorescence intensity increases for equivalent or lower excitation parameters for cells further forward in the differentiation process. This is a somewhat expected result as fibroblasts are not glucose responsive while adipocytes are so trafficking of GLUT4 molecules to the plasma membrane is more likely in adipocyte cells. It follows that a more robust method for distinguishing between adipocyte and fibroblast morphologies in a population would be thresholding by intensity. Another technique could be using

a size filter; adipocytes aggregate while fibroblasts stack in high confluency conditions.

The preliminary study of pseudo-flow cell conditions on a high-volume of red blood cells introduces the possibility to utilise SW mesoscopy to study cell deformation and to understand the role of shear stress on cell health and regeneration [123] across tens of thousands of live cells simultaneously. To the author's knowledge, this presents a new application for SW imaging and the large FOV of the Mesolens would facilitate long-range tracking of large cell populations in three-dimensions within a single dataset. This should ideally be performed in a custom-designed flow chamber that is fabricated on top of a large, high flatness first surface reflector.

Although the Mesolens can produce full-resolution images of up to 6 mm in diameter, the FOV is limited to 4.4 mm by 3.0 mm in this study. This is because of limitations of detection, principally the chip-shifting camera. A successor to the currently installed sensor-shifting camera includes a 50 MP sensor that has a smaller pixel size and is capable of producing images of up to 427 MP (Vieworks VN-200MX). Such camera technology could potentially be applied to extend SW mesoscopy yet further to a FOV up to 6 mm in diameter. These devices use a CMOS chip that can image at up to 3 frames per second, and therefore may further increase both the detection sensitivity and imaging speed compared to the CCD-based device we have used in this work. This may be of considerable benefit for the application of SW mesoscopy to the study of cells in flow conditions.

Chapter 5

Conclusion

The work of this thesis can be split into two projects, both of which aimed to improve the axial resolution of the Mesolens below the diffraction limited value of 7 µm previously measured, [71]. The two modalities designed as a result of the work of this thesis allow the Mesolens to producre axial super-resolved images across large populations of cells, allowing for the detection of rare events in large cell numbers.

Firstly, we sought to develop a TIRF illumination modality for the Mesolens, to achieve a single optical section and an axial resolution well below the depth of field of the Mesolens using evanescent wave illumination. Due to the accessibility of the much used system and for characterisation on a system which provided much more clearance under the objective lens than the Mesolens, a prism based TIRF illuminator was built around the modified body of an upright Olympus microscope and fully characterised, Chapter 2.

In Chapter 3, the system designed in Chapter 2 was adapted, installed and demonstrated with the Mesolens, with thorough characterisation of the illuminator and image quality obtained. An improvement in SBR of more than 5 fold was measured, more fine structure was observed than with widefield epifluorescence, and high uniformity across the 4.4 mm x 3.0 mm FOV was maintained.

The second project, described in Chapter 4, utilised a periodic interference pattern in order to bypass the axial diffraction limit of the Mesolens. The structure of a standing wave yields topographical information from the antinodal planes from a single

2D acquisition. By extending this illumination method across the 4.4 mm x 3.0 mm FOV of the Mesolens, we were able to demonstrate our fast 3D imaging technique across more than 100 fixed fibroblast cells and more than 16,000 live red blood cells. We also laid the groundwork for future SW mesoscopy work to screen for blood disorders, with a custom flow chamber system with a reflective substrate.

Future work based on both of the projects lie in both further developments to the optics of the systems described and for biological applications of the illuminators themselves. In turn, I will outline some areas for future study for the work presented in each Chapter of this thesis.

For the TIRF prototype development and ultimately irreproducible method for measuring evanescent field depth proposed in Chapter 2, an area for further study could be in using different dyes to coat the lens specimen. The main limiting aspect of the resulted presented here was that the illumination bleached the region of the lens specimen in contact with the prism surface and as such, did not produce statistically meaningful values for evanescent field depth. This was an unexpected result given the properties of the Atto-NHS ester dyes used and their published photostability. Perhaps using dyes with different chemical profiles, such as photoswitchable fluorophores whose fluorescence emission could be managed more robustly than with continual excitation of a non-reversible fluorophore. Furthermore, novel developments in 3D printing of optical lenses [124] could allow for quick, scalable, cost efficient manufacture of lenses for the purpose of this evanescent depth measurement, allowing for discarding of samples following deterioration while acquiring multiple datasets for statistical measurement.

For the demonstrated MesoTIRF modality in Chapter 3, there is a large range of applications for this illuminator. From a hardware perspective, additional excitation filters to the custom filters currently in place in the Mesolens detection path would allow for further wavelengths and fluorophores to be utilised in MesoTIRF. As the system is build around a tunable TiSapphire pumped OPO unit (offering wavelengths of 360 nm - 4000 nm) and every optic in the external MesoTIRF system has an anti-reflection coating between 350 nm and 700 nm, only minimal realignment of the modality would be required for additional wavelengths. MesoTIRF acquisition is currently limited to

0.2 Hz by the camera technology but updating this system to faster commercially available sensors would allow for MesoTIRF imaging of fast, dynamic processes such as fast-acting antimicrobial peptides or imaging of calcium transients in the plasma membrane. Furthermore, developing an environmental chamber that is compatible with the Mesolens would allow for high resolution membrane imaging at physiological temperatures for mammalian specimens, for such applications as high content drug screening or wound healing models [102].

Several exciting further super-resolution extensions to the MesoTIRF modality would potentially allow for single molecule imaging across populations of cells. Developing a SIM illuminator coupled into the MesoTIRF path, while very much a non-trivial undertaking which would require vast computational effort or a large scale, custom made spatial light modulator with sufficiently high pixel number, would allow for a two-fold lateral resolution enhancement. As TIRF is the illumination modality for all SMLM, an intriguing project would be to perform, for example, DNA-PAINT on the Mesolens using the MesoTIRF illuminator. However, the comparatively low NA (and associated lateral resolution) of the Mesolens are currently bottlenecks to this endeavour. However, a potential means of sidestepping this issue is utilising computational algorithms such as Super-Resolution Radial Fluctuation (SRRF) algorithms [125] which use the natural fluctuations of a non photoswitchable fluorophore to mimic SMLM blinking, which is currently under investigation in the Centre for Biophotonics, University of Strathclyde.

For the second modality developed as a result of this work, future work in development and application of the SW mesoscopy mode could be extending the applications shown here. One of the limiting aspects of SW mesoscopy shown and discussed here is the 7 µm depth of field of the Mesolens, which restricts the number of antinodal fringes which are detected. It could be possible to use SW mesoscopy as a way of screening rare events or structures across a specimen and then correlating with SW microscopy in the regions of interest detected on the Mesolens. In reference to work shown here, this would be particularly interesting for the case of the GLUT4 imaging where cell segmentation on SW mesoscopy data for identifying regions of interest in 3D and then

imaging these areas with a high NA objective lens to elucidate more antinodal fringes.

Here, preliminary data of pseudo flow cell dynamics of more than 16,000 red blood cells was shown. By manufacturing flow chambers with a reflective base substrate, SW mesoscopy could allow for high throughput screening of various blood disorders and diseases, such as anemia, parasitaemia and other diseases of the blood including hereditary spherocytosis, sickle cell disease, hereditary stomatocytosis or elliptocytosis.

Similar to MesoTIRF, the applications of SW mesoscopy could be extended greatly given updates to the camera technology to allow for faster acquisition and design of a custom environmental chamber for imaging under physiological conditions. One example of an application which would greatly benefit from faster, physiological SW mesoscopy is that of cell motility and signalling across cell populations, in both mammalian and microbiological cell specimens.

Appendix A

TIRF prototype characterisation Python codes

A.0.1 Evanscent depth from lens specimen images, Python code #1

```
## PACKAGES
import numpy as np
import os
import pandas
import matplotlib.pyplot as plt
import math
from scipy.interpolate import UnivariateSpline
from scipy.optimize import curve_fit

filepath = 'I:\Science\SIPBS\McConnellG\Shannan Foylan\Analysis for TIRF
    paper\100320_72mmLensImaging\CroppedImages4Deconv\LineProfiles\'

os.chdir(filepath)

## VARIABLE PARAMETERS###################
theta = [48, 52, 55, 58, 62, 65, 72]
l = 532e-9
```

```
f = 72e-3
Rq = 37.22 # radius of curvature in mm (quoted) (for EO 30mm f -> 15.5mm R,
    48mm f -> 24.81mm R, 72mm f -> 37.22mm R)
R = Rq*(1e-3) #radius of curvature in m
errR = 0.01 * f
pm = 1.532 # pixels per micron

ni = 1.52
nt = 1
########################################

D = []
Dnm = []
eD = []
err_resid = []

# READ IN FILE AND PLOT (IN UM)

def Gaussian(x, a, x0, sigma) :
    return a*np.exp(-(x-x0)**2/(2*sigma**2))

for i in range(0, len(theta)) :
    #pathname containing data
    file = str(theta[i]) + '.csv'

    data = pandas.read_csv(file)
    print('Data set: ', file, 'stored in:', filepath)

    values = data.values

    Dpx = values[:,0] #distance values in pixels
    Dum = Dpx/pm #converting distance to micron
    Igv = values[:,1] #gray value intensities
    Inorm = Igv/max(Igv)
```

```
plt.plot(Dum, Inorm, label = 'Normalised raw data')
plt.xlabel('Distance (\u03bcm)')
plt.ylabel('Gray value intensity')

#estimate mean and standard deviation
mean = np.mean(Inorm)
sigma = np.std(Inorm)/len(Inorm)

#fit Gaussian
popt, pcov = curve_fit(Gaussian, Dum, Inorm, method = 'lm')

#goodness of fit
residuals = Inorm - Gaussian(Dum, *popt)
ss_res = np.sum(residuals**2) #residual sum of squares
rms = math.sqrt(ss_res/len(Inorm))

ss_tot = np.sum(Inorm-mean**2) #total sum of squares
r_squared = 1 - (ss_res/ss_tot)

plt.plot(Dum, Gaussian(Dum, *popt), label = 'Gaussian fit, R^2 =
    {:.4f}'.format(r_squared))
plt.legend(loc = 1)


#find roots @ HM
splineFWHM = UnivariateSpline(Dum, Gaussian(Dum,
    *popt)-np.max(Gaussian(Dum, *popt))/2, s = 0) #calculate FWHM from
    spline function
r1, r2 = splineFWHM.roots() #find roots of function (co-ords of both FWHM
    points)

#find FWHM
FWHM = r2 - r1 #subtract roots from each other to find FWHM
```

```
    print("FWHM diameter: {:3f}".format(FWHM),'\u03bcm') #print answer

    #show on plot
    plt.axvspan(r1, r2, facecolor='b', alpha=0.5)
    plt.show() #plot profile with FWHM measurement shown

    #half to find radius of spot
    r = FWHM/2*(1e-6) #radius of spot in m

    d = -math.sqrt((R**2)-(r**2)) + R # calculate depth by lens geometry (in
        m)
    D.append(d)
    dnm = d*(1e9)
    Dnm.append(dnm)

    #uncertainty...
    err_d = math.sqrt(((errR)**2) + ((rms)**2)) #error from quadrature of
        interpolated r and quoted lens centre thickness tolerance
    eD.append(err_d)


#plt.plot(theta, Dnm, 'x-', color = 'magenta', label = "Measured from {:.2f}
    mm RoC lens specimen".format(Rq))
plt.errorbar(theta, Dnm, eD, xerr = None, marker = 's', mfc='red',
        mec='blueviolet', linewidth = 3, ms=2, mew=4, label = "Measured from
            {:.2f} mm RoC lens specimen".format(Rq) )
plt.xlabel('Incidence angle (\N{DEGREE SIGN})')
plt.ylabel('Depth (nm)')

d_theo = []
for i in theta:
    d_t =
        1/((4*math.pi)*((ni**2*(math.sin(math.radians(i)))**2)-nt**2)**(0.5))*(1e9)
    d_theo.append(d_t)
```

```
plt.plot(theta, d_theo, 'o-', color = 'coral', label = 'Theoretical
    calculation')
plt.legend(loc = 1)
filename = filepath + '\DepthVsIncAngle_{:.2f}mmDataSet_raw.png'.format(Rq)
plt.savefig(filename)
plt.show()
```

A.0.2 Evanscent depth from lens specimen images, Python code #2

```
import numpy as np
import matplotlib.pyplot as plt
import skimage.io as io

import datetime
from tkinter.filedialog import askdirectory
import math
from scipy.interpolate import UnivariateSpline
from scipy.optimize import curve_fit
from scipy.ndimage import gaussian_filter
# import math

## VARIABLE PARAMETERS###################

theta = [63.6, 65.8, 68.6, 70.2, 72.0, 74.6]

T = [22.23, 23.64, 21.03, 22.25, 22.45, 22.23, 22.0, 22.1, 22.63, 22.62,
    22.59] #error in measurement of lens spot @ top surface of prism

errTheta = np.std(T)

l = 532e-9 # wavelength of light
```

```
f = 72e-3 # focal length in m
Rq =  37.22 # radius of curvature in mm (quoted) (for EO 30mm f -> 15.5mm R,
    48mm f -> 24.81mm R, 72mm f -> 37.22mm R)
R = Rq*(1e-3) #radius of curvature in m
errR = 0.01 * f # error on radius of curvature
#R = 7.5e-3
#errR = 0.1e-3
pm = 0.61 # pixels per micron

ni = 1.52 # refractive index of prism
nt = 1 # n of air

N = 500 #number of iterations
blur_sigma = 3

current_date_time = datetime.datetime.now()
dt_string = current_date_time.strftime('%d%m%y')
print ("The date is:" , dt_string) #get a date string for save files

#change to appropriate filename
filestring1 = '/100mWTIR_centreFOV4X_'
filestring2 = 'degInc_1sEt_bgrCorr_cropped.tif' #beginning of file name
#filestring3 = '1_TIR.tif'#end of file name
savefilename = '/DepthPlot{:.2f}RoCmmLens_varyingTheta_4X_'.format(Rq) +
    dt_string + '.png' #save file name

# empty arrays to append into
Dnm = [] #depth in nm from fitting
eD = [] #error on depth
d_theo = []#theoretical depth
d_int = []#depth from interpolation


###################################
```

```
#DEFINITIONS
# annulus code to get binary mask, written by Nicholas Hall
#
    https://github.com/MicronOxford/microscope-aotools/blob/master/microAO/aoMetrics.py
def make_OTF_mask(size, inner_rad, outer_rad):
    rad_y = int(size[0] / 2)
    rad_x = int(size[1] / 2)

    outer_mask = np.sqrt((np.arange(-rad_y, rad_y) ** 2).reshape((rad_y * 2,
        1)) +
                         np.arange(-rad_x, rad_x) ** 2) < outer_rad

    inner_mask_neg = np.sqrt((np.arange(-rad_y, rad_y) ** 2).reshape((rad_y *
        2, 1)) +
                         np.arange(-rad_x, rad_x) ** 2) < inner_rad
    inner_mask = (inner_mask_neg - 1) * -1
    ring_mask = outer_mask * inner_mask
    return ring_mask


#Gaussian definition for fitting
def Gaussian(x, a, x0, sigma) :
    return a*np.exp(-(x-x0)**2/(2*sigma**2))

########################

#open folder to choose file

path = askdirectory(title='Select Folder')
print(path)

#iterate for incidence angle

for i in range(0, len(theta)) :
```

```
#    for it in range(1, 5) :
    idata = path + filestring1 + str(theta[i]) + filestring2 #+ str(it) +
        filestring3
    #print(idata)#define + display file name with iteration
    savepath = path + '\Analysis__48mm_varTheta'
    savefile_iter = str(theta[i]) + '_rExtractionPlots.png'
    #read in image, get image size, specify radius values
    fig = plt.figure(figsize = (10, 10))
    ax = fig.add_subplot(221)
    image1 = io.imread(idata)

    ax.set_title('Raw image: ${\\theta}$ =' + str(theta[i]))
    ax.imshow(image1)#display raw data

    image_bl = gaussian_filter(image1, sigma = blur_sigma)
    ax2 = fig.add_subplot(222)
    ax2.set_title('Gaussian blurred image, sigma =' + str(blur_sigma))
    ax2.imshow(image_bl)

    #image needs to have an even # of pix for annuli def

    if image_bl.shape[0] % 2 == 1 :
        image_bl = image_bl[0:-1]
    if image_bl.shape[1] % 2 == 1 :
        image_bl = image_bl[:, 0:-1]#
    else :
        image_bl = image_bl

    isize = image_bl.shape

    #diameter of thresholded image = max outer radius for make_OTF_mask def
    max_outer_rad = isize[0]/2 #math.sqrt(np.sum(binary)/math.pi)
    orlist = np.linspace(2, max_outer_rad, N)#array for outer radius for
        binary mask
```

```
r = np.linspace(0, max_outer_rad, N)#full radius of image array
aI = []#empty intensity array to append into
sI = []#empty std on intensity array

#iteratively increase size of annulus using binary mask to work out
    intensity
for outer_rad in orlist :

    m = make_OTF_mask(isize, 1, outer_rad) #generate binary mask
    n_m = np.count_nonzero(m)#count pixels in mask
    masked_image = m*image_bl #mask image

    I_M = masked_image[masked_image != 0] #cut out not zero elements

    avgI = np.sum(I_M)/n_m #find average intensity for this annulus
    aI.append(avgI)

    sigI = math.sqrt((1/n_m)*np.sum((I_M-avgI)**2))#find std weighted
        across pixels
    sI.append(sigI)

normI = aI/max(aI) #normalise intensity

ax3 = fig.add_subplot(223)
ax3.set_title('Radial pixel intensity')
ax3.set_xlabel('Radial distance (px)')
ax3.set_ylabel('Intensity (px)')
ax3.plot(r, aI)#display intensity data extracted from image

#fit Gaussian
popt, pcov = curve_fit(Gaussian, r, normI, method = 'lm')

#goodness of fit
residuals = normI - Gaussian(r, *popt)
```

```
ss_res = np.sum(residuals**2) #residual sum of squares
rms = math.sqrt(ss_res/len(normI))#rms error

mean = np.mean(normI)
sigma = np.std(normI)

ss_tot = np.sum(normI-mean**2) #total sum of squares
r_squared = 1 - (ss_res/ss_tot)

#find root @ HM
splineFWHM = UnivariateSpline(r, Gaussian(r, *popt)-np.max(Gaussian(r,
    *popt))/2, s = 0) #calculate FWHM from spline function
r1 = splineFWHM.roots() #find root of function @ HM point
if len(r1) == 2 :
    r1_um = (r1[1] - r1[0])/pm * (1e-6)
else :
    r1_um = r1/pm * (1e-6) #convert to um (and then m)
dnm = (R - math.sqrt(R**2 - r1_um**2)) * (1e9) #geometrically find depth
    in nm
Dnm.append(dnm)

ax4 = fig.add_subplot(224)
ax4.plot(r/pm, normI, label = 'Data')
ax4.plot(r/pm, Gaussian(r, *popt), label = 'Gaussian fit, R^2 =
    {:.4f}'.format(r_squared))
ax4.axhline(y = np.max(normI)/2 , color='r', linestyle='--', label =
    'FWHM')
ax4.set_xlabel('Radial distance (\u03bcm))')
ax4.set_ylabel('Normalised intensity')
ax4.legend(loc = 1)#display Gaussian fit to data and HM point
# fig.savefig(savepath + savefile_iter)

yHMidx = np.argwhere(normI < max(normI)/2)#interpolate to find HM
rHM = r[yHMidx[0]]/pm *(1e-6)#convert to um (and then m)
```

```
    d = (R - math.sqrt(R**2 - rHM**2)) * (1e9) #geometrically find depth in nm
    d_int.append(d)

    err_d = math.sqrt((errR**2) + (np.std(rms))**2) #error from quadrature of
        interpolated r and quoted lens centre thickness tolerance
    eD.append(err_d)

    print('Depth measured (fit) for inc. angle =', str(theta[i]), ':', dnm,
        '+/-', err_d , 'nm')
    print('Depth measured (interp) for inc. angle =', str(theta[i]), ':', d,
        '+/-', err_d , 'nm')

#plot depth for varying incidence angle + compare with theory
fig2 = plt.figure(figsize = (10, 10))
ax5 = fig2.add_subplot(221)
ax5.errorbar(theta, Dnm, eD, xerr = errTheta, marker = 's', mfc='blue', label
    = 'Measured w fit')
ax5.errorbar(theta, d_int, eD, xerr = None, marker = 's', label = 'Measured w
    interpolation')

for th in theta: #theoretical depth for experimental parameters
    d_t = (l)/(4*math.pi*(ni**2*math.sin(math.radians(th))**2-nt**2)**0.5)
    d_t = d_t * (1e9)
    d_theo.append(d_t)

ax5.plot(theta, d_theo, 'o-', color = 'coral', label = 'Theoretical')
ax5.legend(loc = 1)
ax5.set_xlabel('Incidence angle (\N{DEGREE SIGN})')
ax5.set_ylabel('Depth of field (nm)') #plot depth measured, theo depth
    against incidence angle

fig2.savefig(path + savefilename)
```

A.0.3 Fitting to evanescent power data with incidence angle dependence

```
## load in power versus incidence angle measurements ##
#find max and min incidence angles to define fit window and domain
tmin, tmax = min(theta), max(theta)
#convert data into logarithmic scale
x, y = np.log(theta),np.log(avg_Power)
#least squares fit a linear function to the logarithmic data,
#good fit indicates exponential fit in raw data
pfit, stat = PN.fit(x, y, 1, full = True, window = (tmin, tmax))
#confine domain of fit to angle data
domain=(tmin, tmax)

#spit out fit results
print('Raw fit results:', pfit, stat, sep='\n')
P0, m = pfit
resid, rank, sing_val, rcond = stat
rms = np.sqrt(resid[0]/len(avg_Power))
ss_res = np.sum(resid**2)
ss_tot = np.sum(y - np.mean(y)**2)
R_sq = 1 - (ss_res/ss_tot)
print('Fit for {:1f}'.format(Pi[i]),': P = {:.3f}t + {:.3f}'.format(m,
    P0),'(rms residual = {:.4f})'.format(rms))


#add in confidence bounds to classify confidence in data fit


#define confidence interval
ci = st.t.interval(alpha=0.97, df=len(pfit(x))-1, loc=np.mean(pfit(x)),
    scale=st.sem(pfit(x)))
cil = np.log(ci)
```

A.0.4 Focal adhesion detection for MesoTIRF chapter

```
#%% relevent libraries
import pandas as pd
import numpy as np
import matplotlib.pyplot as plt
import os
#from scipy.signal import find_peaks

#%% file path, load file
file_path = 'I:\\Science\\SIPBS\\McConnellG\\Shannan Foylan\\Mesolens
    imaging\\Focal adhesion Proof of Principle MesoTIRF
    imaging\\091221_fixedcells_paxillin\\3t3_r3_analysis\\'
os.chdir(file_path)

filename = 'Neighbouring focal adhesions r3.xlsx'

data = pd.read_excel(filename)

#%% variables
px_um = 4.425 #pixel to micron conversion
CB = 0.5 #'confidence bound', the normalised intensity value chosen to be
    minimum focal adhesion signal

v1 = 1
v2 = 7
v3 = 13
v4 = 19
v5 = 25 #column locations in excel file for n-th ROI data

V = [v1, v2, v3, v4, v5]
c = 1 #counter
epiC = []
```

```
TIRFC = []
IC = []
#%% loop over all 5 line profiles
for v in V :

    e1p = data.iloc[:,v]
    e1I = data.iloc[:,v+1] #read in line profile data for epi illuminated
        images
    T1p = data.iloc[:,v+3]
    T1I = data.iloc[:,v+4] #read in line profile data for TIRF illuminated
        images

    a = [e1p, e1I, T1p, T1I]
    b = []
    for i in a :
        i = i[~pd.isnull(i)]
        b.append(i)

    e1p = b[0]# * px_um
    e1I = b[1]
    T1p = b[2] #* px_um
    T1I = b[3] #remove NaN values

    normE1 = e1I/max(e1I) #normalise by maximum epi intensity count
    normT1 = T1I/max(T1I) #normalise by maximum TIRF intensity count

    Ce = np.var(e1I)/np.mean(e1I)
    epiC.append(Ce)
    print('Epi contrast for ROI ' + str(c) + ' = ' + str(Ce))
    CT = np.var(T1I)/np.mean(T1I)
    TIRFC.append(CT)
    print('TIRF contrast for ROI ' + str(c) + ' = ' + str(CT))

    C_improve = CT/Ce
```

```
IC.append(C_improve)

print('Contrast improvement ratio TIRF/epi = ' + str(C_improve) + ' (ROI
    ' + str(c) +')')

fig = plt.figure()# create figure object
ax = fig.add_subplot(111)
ax.plot(e1p, normE1, 'coral', label = 'Epi')
ax.plot(T1p, normT1, 'cyan', label = 'TIRF')
ax.set_xlabel('Position along line profile (px)')
ax.set_ylabel('Normalised fluorescent intensity, In')
ax.legend(loc='upper left', frameon=False)



normE0 = normE1 - min(normE1)
normT0 = normT1 - min(normT1) #remove noise floor

idx_e = normE0.where(normE0>CB)
idx_t = normT0.where(normT0>CB)

# savefig1name = 'Raw line profile data for ROI' + str(c) + '_poster' +
    '.png'
# fig.savefig(file_path + savefig1name)

fig2 = plt.figure()
ax2 = fig2.add_subplot(211)
ax2.plot(e1p, normE0, 'coral', label = 'Epi')
ax2.plot(e1p, idx_e, 'indigo', label = 'Focal adhesion > CB')
ax2.set_ylabel('In - noise floor')
ax2.legend(loc='upper left', frameon=False)

ax3 = fig2.add_subplot(212)
ax3.plot(T1p, normT0, 'cyan', label = 'TIRF')
```

```
    ax3.plot(T1p, idx_t, 'indigo', label = 'Focal adhesion > CB')
    ax3.legend(loc='upper left', frameon=False)

    plt.ylabel('In - noise floor')
    plt.xlabel('Position along line profile (px)')

    savefig2name = 'Accepted FA in epi and TIRF data for ROI' + str(c) +
        'poster' + '.png'
    fig2.savefig(file_path + savefig2name)

    c = c + 1

avgSNRe = np.mean(epiSNR)
avgSNRT = np.mean(TIRFSNR)
avg_improvement = np.mean(IC)

SNR = {'Avg Epi SNR':[avgSNRe], 'Avg TIRF SNR':[avgSNRT], 'Improvement
    ratio':[avg_improvement]}
avSNR = pd.DataFrame(data = SNR)

avgSNRsavefile = 'AveragedSNR_5ROIS.csv'
avSNR.to_csv(avgSNRsavefile)
```

Following Python code written by Nicholas Hall utilised for evanescent depth characterisation in this thesis, obtained from Github: (https://github.com/MicronOxford/microscope-aotools/blob/master/microAO/aoMetrics.py).

```
    #!/usr/bin/env python
# -*- coding: utf-8 -*-

## Copyright (C) 2018 Nicholas Hall <nicholas.hall@dtc.ox.ac.uk>
##
## microAO is free software: you can redistribute it and/or modify
## it under the terms of the GNU General Public License as published by
```

```
## the Free Software Foundation, either version 3 of the License, or
## (at your option) any later version.
##
## microAO is distributed in the hope that it will be useful,
## but WITHOUT ANY WARRANTY; without even the implied warranty of
## MERCHANTABILITY or FITNESS FOR A PARTICULAR PURPOSE. See the
## GNU General Public License for more details.
##
## You should have received a copy of the GNU General Public License
## along with microAO. If not, see <http://www.gnu.org/licenses/>.

#Import required packs
import numpy as np
from scipy.signal import tukey
from skimage.filters import threshold_otsu

def make_OTF_mask(size, inner_rad, outer_rad):
    rad_y = int(size[0] / 2)
    rad_x = int(size[1] / 2)

    outer_mask = np.sqrt((np.arange(-rad_y, rad_y) ** 2).reshape((rad_y * 2,
        1)) +
                         np.arange(-rad_x, rad_x) ** 2) < outer_rad

    inner_mask_neg = np.sqrt((np.arange(-rad_y, rad_y) ** 2).reshape((rad_y *
        2, 1)) +
                         np.arange(-rad_x, rad_x) ** 2) < inner_rad
    inner_mask = (inner_mask_neg - 1) * -1
    ring_mask = outer_mask * inner_mask
    return ring_mask
```

Appendix B

Media recipes

Luria-Bertani (Miller)/Lysogeny Broth (LB) Medium

For *E. coli* cultures.

Tryptone	10.0 g
Yeast extract	5.0 g
NaCl	10.0 g
Agar	20.0 g
dH_2O	1000 mL

Weigh out dry reagents, dissolve in 950 mL dH_2O, add in liquid reagents, mix and autoclave.

Supplemented DMEM

For 3T3-L1, HeLa and HEK293 cell lines.

Dulbeccos Modified Eagle's Medium (11500596, Gibco)	500 mL
Heat inactivated Fetal Bovine Serum (10500064, Gibco)	50 mL
Penicillin Streptomycin (P4458-100ML, Merck)	5 mL
L-Glutamine (392-0441, VWR)	5 mL
Sodium Pyravuate (11360-070-100ML, Gibco)	5 mL
HEPES buffer (14175-095, Gibco)	1 mL

Supplemented RPMI-1640

For MeT-5A cell line.

RPMI-1640 Medium (15-040-CV, Scientific Laboratory Supplies)	500 mL
Heat inactivated Fetal Bovine Serum (10500064, Gibco)	50 mL
Penicillin Streptomycin (P4458-100ML, Merck)	5 mL
L-Glutamine (392-0441, VWR)	5 mL
Sodium Pyravuate (11360-070-100ML, Gibco)	5 mL
HEPES buffer (14175-095, Gibco)	1 mL

Bibliography

[1] Z. Janssen, J. W. Kepler Michael Davidson, and M. Zacharias Janssen, "Pioneers in Optics: Zacharias Janssen and Johannes Kepler," *Microscopy Today*, vol. 17, pp. 44–47, 11 2009.

[2] R. Hooke, *Micrographia: or some Physiological Descriptions of Minute Bodies made byMagnifying Glasses with Observations and Inquiries thereupon.* 1665.

[3] F. J. Cole, "The Collected Letters of Antoni van Leeuwenhoek," *Nature*, vol. 163, pp. 192–193, 2 1949.

[4] K. Carlsson and N. Åslund, "Confocal imaging for 3D digital microscopy," *Applied Optics*, vol. 26, pp. 3232–3238, 8 1987.

[5] W. B. Amos, J. G. White, and M. Fordham, "Use of confocal imaging in the study of biological structures," *Applied Optics*, vol. 26, p. 3239, 8 1987.

[6] A. Diaspro, P. Bianchini, F. Cella Zanacchi, and C. Usai, "Two-Photon Excitation Fluorescence Microscopy," in *Encyclopedia of Biophysics*, pp. 2667–2671, Berlin, Heidelberg: Springer Berlin Heidelberg, 2013.

[7] W. Denk, J. Strickler, and W. Webb, "Three-Dimensional Optical Storage Memory," *Science*, vol. 245, pp. 843–845, 4 1990.

[8] P. F. Curley, A. I. Ferguson, J. G. White, and W. B. Amos, "Application of a femtosecond self-sustaining mode-locked Ti:sapphire laser to the field of laser scanning confocal microscopy," *Optical and Quantum Electronics*, vol. 24, pp. 851–859, 8 1992.

[9] W. Kukulski, M. Schorb, S. Welsch, A. Picco, M. Kaksonen, and J. A. Briggs, "Correlated fluorescence and 3D electron microscopy with high sensitivity and spatial precision," *Journal of Cell Biology*, vol. 192, pp. 111–119, 1 2011.

[10] "Fluorophores," in *Principles of Fluorescence Spectroscopy* (J. R. Lakowicz, ed.), pp. 63–95, Boston, MA: Springer US, 2006.

[11] M. W. Davidson and M. Abramowitz, "Optical Microscopy," in *Encyclopedia of Imaging Science and Technology*, American Cancer Society, 2002.

[12] M. Born, *Principles of optics : electromagnetic theory of propagation, interference and diffraction of light.* 5th rev.ed ed., 1975.

[13] Geoffrey Brooker, *Modern Classical Optics.* Oxford University Press, 2003.

[14] J. W. Goodman, *Introduction to Fourier optics.* McGraw-Hill physical and quantum electronics series, San Francisco: McGraw-Hill, 1968.

[15] H. E. Keller, "Objective Lenses for Confocal Microscopy," in *Handbook Of Biological Confocal Microscopy*, pp. 145–161, Boston, MA: Springer US, 2006.

[16] John J. Cargille, "Immersion Oil and The Microscope," *New York Microscopical Society Yearbook*, pp. 1–6, 1964.

[17] W. J. Smith, "Image Formation: Geometrical and Physical Optics," in *Handbook of Optics* (Driscoll W. G. and Vaughan W., eds.), vol. 1, ch. 2, pp. 1–16, McGraw-Hill, 1978.

[18] S. Inoué, "Foundations of confocal scanned imaging in light microscopy," *Handbook of Biological Confocal Microscopy: Third Edition*, pp. 1–19, 2006.

[19] C. M. Sparrow, "On Spectroscopic Resolving Power," *ApJ*, vol. 44, no. 2455, p. 76, 1916.

[20] S. Kurinec, "Complementary Metal Oxide Semiconductor Field Effect Transistors," in *Encyclopedia of Materials: Science and Technology*, pp. 1343–1350, Elsevier, 2001.

[21] R. Hui, "Photodetectors," in *Introduction to Fiber-Optic Communications*, pp. 125–154, Elsevier, 2020.

[22] J. B. Pawley, "Points, pixels, and gray levels: Digitizing image data," *Handbook of Biological Confocal Microscopy: Third Edition*, pp. 59–79, 2006.

[23] S. Herbert, H. Soares, C. Zimmer, and R. Henriques, "Single-Molecule Localization Super-Resolution Microscopy: Deeper and Faster," *Microscopy and Microanalysis*, vol. 18, pp. 1419–1429, 12 2012.

[24] J. Pawley, "Fundamental Limits in Confocal Microscopy," *Handbook of Biological Confocal Microscopy*, pp. 19–37, 1995.

[25] M. G. L. Gustafsson, "Surpassing the lateral resolution limit by a factor of two using structured illumination microscopy," *Journal of Microscopy*, vol. 198, pp. 82–87, 5 2000.

[26] B. Bailey, D. L. Farkas, D. L. Taylor, and F. Lanni, "Enhancement of axial resolution in fluorescence microscopy by standing-wave excitation," *Nature 1993 366:6450*, vol. 366, no. 6450, pp. 44–48, 1993.

[27] F. Zernike, "How I Discovered Phase Contrast," *Science*, vol. 121, pp. 345–349, 1955.

[28] O. Heimstädt, "The fluorescence microscope (Das Fluoreszenzmikroskop)," *Zeitschrift für wissenschaftliche Mikroskopie und mikroskopische Technik*, vol. 28, pp. 330–337, 1911.

[29] P. T. C. So, H. Kim, and I. E. Kochevar, "Two-photon deep tissue ex vivo imaging of mouse dermal and subcutaneous structures," *Optics Express*, vol. 3, pp. 339–350, 10 1998.

[30] N. B. Vicente, J. E. D. Zamboni, J. F. Adur, E. V. Paravani, and V. H. Casco, "Photobleaching correction in fluorescence microscopy images," *Journal of Physics: Conference Series*, vol. 90, p. 12068, 11 2007.

[31] S. Inoué, "Foundations of Confocal Scanned Imaging in Light Microscopy," *Handbook of Biological Confocal Microscopy*, pp. 1–17, 1995.

[32] M. Minsky, "Memoir on inventing the confocal scanning microscope," *Scanning*, vol. 10, pp. 128–138, 1 1988.

[33] G. v. Meer, E. H. Stelzer, R. W. Wijnaendts-van Resandt, and K. Simons, "Sorting of sphingolipids in epithelial (Madin-Darby canine kidney) cells.," *The Journal of Cell Biology*, vol. 105, pp. 1623–1635, 10 1987.

[34] G. McConnell, W. Amos, and T. Wilson, "Confocal microscopy," in *Handbook of Comprehensive Biophysics*, 2011.

[35] G. S. Kino and T. R. Corle, "Confocal {Scanning} {Optical} {Microscopy}," p. 9, 1989.

[36] D. Axelrod, "Evanescent Excitation and Emission," in *Fluorescence Microscopy*, pp. 1–14, Elsevier, 2014.

[37] M. Martin-Fernandez, C. Tynan, and S. Webb, "A 'pocket guide' to total internal reflection fluorescence," *Journal of Microscopy*, vol. 252, pp. 16–22, 10 2013.

[38] M. Bertolotti, C. Sibilia, and A. M. Guzman, *Evanescent Waves in Optics*, vol. 206 of *Springer Series in Optical Sciences*. Cham: Springer International Publishing, 2017.

[39] D. Axelrod, "Cell-substrate contacts illuminated by total internal reflection fluorescence," *The Journal of Cell Biology*, vol. 89, pp. 141–145, 4 1981.

[40] M. Cardoso Dos Santos, C. Vézy, and R. Jaffiol, "Nanoscale characterization of vesicle adhesion by normalized total internal reflection fluorescence microscopy," *Biochimica et Biophysica Acta (BBA) - Biomembranes*, vol. 1858, pp. 1244–1253, 6 2016.

[41] J. Oreopoulos and C. M. Yip, "Probing Membrane Order and Topography in Supported Lipid Bilayers by Combined Polarized Total Internal Reflection

Fluorescence-Atomic Force Microscopy," *Biophysical Journal*, vol. 96, pp. 1970–1984, 3 2009.

[42] A. E. Ward, V. Kiessling, O. Pornillos, J. M. White, B. K. Ganser-Pornillos, and L. K. Tamm, "HIV-cell membrane fusion intermediates are restricted by Serincs as revealed by cryo-electron and TIRF microscopy," *Journal of Biological Chemistry*, vol. 295, pp. 15183–15195, 11 2020.

[43] R. M. Luik, M. M. Wu, J. Buchanan, and R. S. Lewis, "The elementary unit of store-operated Ca2+ entry: local activation of CRAC channels by STIM1 at ER-plasma membrane junctions.," *The Journal of cell biology*, vol. 174, pp. 815–25, 9 2006.

[44] M. J. Taylor, D. Perrais, and C. J. Merrifield, "A High Precision Survey of the Molecular Dynamics of Mammalian Clathrin-Mediated Endocytosis," *PLOS Biology*, vol. 9, no. 3, p. e1000604, 2011.

[45] A. Bella, M. Shaw, S. Ray, and M. G. Ryadnov, "Filming protein fibrillogenesis in real time," *Scientific Reports*, vol. 4, pp. 1–6, 12 2014.

[46] A. L. Mattheyses and D. Axelrod, "Direct measurement of the evanescent field profile produced by objective-based total internal reflection fluorescence," *Journal of Biomedical Optics*, vol. 11, no. 1, p. 014006, 2006.

[47] D. Axelrod, "Total internal reflection fluorescence microscopy in cell biology," *Traffic (Copenhagen, Denmark)*, vol. 2, pp. 764–774, 11 2001.

[48] H. M. Grandin, B. Städler, M. Textor, and J. Vörös, "Waveguide excitation fluorescence microscopy: A new tool for sensing and imaging the biointerface," *Biosensors and Bioelectronics*, vol. 21, pp. 1476–1482, 2 2006.

[49] R. Diekmann, I. Helle, C. I. Øie, P. McCourt, T. R. Huser, M. Schüttpelz, and B. S. Ahluwalia, "Chip-based wide field-of-view nanoscopy," *Nature Photonics 2017 11:5*, vol. 11, pp. 322–328, 4 2017.

[50] D. A. Coucheron, I. Helle, C. I. Øie, J. C. Tinguely, and B. S. Ahluwalia, "High-Throughput Total Internal Reflection Fluorescence and Direct Stochastic Optical Reconstruction Microscopy Using a Photonic Chip," *JoVE (Journal of Visualized Experiments)*, vol. 2019, p. e60378, 11 2019.

[51] L. E. Villegas-Hernández, V. Dubey, M. Nystad, J. C. Tinguely, D. A. Coucheron, F. T. Dullo, A. Priyadarshi, S. Acuña, A. Ahmad, J. M. Mateos, G. Barmettler, U. Ziegler, B. Birgisdottir, A. M. K. Hovd, K. A. Fenton, G. Acharya, K. Agarwal, and B. S. Ahluwalia, "Chip-based multimodal super-resolution microscopy for histological investigations of cryopreserved tissue sections," *Light: Science and Applications*, vol. 11, 12 2022.

[52] M. Tokunaga, N. Imamoto, and K. Sakata-Sogawa, "Highly inclined thin illumination enables clear single-molecule imaging in cells," *Nature Methods*, vol. 5, pp. 159–, 2 2008.

[53] J. Boulanger, C. Gueudry, D. Münch, B. Cinquin, P. Paul-Gilloteaux, S. Bardin, C. Guérin, F. Senger, L. Blanchoin, and J. Salamero, "Fast high-resolution 3D total internal reflection fluorescence microscopy by incidence angle scanning and azimuthal averaging," *Proceedings of the National Academy of Sciences*, 11 2014.

[54] A. Archetti, E. Glushkov, C. Sieben, A. Stroganov, A. Radenovic, and S. Manley, "Waveguide-PAINT offers an open platform for large field-of-view super-resolution imaging," *Nature Communications*, vol. 10, p. 1267, 12 2019.

[55] I. Jayasinghe, A. H. Clowsley, R. Lin, T. Lutz, C. Harrison, E. Green, D. Baddeley, L. Di Michele, and C. Soeller, "True Molecular Scale Visualization of Variable Clustering Properties of Ryanodine Receptors," *Cell Reports*, vol. 22, pp. 557–567, 1 2018.

[56] H. E. Ives and T. C. Fry, "Standing Light Waves; Repetition of an Experiment by Wiener, Using a Photoelectric Probe Surface," *JOSA, Vol. 23, Issue 3, pp. 73-83*, vol. 23, pp. 73–83, 3 1933.

[57] F. Lanni, "Standing wave fluorescence microscopy," in *Applications of Fluorescence in the Biomedical Sciences* (D. Taylor, A. Waggoner, R. Murphy, F. Lanni, and R. Birge, eds.), pp. 505–21, 1986.

[58] R. Amor, S. Mahajan, W. B. Amos, and G. McConnell, "Standing-wave-excited multiplanar fluorescence in a laser scanning microscope reveals 3D information on red blood cells," *Scientific Reports*, vol. 4, 5 2015.

[59] K. Elsayad, A. Urich, P. S. Tan, M. Nemethova, J. V. Small, K. Unterrainer, and K. G. Heinze, "Spectrally coded optical nanosectioning (SpecON) with biocompatible metal-dielectric-coated substrates," *Proceedings of the National Academy of Sciences of the United States of America*, vol. 110, pp. 20069–20074, 12 2013.

[60] P. W. Tinning, R. Scrimgeour, and G. McConnell, "Widefield standing wave microscopy of red blood cell membrane morphology with high temporal resolution," *Biomedical Optics Express*, vol. 9, p. 1745, 4 2018.

[61] J. K. Schniete, P. W. Tinning, R. C. Scrimgeour, G. Robb, L. S. Kölln, K. Wesencraft, N. R. Paul, T. J. Bushell, and G. McConnell, "An evaluation of multi-excitation-wavelength standing-wave fluorescence microscopy (TartanSW) to improve sampling density in studies of the cell membrane and cytoskeleton," *Scientific Reports*, vol. 11, p. 2903, 2 2021.

[62] X. Li, Y. Wu, Y. Su, I. Rey-Suarez, C. Matthaeus, T. B. Updegrove, Z. Wei, L. Zhang, H. Sasaki, Y. Li, M. Guo, J. P. Giannini, H. D. Vishwasrao, J. Chen, S. J. J. Lee, L. Shao, H. Liu, K. S. Ramamurthi, J. W. Taraska, A. Upadhyaya, P. La Riviere, and H. Shroff, "Three-dimensional structured illumination microscopy with enhanced axial resolution," *Nature Biotechnology 2023*, pp. 1–13, 1 2023.

[63] "Meso- definition and meaning — Collins English Dictionary."

[64] N. J. Sofroniew, D. Flickinger, J. King, and K. Svoboda, "A large field of view two-photon mesoscope with subcellular resolution for in vivo imaging," *eLife*, vol. 5, p. e14472, 6 2016.

[65] J. N. Stirman, I. T. Smith, M. W. Kudenov, and S. L. Smith, "Wide field-of-view, multi-region, two-photon imaging of neuronal activity in the mammalian brain," *Nature Biotechnology*, vol. 34, p. 857, 6 2016.

[66] "Movable Aperture Lensless Transmission Microscopy: A Novel Phase Retrieval Algorithm,"

[67] G. Zheng, R. Horstmeyer, and C. Yang, "Wide-field, high-resolution Fourier ptychographic microscopy," *Nature Photonics*, vol. 7, pp. 739–745, 9 2013.

[68] J. Huisken, J. Swoger, F. D. Bene, J. Wittbrodt, and E. H. K. Stelzer, "Optical Sectioning Deep Inside Live Embryos by Selective Plane Illumination Microscopy," *Science*, vol. 305, pp. 1007–1009, 8 2004.

[69] M. Weber and J. Huisken, "Light sheet microscopy for real-time developmental biology," *Current Opinion in Genetics & Development*, vol. 21, pp. 566–572, 10 2011.

[70] F. F. Voigt, D. Kirschenbaum, E. Platonova, S. Pagès, R. A. Campbell, R. Kastli, M. Schaettin, L. Egolf, A. van der Bourg, P. Bethge, K. Haenraets, N. Frézel, T. Topilko, P. Perin, D. Hillier, S. Hildebrand, A. Schueth, A. Roebroeck, B. Roska, E. T. Stoeckli, R. Pizzala, N. Renier, H. U. Zeilhofer, T. Karayannis, U. Ziegler, L. Batti, A. Holtmaat, C. Lüscher, A. Aguzzi, and F. Helmchen, "The mesoSPIM initiative: open-source light-sheet microscopes for imaging cleared tissue," *Nature Methods 2019 16:11*, vol. 16, pp. 1105–1108, 9 2019.

[71] G. McConnell, J. Trägårdh, R. Amor, J. Dempster, E. Reid, and W. B. Amos, "A novel optical microscope for imaging large embryos and tissue volumes with sub-cellular resolution throughout," *eLife*, vol. 5, p. e18659, 9 2016.

[72] G. Mcconnell and W. B. Amos, "Application of the Mesolens for subcellular resolution imaging of intact larval and whole adult Drosophila," *Journal of microscopy*, vol. 270, pp. 252–258, 5 2018.

[73] J. Schniete, A. Franssen, J. Dempster, T. J. Bushell, W. B. Amos, and G. McConnell, "Fast Optical Sectioning for Widefield Fluorescence Mesoscopy with the Mesolens based on HiLo Microscopy," *Scientific Reports*, vol. 8, 12 2018.

[74] E. Battistella, J. Schniete, K. Wesencraft, J. F. Quintana, and G. McConnell, "Light-sheet mesoscopy with the Mesolens provides fast sub-cellular resolution imaging throughout large tissue volumes," *iScience*, vol. 25, p. 104797, 9 2022.

[75] E. Battistella, J. F. Quintana, and G. McConnell, "Application of Light-Sheet Mesoscopy to Image Host-Pathogen Interactions in Intact Organs," *Frontiers in Cellular and Infection Microbiology*, vol. 12, p. 771, 6 2022.

[76] J. Fan, J. Suo, J. Wu, H. Xie, Y. Shen, F. Chen, G. Wang, L. Cao, G. Jin, Q. He, T. Li, G. Luan, L. Kong, Z. Zheng, and Q. Dai, "Video-rate imaging of biological dynamics at centimetre scale and micrometre resolution," *Nature Photonics*, vol. 13, pp. 809–816, 11 2019.

[77] L. Huang, X. Zhang, Y. Feng, F. Liang, and W. Wang, "High content drug screening of primary cardiomyocytes based on microfluidics and real-time ultra-large-scale high-resolution imaging," *Lab on a Chip*, vol. 22, pp. 1206–1213, 3 2022.

[78] L. Schermelleh, A. Ferrand, T. Huser, C. Eggeling, M. Sauer, O. Biehlmaier, and G. P. C. Drummen, "Super-resolution microscopy demystified," *Nature Cell Biology*, vol. 21, p. 72, 1 2019.

[79] E. Betzig, G. H. Patterson, R. Sougrat, O. W. Lindwasser, S. Olenych, J. S. Bonifacino, M. W. Davidson, J. Lippincott-Schwartz, and H. F. Hess, "Imaging intracellular fluorescent proteins at nanometer resolution," *Science*, vol. 313, pp. 1642–1645, 9 2006.

[80] M. J. Rust, M. Bates, and X. Zhuang, "Sub-diffraction-limit imaging by stochastic optical reconstruction microscopy (STORM)," *Nature Methods 2006 3:10*, vol. 3, pp. 793–796, 8 2006.

[81] R. Henriques, C. Griffiths, E. Hesper Rego, and M. M. Mhlanga, "PALM and STORM: Unlocking live-cell super-resolution," *Biopolymers*, vol. 95, pp. 322–331, 5 2011.

[82] L. Schermelleh, P. M. Carlton, S. Haase, L. Shao, L. Winoto, P. Kner, B. Burke, M. C. Cardoso, D. A. Agard, M. G. Gustafsson, H. Leonhardt, and J. W. Sedat, "Subdiffraction multicolor imaging of the nuclear periphery with 3D structured illumination microscopy," *Science (New York, N.Y.)*, vol. 320, pp. 1332–1336, 6 2008.

[83] K. I. Willig, B. Harke, R. Medda, and S. W. Hell, "STED microscopy with continuous wave beams," *Nature Methods 2007 4:11*, vol. 4, pp. 915–918, 10 2007.

[84] A. T. Wassie, Y. Zhao, and E. S. Boyden, "Expansion microscopy: principles and uses in biological research," *Nature Methods 2018 16:1*, vol. 16, pp. 33–41, 12 2018.

[85] M. D. Wang and D. Axelrod, "Time-lapse total internal reflection fluorescence video of acetylcholine receptor cluster formation on myotubes," *Developmental Dynamics*, vol. 201, pp. 29–40, 9 1994.

[86] P. Toglia, G. Ullah, and J. E. Pearson, "Analyzing optical imaging of Ca 2+ signals via TIRF microscopy: The limits on resolution due to chemical rates and depth of the channels," *Cell Calcium*, vol. 67, pp. 65–73, 11 2017.

[87] J. Schnitzbauer, M. T. Strauss, T. Schlichthaerle, F. Schueder, and R. Jungmann, "Super-resolution microscopy with DNA-PAINT," *Nature Protocols 2017 12:6*, vol. 12, pp. 1198–1228, 5 2017.

[88] J. Dempster, D. L. Wokosin, K. D. McCloskey, J. M. Girkin, and A. M. Gurney, "WinFluor: an integrated system for the simultaneous recording of cell fluorescence images and electrophysiological signals on a single computer system," *British Journal of Pharmacology*, vol. 137, no. 146, 2002.

[89] C. T. Rueden, J. Schindelin, M. C. Hiner, B. E. DeZonia, A. E. Walter, E. T. Arena, and K. W. Eliceiri, "ImageJ2: ImageJ for the next generation of scientific image data," *BMC Bioinformatics*, vol. 18, p. 529, 11 2017.

[90] P. Virtanen, R. Gommers, T. E. Oliphant, M. Haberland, T. Reddy, D. Cournapeau, E. Burovski, P. Peterson, W. Weckesser, J. Bright, S. J. van der Walt, M. Brett, J. Wilson, K. J. Millman, N. Mayorov, A. R. Nelson, E. Jones, R. Kern, E. Larson, C. J. Carey, Polat, Y. Feng, E. W. Moore, J. VanderPlas, D. Laxalde, J. Perktold, R. Cimrman, I. Henriksen, E. A. Quintero, C. R. Harris, A. M. Archibald, A. H. Ribeiro, F. Pedregosa, P. van Mulbregt, A. Vijaykumar, A. P. Bardelli, A. Rothberg, A. Hilboll, A. Kloeckner, A. Scopatz, A. Lee, A. Rokem, C. N. Woods, C. Fulton, C. Masson, C. Häggström, C. Fitzgerald, D. A. Nicholson, D. R. Hagen, D. V. Pasechnik, E. Olivetti, E. Martin, E. Wieser, F. Silva, F. Lenders, F. Wilhelm, G. Young, G. A. Price, G. L. Ingold, G. E. Allen, G. R. Lee, H. Audren, I. Probst, J. P. Dietrich, J. Silterra, J. T. Webber, J. Slavič, J. Nothman, J. Buchner, J. Kulick, J. L. Schönberger, J. V. de Miranda Cardoso, J. Reimer, J. Harrington, J. L. C. Rodríguez, J. Nunez-Iglesias, J. Kuczynski, K. Tritz, M. Thoma, M. Newville, M. Kümmerer, M. Bolingbroke, M. Tartre, M. Pak, N. J. Smith, N. Nowaczyk, N. Shebanov, O. Pavlyk, P. A. Brodtkorb, P. Lee, R. T. McGibbon, R. Feldbauer, S. Lewis, S. Tygier, S. Sievert, S. Vigna, S. Peterson, S. More, T. Pudlik, T. Oshima, T. J. Pingel, T. P. Robitaille, T. Spura, T. R. Jones, T. Cera, T. Leslie, T. Zito, T. Krauss, U. Upadhyay, Y. O. Halchenko, and Y. Vázquez-Baeza, "SciPy 1.0: fundamental algorithms for scientific computing in Python," *Nature Methods*, vol. 17, pp. 261–272, 3 2020.

[91] D. Sage, L. Donati, F. Soulez, D. Fortun, G. Schmit, A. Seitz, R. Guiet, C. Vonesch, and M. Unser, "DeconvolutionLab2: An open-source software for deconvolution microscopy," *Methods*, vol. 115, pp. 28–41, 2 2017.

[92] A. Sarkar, R. B. Robertson, and J. M. Fernandez, "Simultaneous atomic force microscope and fluorescence measurements of protein unfolding using a calibrated

evanescent wave," *Proceedings of the National Academy of Sciences of the United States of America*, vol. 101, pp. 12882–12886, 8 2004.

[93] I. Arganda-Carreras, V. Kaynig, C. Rueden, K. W. Eliceiri, J. Schindelin, A. Cardona, and H. S. Seung, "Trainable Weka Segmentation: a machine learning tool for microscopy pixel classification," *Bioinformatics*, vol. 33, pp. 2424–2426, 8 2017.

[94] M. Webster, K. L. Witkin, and O. Cohen-Fix, "Sizing up the nucleus: nuclear shape, size and nuclear-envelope assembly," *Journal of Cell Science*, vol. 122, pp. 1477–1486, 5 2009.

[95] C. E. Turner, J. R. Glenney, and K. Burridge, "Paxillin: a new vinculin-binding protein present in focal adhesions.," *Journal of Cell Biology*, vol. 111, pp. 1059–1068, 9 1990.

[96] A. Möhl, S. Wickenhagen, and U. Fuchs, "Gauss to top-hat beam shaping with aspheres," *High-Power Laser Materials Processing: Lasers, Beam Delivery, Diagnostics, and Applications V*, vol. 9741, p. 974102, 3 2016.

[97] M. A. Model and J. K. Burkhardt, "A Standard for Calibration and Shading Correction of a Fluorescence Microscope," 2001.

[98] D. Pinkel, J. Gray, R. Segraves, F. Waldman, B. Trask, L. C. Yu, D. Eastmond, and P. Dean, "Fluorescent Nucleic Acid Hybridization Methods.," p. 123, 6 1989.

[99] M. Shaw, R. Claveau, P. Manescu, M. Elmi, B. J. Brown, R. Scrimgeour, L. S. Kölln, G. McConnell, and D. Fernandez-Reyes, "Optical mesoscopy, machine learning, and computational microscopy enable high information content diagnostic imaging of blood films," *The Journal of Pathology*, vol. 255, pp. 62–71, 9 2021.

[100] Travis J Crites and Lirong Chen and Rajat Varma, "A TIRF microscopy technique for real-time, simultaneous imaging of the TCR and its associated signaling proteins," *Journal of Visualized Experiments*, vol. 61, 3 2012.

[101] A. K. Buck, D. E. Elmore, and L. E. Darling, "Using fluorescence microscopy to shed light on the mechanisms of antimicrobial peptides," *Future Medicinal Chemistry*, vol. 11, pp. 2447–2460, 9 2019.

[102] S. Sen-Britain, D. M. Britain, W. L. Hicks, and J. A. Gardella, "ToF-SIMS and TIRF microscopy investigation on the effects of HEMA copolymer surface chemistry on spatial localization, surface intensity, and release of fluorescently labeled keratinocyte growth factor," *Biointerphases*, vol. 14, p. 051003, 9 2019.

[103] P. Kner, B. B. Chhun, E. R. Griffis, L. Winoto, and M. G. L. Gustafsson, "Super-resolution video microscopy of live cells by structured illumination," *Nature Methods*, vol. 6, pp. 339–342, 5 2009.

[104] J. Roth, J. Mehl, and A. Rohrbach, "Fast TIRF-SIM imaging of dynamic, low-fluorescent biological samples," *Biomedical Optics Express*, vol. 11, p. 4008, 7 2020.

[105] A. Jost, A. Sentenac, E. Mudry, H. Giovannini, J. Girard, K. Belkebir, K. Wicker, N. Sandeau, R. Ayuk, R. Heintzmann, and T. Mangeat, "Structured illumination fluorescence microscopy with distorted excitations using a filtered blind-SIM }algorithm," *Optics Letters, Vol. 38, Issue 22, pp. 4723-4726*, vol. 38, pp. 4723–4726, 11 2013.

[106] G. McConnell and W. B. Amos, "Application of the Mesolens for subcellular resolution imaging of intact larval and whole adult Drosophila," *Journal of Microscopy*, vol. 270, no. 2, pp. 252–258, 2018.

[107] F. Voigt, C. J. Engelbrecht, and F. Helmchen, "Miniaturized selective plane illumination microscopy for high-contrast in vivo fluorescence imaging," *Optics Letters, Vol. 35, Issue 9, pp. 1413-1415*, vol. 35, pp. 1413–1415, 5 2010.

[108] J. Mertz and J. Kim, "Scanning light-sheet microscopy in the whole mouse brain with HiLo background rejection," *Journal of Biomedical Optics*, vol. 15, p. 016027, 1 2010.

[109] K. Zebisch, V. Voigt, M. Wabitsch, and M. Brandsch, "Protocol for effective differentiation of 3T3-L1 cells to adipocytes," *Analytical Biochemistry*, vol. 425, pp. 88–90, 6 2012.

[110] A. Klip, T. E. McGraw, and D. E. James, "Thirty sweet years of GLUT4," *The Journal of Biological Chemistry*, vol. 294, pp. 11369–11381, 7 2019.

[111] A. M. Koester, A. Geiser, K. M. Laidlaw, S. Morris, M. F. Cutiongco, L. Stirrat, N. Gadegaard, E. Boles, H. L. Black, N. J. Bryant, and G. W. Gould, "EFR3 and phosphatidylinositol 4-kinase IIIα regulate insulin-stimulated glucose transport and GLUT4 dispersal in 3T3-L1 adipocytes," *Bioscience Reports*, vol. 42, 7 2022.

[112] R. T. Kendall and C. A. Feghali-Bostwick, "Fibroblasts in fibrosis: Novel roles and mediators," *Frontiers in Pharmacology*, vol. 5 MAY, p. 123, 5 2014.

[113] A. J. Richard, U. White, C. M. Elks, and J. M. Stephens, "Adipose Tissue: Physiology to Metabolic Dysfunction," *Endotext*, 4 2020.

[114] S. Morris, N. D. Geoghegan, J. B. Sadler, A. M. Koester, H. L. Black, M. Laub, L. Miller, L. Heffernan, J. C. Simpson, C. C. Mastick, J. Cooper, N. Gadegaard, N. J. Bryant, and G. W. Gould, "Characterisation of GLUT4 trafficking in HeLa cells: comparable kinetics and orthologous trafficking mechanisms to 3T3-L1 adipocytes," *PeerJ*, vol. 8, no. 3, 2020.

[115] L. Dean, "Blood and the cells it contains," in *Cover of Blood Groups and Red Cell Antigens Blood Groups and Red Cell Antigens*, National Center for Biotechnology Information (US), 2005.

[116] M. Diez-Silva, M. Dao, J. Han, C. T. Lim, and S. Suresh, "Shape and biomechanics characteristics of human red blood cells in health and disease," *MRS Bulletin*, vol. 35, pp. 382–388, 1 2010.

[117] K. Zuiderveld, "Contrast Limited Adaptive Histogram Equalization," *Graphics Gems*, pp. 474–485, 1 1994.

[118] R. C. Scrimgeour, *Development of computational methods for standing wave microscopy.* PhD thesis, University of Strathclyde, Glasgow, 2019.

[119] David Fischer, "radialavg.zip (https://www.mathworks.com/matlabcentral/fileexchange/46468-radialavg-zip)," 2020.

[120] P. Virtanen, R. Gommers, T. E. Oliphant, M. Haberland, T. Reddy, D. Cournapeau, E. Burovski, P. Peterson, W. Weckesser, J. Bright, S. J. van der Walt, M. Brett, J. Wilson, K. J. Millman, N. Mayorov, A. R. J. Nelson, E. Jones, R. Kern, E. Larson, C. J. Carey, Polat, Y. Feng, E. W. Moore, J. VanderPlas, D. Laxalde, J. Perktold, R. Cimrman, I. Henriksen, E. A. Quintero, C. R. Harris, A. M. Archibald, A. H. Ribeiro, F. Pedregosa, P. van Mulbregt, A. Vijaykumar, A. P. Bardelli, A. Rothberg, A. Hilboll, A. Kloeckner, A. Scopatz, A. Lee, A. Rokem, C. N. Woods, C. Fulton, C. Masson, C. Häggström, C. Fitzgerald, D. A. Nicholson, D. R. Hagen, D. V. Pasechnik, E. Olivetti, E. Martin, E. Wieser, F. Silva, F. Lenders, F. Wilhelm, G. Young, G. A. Price, G.-L. Ingold, G. E. Allen, G. R. Lee, H. Audren, I. Probst, J. P. Dietrich, J. Silterra, J. T. Webber, J. Slavič, J. Nothman, J. Buchner, J. Kulick, J. L. Schönberger, J. V. de Miranda Cardoso, J. Reimer, J. Harrington, J. L. C. Rodríguez, J. Nunez-Iglesias, J. Kuczynski, K. Tritz, M. Thoma, M. Newville, M. Kümmerer, M. Bolingbroke, M. Tartre, M. Pak, N. J. Smith, N. Nowaczyk, N. Shebanov, O. Pavlyk, P. A. Brodtkorb, P. Lee, R. T. McGibbon, R. Feldbauer, S. Lewis, S. Tygier, S. Sievert, S. Vigna, S. Peterson, S. More, T. Pudlik, T. Oshima, T. J. Pingel, T. P. Robitaille, T. Spura, T. R. Jones, T. Cera, T. Leslie, T. Zito, T. Krauss, U. Upadhyay, Y. O. Halchenko, and Y. Vázquez-Baeza, "SciPy 1.0: fundamental algorithms for scientific computing in Python," *Nature Methods*, vol. 17, pp. 261–272, 3 2020.

[121] K. Kitagawa, "Fast Surface Profiling by Multi-Wavelength Single-Shot Interferometry," *http://dx.doi.org/10.1080/15599612.2010.484522*, vol. 4, pp. 136–156, 4 2010.

[122] D. Cohoe, I. Hanczarek, J. K. Wallace, and J. Nadeau, "Multiwavelength Digital Holographic Imaging and Phase Unwrapping of Protozoa Using Custom Fiji Plug-

ins," *Frontiers in Physics*, vol. 7, 7 2019.

[123] K. H. Vining and D. J. Mooney, "Mechanical forces direct stem cell behaviour in development and regeneration," *Nature Reviews Molecular Cell Biology 2017 18:12*, vol. 18, pp. 728–742, 11 2017.

[124] J. Christopher, P. Tinning, D. Uttamchandani, R. L. Bauer Jay Christopher, P. W. Tinning, and R. Bauer, "3D printing optical components for microscopy using a desktop 3D printer," *https://doi.org/10.1117/12.2608614*, vol. 12013, pp. 136–142, 3 2022.

[125] S. Culley, K. L. Tosheva, P. Matos Pereira, and R. Henriques, "SRRF: Universal live-cell super-resolution microscopy," *The International Journal of Biochemistry & Cell Biology*, vol. 101, p. 74, 8 2018.